

Turbulence modeling for large eddy simulation of incompressible flows using high-order discontinuous Galerkin methods

Bachelorarbeit

Autor:
Tim Dockhorn

Matrikelnummer:
03660025

Betreuer:
Niklas Fehn, M.Sc.

1. Dezember 2017

Selbstständigkeitserklärung

Ich erkläre hiermit, dass ich die vorliegende Arbeit selbstständig angefertigt habe, alle Zitate als solche kenntlich gemacht sowie alle benutzten Quellen und Hilfsmittel angegeben habe.

Garching b. München, 1. Dezember 2017

Abstract

This thesis deals with turbulence modeling for under-resolved incompressible flows using high-order discontinuous Galerkin methods. The incompressible Navier–Stokes equations are implicitly filtered according to a large eddy simulation approach. The concept of numerical dissipation and its ability to serve as an appropriate turbulence model is briefly described. In this work, turbulence models based on the eddy viscosity assumption are investigated. We further analyze four state of the art local eddy viscosity models. The drawback of identifying an appropriate model constant when using local eddy viscosity models is addressed. We investigate if an eddy viscosity model is capable of stabilizing an eventually unstable numerical scheme, and thus if it has the ability to improve or even replace the use of numerical dissipation. Numerical results of two turbulent test cases, for different combinations of numerical dissipation with eddy viscosity models, are presented.

Zusammenfassung

Diese Arbeit beschäftigt sich mit der Turbulenzmodellierung für schwach aufgelöste Strömungen mit diskontinuierlichen Galerkin-Methoden hoher Ordnung. Die inkompressiblen Navier-Stokes-Gleichungen werden impliziert gefiltert nach dem Grobstruktursimulationsansatz. Das Konzept der numerischen Dissipation und deren Eignung als Turbulenzmodell zu dienen wird knapp beschrieben. In dieser Arbeit werden Turbulenzmodelle nach dem Wirbelviskositätsansatzes untersucht. Wir analysieren vier lokale Wirbelviskositätsmodelle nach akutellem Stand der Technik. Die Schwierigkeit der Bestimmung einer geeigneten Modellkonstanten bei der Benutzung eines lokalen Wirbelviskositätsmodells wird angesprochen. Wir untersuchen ob ein Wirbelviskositätsmodell in der Lage ist ein eventuell instabiles numerisches Verfahren zu stabilisieren, beziehungsweise ob es in der Lage ist die Benutzung von numerischer Dissipation zu verbessern oder gar zu ersetzen. Numerische Ergebnisse für zwei turbulente Testfälle mit verschiedenen Kombinationen von numerischer Dissipation und Wirbelviskositätsmodell werden gezeigt.

Contents

1	Introduction	2
1.1	Motivation	2
1.2	Outline	4
2	Physics of turbulence	6
2.1	Incompressible Navier–Stokes equations	6
2.2	The theory of turbulence	8
2.2.1	The energy cascade	8
2.2.2	The Kolmogorov hypotheses	9
3	Large eddy simulation	12
3.1	The filtered Navier–Stokes equations	12
3.2	Eddy viscosity models	14
3.2.1	The Smagorinsky model	16
3.2.2	The Vreman model	18
3.2.3	The WALE Model	19
3.2.4	The σ -model	20
3.2.5	Model constants and summary of the local eddy viscosity models .	21
3.2.6	A dynamic eddy viscosity model	21
4	Numerical discretization	24
4.1	Temporal discretization	24
4.1.1	High-order dual splitting scheme	24
4.2	Spatial discretization	26
4.2.1	Convective step	27
4.2.2	Pressure and projection step	29
4.2.3	Viscous step	29
4.3	Instabilities and the implicit large eddy simulation	30
4.4	Element shape and basis functions	31
4.5	The characteristic filter width	32
4.6	Implementation and computation of integrals	33

5 Numerical results	36
5.1 Turbulent channel flow	36
5.1.1 Computational domain	37
5.1.2 Boundary and initial conditions	37
5.1.3 Time advancement and post-processing	38
5.1.4 Evaluation	39
5.1.5 Discussion of results	45
5.2 Backward facing step	46
5.2.1 Computational domain	46
5.2.2 Boundary and initial conditions	46
5.2.3 Time advancement and post-processing	49
5.2.4 Evaluation and the importance of turbulent inflow data	51
5.3 Backward facing step with precursor simulation	53
5.3.1 Computational domain	53
5.3.2 Boundary and initial conditions	54
5.3.3 Time advancement and post-processing	54
5.3.4 Evaluation	55
5.3.5 Discussion of results	65
6 Conclusion and outlook	66
A Appendix	xi
A.1 Mesh for turbulent channel problem	xi
A.2 Mesh for backward facing step problem ER = 1.2	xii
A.3 Mesh for backward facing step problem ER = 1.5 with precursor	xiii

List of Figures

2.1	The energy cascade [46]	10
2.2	The energy spectrum [46]	11
4.1	Comparison of smooth function ψ to piecewise smooth function ψ_h [8]	27
4.2	Curve fitting of normalized Gaussian-like filter width data [41]	33
5.1	Computational domain of the turbulent channel	37
5.2	Turbulent channel flow $Re_\tau = 180$ without numerical dissipation and spatial discretization (3, 3)	40
5.3	Turbulent channel flow $Re_\tau = 180$ with numerical dissipation and spatial discretization (3, 3)	41
5.4	Turbulent channel flow $Re_\tau = 180$ with decreased eddy viscosity constant $C_m^{\text{new}} = C_m/\sqrt{2}$ and spatial discretization (3, 3)	42
5.5	Turbulent channel flow $Re_\tau = 395$ with decreased eddy viscosity constant $C_m^{\text{new}} = C_m/\sqrt{2}$ and spatial discretization (3, 3)	43
5.6	Turbulent channel flow $Re_\tau = 395$ with decreased eddy viscosity constant $C_m^{\text{new}} = C_m/\sqrt{2}$ and spatial discretization (3, 6)	43
5.7	Turbulent channel flow $Re_\tau = 590$ with decreased eddy viscosity constant $C_m^{\text{new}} = C_m/\sqrt{2}$ and spatial discretization (3, 6)	44
5.8	Turbulent channel flow $Re_\tau = 590$ for several σ -models and spatial discretization (3, 6)	45
5.9	Computational domain of the backward facing step $ER = 1.2$	47
5.10	Different layers for near-wall flow [46]	48
5.11	Numerical results for large eddy simulations (implicit and σ -model) of a backward facing step ($ER = 1.2$) compared with DNS [31] and LES [29] solutions	50
5.12	Sketch of backward facing step ($ER = 1.5$) geometry with turbulent channel as a precursor simulation	54
5.13	Plot of the mean velocity for the pure ILES approach	56
5.14	Plot of the RMS values for the pure ILES approach	57
5.15	Plot of the Reynolds stress for the pure ILES approach	58
5.16	Plot of the mean velocity for combination of eddy viscosity model with numerical dissipation and spatial discretization (3, 2)	59

5.17	Plot of the RMS values for combination of eddy viscosity model with numerical dissipation and spatial discretization (3, 2)	60
5.18	Plot of the Reynolds stress for combination of eddy viscosity model with numerical dissipation and spatial discretization (3, 2)	61
5.19	Plot of the skin friction for combination of eddy viscosity model with numerical dissipation and spatial discretization (3, 2)	61
5.20	Plot of the mean velocity for combination of eddy viscosity model with numerical dissipation and spatial discretization (2, 5)	62
5.21	Plot of the RMS values for combination of eddy viscosity model with numerical dissipation and spatial discretization (2, 5)	63
5.22	Plot of the Reynolds stress for combination of eddy viscosity model with numerical dissipation and spatial discretization (2, 5)	64
5.23	Plot of the skin friction for combination of eddy viscosity model with numerical dissipation and spatial discretization (2, 5)	64
A.1	Refine levels $l = 0, 1, 2, 3$ for turbulent channel problem	xi
A.2	Refine levels $l = 0, 1$ for backward facing step problem ER = 1.2	xii
A.3	Mesh for the uniform grid ($l = 2$) and the stretched grid ($l = 3$) of a backward facing step problem ER = 1.5	xiii

List of Tables

3.1	The most common filter functions in their real and spectral representation [46]	13
3.2	Desirable properties for the differential operator of an eddy viscosity model [43]	16
3.3	Properties of the four local eddy viscosity models [43]	22
4.1	Coefficients of time integration scheme and extrapolation scheme	25
5.1	Abbreviations for the four eddy viscosity models	36
5.2	Turbulent channel flow parameters	37
5.3	Offset for the quantities $(u'_2)^+$ and $(u'_3)^+$	39
5.4	Model constants C_σ for several σ -model	44
5.5	Backward facing step flow parameters	47
5.6	Model description for backward facing step ER = 1.2	51
5.7	Global wall time for the numerical simulations of the backward facing step ER = 1.5	65
A.1	Mesh refinement for turbulent channel problem	xii
A.2	Mesh refinement for backward facing step problem ER = 1.2	xii
A.3	Mesh refinement for backward facing step problem ER = 1.5 with precursor	xiii

Nomenclature

Physical quantities

σ	Cauchy stress tensor	[N/m ²]
τ	Viscous stress tensor	[N/m ²]
f	Body force	[N/kg]
L	Velocity gradient	[1/s]
t	Surface tension	[N/m ²]
$\mathbf{u} = (u_1, \dots, u_3)^T$	Fluid velocity	[m/s]
$\mathbf{u} \otimes \mathbf{u}$	Convective flux	[m ² /s ²]
\bar{p}	Modified pressure	[m ² /s ²]
μ	Dynamic viscosity	[kg/(ms)]
ν	Kinematic viscosity	[m ² /s]
ρ	Density	[kg/m ³]
τ_w	Wall shear stress	[N/m ²]
p_d	Dynamic pressure	[N/m ²]
p_k	Kinematic pressure	[m ² /s ²]
u_τ	Friction velocity	[m/s]

Physical constants

κ_K	Von Kármán constant
C^+	Law of the wall constant
C_k	Kolmogorov constant

Operators

\bigotimes	Direct sum
$\frac{\partial}{\partial t}$	Partial derivative (with respect to time)
$\frac{D}{Dt}$	Material derivative
$\frac{d}{dt}$	Total derivative (with respect to time)
$\{\cdot\}$	Statistical average
$[\![\cdot]\!], [\cdot]$	Jump operators
$\nabla \times$	Curl operator
∇	Divergence operator
∇^2	Laplace operator
\otimes	Dyadic product

$\{\cdot\}$	Average operator
-------------	------------------

Large eddy simulation

Ω	Rotation rate	[1/s]
τ^R	Residual stress tensor	[m ² /s ²]
τ^r	Anisotropic residual stress tensor	[m ² /s ²]
τ^d	Dynamic residual stress tensor	[m ² /s ²]
L	Velocity gradient	[1/s]
S	Rate of strain	[1/s]
Δ	Characteristic filter width	[m]
ϵ	Dissipation rate	[m ² /s ³]
η	Kolmogorov length scale	[m]
$f(x, t)$	General resolved quantity	[–]
$\hat{G}(\kappa)$	Filter function in the wavenumber space	[m]
κ_c	Cutoff wavenumber	[1/m]
ν_{SGS}	Sub-grid scale viscosity	[m ² /s]
τ_η	Kolmogorov time scale	[s]
C_m	Eddy viscosity model constant	[1]
D_m	Eddy viscosity differential operator	[1/s]
$E(\kappa)$	Energy spectrum function	[m ³ /s ²]
$f'(x, t)$	General residual quantity	[–]
$G(x)$	Filter function in the physical space	[1/m]
k_r	Residual kinetic energy	[m ² /s ²]
u_η	Kolmogorov velocity scale	[m/s]

Turbulence theory

$\mathcal{T}(l)$	Rate of transfer of energy from eddies of size larger than l to eddies smaller than l
\mathfrak{L}	Characteristic length scale
\mathfrak{U}	Characteristic velocity scale
$l < l_{DI}$	The dissipation range
$l_{EI} > l > l_{DI}$	The inertial subrange
l_{EI}	Demarcation lengthscale between the anisotropic large eddies and the isotropic small eddies

Functions

$\delta(x)$	Kronecker δ
$\mathcal{F}\{\cdot\}$	Fourier transformation
$H(x)$	Heaviside function

Numerical discretization

$(\cdot)^*$	General numerical flux
ξ_q	Quadrature point

\mathbf{F}_m	Mapping from unit cell to physical cell
\mathbf{J}	Jacobian matrix
Δt	Time step size
Γ	Boundary of a domain
Γ_D	Boundary of a domain with Dirichlet boundary condition
Γ_N	Boundary of a domain with Neumann boundary condition
\mathbb{R}^d	The set of the real numbers in d dimensions
\mathcal{T}	Triangulation
Ω	Physical domain
Ω_h	Numerical domain
Ψ_h, \mathcal{V}_h	Finite element function spaces
K	Nonoverlapping elements
L^2	Hilbert space of square-integrable functions
$l_j^k(\xi)$	Lagrange polynomial of order k
N_{qp}	Number of quadrature points
N_{el}	Number of elements
$P_k(K)$	Space of polynomials of order k on element K
V_K	Volume of element K
w_q	Quadrature weight

Abbreviations

CFD	Computational fluid dynamics
CFL	Courant–Friedrichs–Lowy
DG	Discontinuous Galerkin
DNS	Direct numerical simulation
DOF	Degrees of freedom
ER	Expansion ratio
FEM	Finite element method
FVM	Finite volume method
ILES	Implicit large eddy simulation
LES	Large eddy simulation
LGL	Legendre–Gauss–Lobatto
RANS	Reynolds-averaged Navier–Stokes
RMS	Root mean square
SIPG	Symmetric interior penalty Galerkin
WALE	Wall-adapting local eddy viscosity

Non-dimensional numbers

Re	Reynolds number
----	-----------------

Chapter 1

Introduction

1.1 Motivation

Computational fluid dynamics (CFD) is a rapidly growing field that combines disciplines of numerical analysis, fluid mechanics, and computer science. Its main purpose is to solve and analyze problems that involve fluid flows. In general, the motion of viscous fluids is described by the Navier–Stokes equations, a set of balance equations that arise from Newton’s second law of motion. Finding a smooth and bounded solution that solves the three-dimensional Navier–Stokes equations is one of the Millennium Prize problems stated by the Clay Mathematics Institute in 2000 [7], and has yet to be proven. CFD tackles the Navier–Stokes equations with a different approach: it tries to find a solution numerically by using discretization methods.

The finite volume method (FVM) and the finite element method (FEM) are two well-established discretization methods. The former is especially well-suited for convection-dominated problems but suffers from low-order accuracy [18]. Contrarily, FEM can achieve high-order accuracy; however, it eventually experiences stability problems in convection-dominated problems [18]. The desire to combine advantages of both FVM and FEM has led to the development of the discontinuous Galerkin (DG) method. The numerical solution obtained by a DG method is discontinuous between element boundaries but uses high-polynomial approximation within the element. Connectivity between neighboring elements is achieved by using the concept of numerical fluxes, which was originally developed for the FVM.

In fluid dynamics, the Reynolds number (Re) is an important quantity characterizing a fluid flow. At low Re , the fluid moves in parallel layers where no lateral mixing is apparent, characterizing it as a laminar flow. However, with increasing Re , small disturbances in the flow are no longer damped and take energy from the initial laminar state – the flow is said to become turbulent. The fluid velocity and pressure in this state varies significantly and irregularly in both space and time. Turbulence can be observed

in many situations of daily life, e.g, the flow around an airfoil, mixing of fuel and air in an engine, fluid flows in pipelines, etc. An essential aspect of turbulence is its ability to mix and transport fluids effectively; primarily due to the wide range of different length and time scales of turbulent motions [46].

In the 1970s, computers with sufficient computing power to solve the Navier–Stokes equations, resolving all scales of motions for simple problems, became available and initiated the study of direct numerical simulation (DNS). However, even though computing power has continuously increased over the last decades, the high computational costs of DNS remains a major drawback and makes its use unfeasible for complex problems in industry. In order to simplify the problem, and thus decrease computing effort, it is a common approach to apply the Reynolds decomposition [49] to the Navier–Stokes equations and solve the obtained Reynolds-averaged Navier–Stokes (RANS) equations instead. Due to the small computational costs of RANS simulation compared to DNS, the averaging method is predominantly used for CFD in industry, however, with the drawback of significantly less accuracy.

In the 1960s, a new CFD model, namely the large eddy simulation (LES), was originally proposed to simulate atmospheric flows. Using LES for turbulent flows, the larger-scale motions, which are highly affected by both the flow geometry and the boundary conditions, are computed explicitly. The influence of the smaller-scale motions can be modelled since they are to some extent universal, as stated by Kolmogorov [27]. The LES traditionally makes use of a low-pass filter so that the resulting filtered velocity and pressure field can be resolved on a coarse grid. Filtering the Navier–Stokes equations leads to a coupling of resolved and unresolved motions, which is accounted for by an additional term, namely the residual-stress tensor. Modeling this tensor has been the major challenge in LES – commonly known as the closure problem. Currently, the development and the use of LES is highly motivated by the accuracy limitations of RANS simulation and the large computational costs of DNS [46]. The reader is referred to [51] for an extensive discussion on LES.

In LES, the transfer of energy from the resolved to the unresolved scales is most often modeled with an eddy viscosity approach. According to Kolmogorov [27], the smallest-scale motions dissipate kinetic to thermal energy, but these scales are unresolved when using LES, and thus the eddy viscosity also has to mimic the correct physical dissipation. Smagorinsky was the first to propose an eddy-viscosity model [54] which is based on the filtered rate of strain and assumes that energy received by the unresolved scales is in equilibrium with the energy that is dissipated by those scales. The Smagorinksy model has the drawback that it generally produces a non-zero eddy viscosity, even though any eddy viscosity model should vanish in near-wall regions due to the no-slip condition [43]. In the following years, several attempts to improve the Smagorinsky model have been made, e.g., the use of damping functions [39], the development of a dynamic eddy viscosity model [14], etc. Moreover, new models that do not require ad hoc treatment have been proposed: Vreman derived an eddy viscosity model with low dissipation in transitional

and near-wall regions [61], and Nicoud proposed two models that have a proper near-wall behavior, namely, the wall-adapating local eddy-viscosity (WALE) model [42], and the σ -model [43]. All eddy-viscosity models share the drawback that a problem specific model constant has to be determined.

In this work, we use a high-order discontinuous Galerkin solver for under-resolved incompressible flows [8, 28]. This solver has been validated for both laminar [8, 28] and turbulent test cases [28]. Instability issues as well as their solution approaches have been discussed in [10, 28]. The coupling of velocity and pressure in combination with the incompressibility constraint leads to a complex problem that needs advanced solution techniques. For the temporal discretization, we apply the high-order dual splitting scheme [24], which leads to the decoupling of velocity and pressure, and a set of three substeps. The Lax–Friedrichs flux [18] is chosen to discretize the convective step and the symmetric interior penalty Galerkin (SIPG) method [3] is applied to the viscous step and the Poisson problem in the pressure step. Instabilities for DG discretizations of the incompressible Navier–Stokes equations in combination with the high-order dual splitting scheme have been reported in [19, 28, 56]. The scheme can be stabilized by using two penalty terms [28] which induce numerical dissipation as well as correct integration methods [10]. The idea of the implicit large eddy simulation (ILES) is that this numerical dissipation is able to mimic the correct physical dissipation of the unresolved scales and that no explicit turbulence model is needed at all. The ILES approach has been shown to yield excellent results when applied to DG discretizations of the compressible [63] and the incompressible [28] Navier–Stokes equations; however, numerical solutions of a turbulent channel flow with the DG scheme applied in this work [28] indicate that the numerical dissipation tends to be lower than the correct physical dissipation.

Marek et al. [37] successfully used a DG method with an eddy viscosity model instead of numerical dissipation to stabilize the scheme. That said, we want to investigate if an eddy viscosity model could generally improve or even replace the ILES approach used in [28]. The four mentioned eddy viscosity models are implemented within the high-order DG solver described in [28] and analyzed with respect to their accuracy. Numerical simulations for turbulent flow problems with ILES approach in combination with an additional eddy viscosity model have been carried out and are compared to DNS and ILES solutions. Based on the numerical results obtained, the different eddy viscosity models are compared.

1.2 Outline

In Chapter 2, the derivation of the incompressible Navier–Stokes equations for Newtonian fluids is summarized. Moreover, the theory of turbulence, based on the energy cascade and the Kolomogorov hypothesis, is discussed. The theory of large eddy simulation as well as its application to the incompressible Navier–Stokes equations are subject of Chap-

ter 3. Furthermore, the modeling of the residual-stress tensor with four different local eddy viscosity models is shown. Chapter 4 deals with the discretization of the incompressible Navier–Stokes equations in both space and time, and addresses the importance of numerical dissipation to stabilize the DG discretization. In Chapter 5, we present numerical results for two turbulent test cases and discuss the importance of appropriate inflow data on the simulation of turbulent flows within the LES approach. Chapter 6 summarizes the obtained results and gives an outlook on future work.

Chapter 2

Physics of turbulence

This chapter is intended to give the reader a brief summary of the physics of turbulence. First, the governing equations for incompressible fluids are reviewed, relating to the derivation given in [46]. Moreover, important concepts of turbulent flows are described.

2.1 Incompressible Navier–Stokes equations

Derivation of the governing equations The local formulation of the conservation of mass reads as

$$\frac{\partial \rho}{\partial t} + \nabla \cdot (\rho \mathbf{u}) = 0 \quad . \quad (2.1)$$

Since we want to derive the incompressible Navier–Stokes equations, we have to apply the incompressibility constraint, i.e., we set the material derivative of ρ to zero

$$\frac{D\rho}{Dt} = \frac{\partial \rho}{\partial t} + (\mathbf{u} \cdot \nabla) \rho = 0 \quad . \quad (2.2)$$

Using this constraint, equation (2.1) simplifies to

$$\nabla \cdot \mathbf{u} = 0 \quad , \quad (2.3)$$

which means that the velocity field is divergence-free. The local formulation of the momentum equation reads as

$$\frac{\partial}{\partial t}(\rho \mathbf{u}) + \nabla \cdot (\rho \mathbf{u} \otimes \mathbf{u}) = \nabla \cdot \boldsymbol{\sigma} + \rho \mathbf{f} \quad , \quad (2.4)$$

where $(a \otimes b)_{ij} = a_i b_j$ is the dyadic product. By inserting the continuity equation (2.1), the momentum equation (2.4) can be rewritten as

$$\frac{\partial}{\partial t}(\mathbf{u}) + (\mathbf{u} \cdot \nabla) \mathbf{u} = \frac{1}{\rho} \nabla \cdot \boldsymbol{\sigma} + \mathbf{f} \quad . \quad (2.5)$$

The Cauchy stress tensor can be expressed as the sum of two other stress tensors

$$\boldsymbol{\sigma} = -p_d \mathbf{I} + \boldsymbol{\tau} , \quad (2.6)$$

where \mathbf{I} is the identity tensor, and p_d and $\boldsymbol{\tau}$ denote the dynamic pressure and the viscous stress tensor, respectively. In case of Newtonian fluids, the viscous stresses are a linear function of the velocity gradient [46]. Exploiting that the velocity field is divergence-free, the viscous stress tensor can be written as

$$\boldsymbol{\tau} = \mu(\nabla \mathbf{u} + (\nabla \mathbf{u})^T) , \quad (2.7)$$

with the dynamic viscosity μ . Inserting equations (2.6) and (2.7) into the momentum equation (2.4) as well as assuming $p = \text{const.}$, the local formulation of the momentum equation can be rewritten as

$$\frac{\partial \mathbf{u}}{\partial t} + (\mathbf{u} \cdot \nabla) \mathbf{u} = -\nabla p_k + \nabla \cdot (\nu(\nabla \mathbf{u} + (\nabla \mathbf{u})^T)) + \mathbf{f} , \quad (2.8)$$

where $p_k = p_d/\rho$ and $\nu = \mu/\rho$ denote the kinematic pressure and the kinematic viscosity, respectively. The convective term can be written in an alternative form by using the incompressibility constraint

$$(\mathbf{u} \cdot \nabla) \mathbf{u} = (\mathbf{u} \cdot \nabla) \mathbf{u} + \mathbf{u}(\nabla \cdot \mathbf{u}) = \nabla \cdot (\mathbf{u} \otimes \mathbf{u}) . \quad (2.9)$$

The incompressible Navier–Stokes equation can then be written as

$$\begin{aligned} \frac{\partial \mathbf{u}}{\partial t} + \nabla \cdot (\mathbf{u} \otimes \mathbf{u}) &= -\nabla p_k + \nabla \cdot (\nu(\nabla \mathbf{u} + (\nabla \mathbf{u})^T)) + \mathbf{f} , \\ \nabla \cdot \mathbf{u} &= 0 . \end{aligned} \quad (2.10)$$

Formulation of the viscous term The correct formulation of the viscous term is crucial for this work. The kinematic viscosity ν is a fluid property and generally constant when dealing with one-phase fluid flows. Therefore the viscous term could be written in the Laplace form

$$\underbrace{\nabla \cdot (\nu(\nabla \mathbf{u} + (\nabla \mathbf{u})^T))}_{\text{divergence form}} = \nu \nabla^2 \mathbf{u} + \nu \nabla(\nabla \cdot \mathbf{u}) = \underbrace{\nu \nabla^2 \mathbf{u}}_{\text{Laplace form}} . \quad (2.11)$$

As we will see in Chapter 3, when using the linear eddy viscosity assumption to model turbulence, a spatially dependent sub-grid scale viscosity ν_{SGS} is added to the kinematic viscosity. Hence, it is appropriate to immediately treat the viscosity ν as non-constant and write the viscous term in the divergence form.

Boundary and initial conditions In order to have a unique problem, we need

to specify boundary and initial conditions. On the boundary of the physical domain $\Gamma = \partial\Omega$ either Dirichlet or Neumann boundary conditions are prescribed

$$\mathbf{u} = \mathbf{g} \text{ on } \Gamma_D , \quad (2.12)$$

$$\boldsymbol{\sigma} \cdot \mathbf{n} = \mathbf{h} \text{ on } \Gamma_N , \quad (2.13)$$

with the condition that $\Gamma = \Gamma_D \cup \Gamma_N$ and $\Gamma_D \cap \Gamma_N = \emptyset$. Attention should be paid to two important issues when using the special case of pure Dirichlet boundary conditions ($\Gamma = \Gamma_D$): the Dirichlet velocity boundary condition (2.12) must fulfill

$$\int_{\Gamma_D} \mathbf{g} \cdot \mathbf{n} d\Gamma = 0 , \quad (2.14)$$

in order to meet the incompressibility constraint. Moreover, when having pure Dirichlet boundary conditions, the pressure is just defined up to an arbitrary additive constant. This issue can be resolved by either prescribing the pressure in an arbitrary point of the domain or requiring that the mean of the pressure vanishes [59]

$$\int_{\Omega} p d\Omega = 0 . \quad (2.15)$$

The velocity field is initially defined as

$$\mathbf{u}(\mathbf{x}, t = t_0) = \mathbf{u}_0 \text{ on } \Omega , \quad (2.16)$$

where the initial condition must fulfill the incompressibility constraint as well as the boundary conditions.

2.2 The theory of turbulence

Turbulent flows have a wide spectrum of motions – ranging from the characteristic length scale of the flow geometry to significantly smaller scales, which progressively decrease as the Reynolds number increases. To understand the distribution of energy and anisotropy of the different scales two important concepts will be introduced, namely the energy cascade and the Kolmogorov hypotheses [27]. The former was proposed by Richardson in 1922 [50] and states that kinetic energy enters turbulent flow at the largest-scale motions, which are defined by the flow geometry. The energy is then transferred down the range of scales by inviscid processes, until the smallest scale (Kolmogorov scale) is reached and the energy is dissipated by viscous processes. In the following we consider a fully turbulent flow at high Reynolds number $Re = \mathfrak{U}\mathfrak{L}/\nu$ with characteristic length scale \mathfrak{L} and velocity scale \mathfrak{U} [46].

2.2.1 The energy cascade

According to Richardson's theory [50], turbulence is composed of eddies with characteristic size l , velocity $u(l)$, and time scale $\tau = l/u(l)$. An eddy is conceived to be a turbulent

motion, that is at least moderately coherent over a region of size l . The largest-scale eddies are of size $l_0 \approx \mathfrak{L}$ and velocity $u_0 = u(l_0) \approx \mathfrak{U}$. Their Reynolds number $\text{Re}_0 = u_0 l_0 / \nu$ is comparable to Re ; hence, direct effects of viscosity are negligible.

The instability of eddies is an important concept in Richardson's notion. As larger eddies break up, they transfer their energy to smaller and yet smaller eddies again. This energy cascade continues until the Reynolds number $\text{Re}(l) = u(l)l/\nu$ has become sufficiently small so that the eddy motion is stable and molecular viscosity dissipates the kinetic energy. Consequently, the rate of dissipation ϵ is determined by the transfer of energy from the largest eddies with energy of order u_0^2 . It follows that the dissipation rate scales as $\epsilon \sim u_0^2/\tau_0 = u_0^3/l_0$ [46].

2.2.2 The Kolmogorov hypotheses

Kolmogorov [27] advanced Richardson's theory in the form of three hypotheses as fundamental questions remain unanswered: What is the size l of the smallest eddies? How do the characteristic velocity $u(l)$ and time scale $\tau(l)$ behave as l approaches that size?

In general, larger eddies are anisotropic as they are significantly affected by the boundary conditions and the geometry of the flow. However, Kolmogorov argued, that the geometry of the larger eddies and also their directional bias gets lost in the scale-reduction process. Hence, the small-scale ($l \ll l_0$) turbulent motions are statistically isotropic, i.e., uniform in all directions in terms of mean values, at sufficiently high Reynolds numbers.

We introduce the length scale $l_{\text{EI}} \approx 1/6l_0$ that separates the anisotropic large eddies and the isotropic small eddies and denote the region $l < l_{\text{EI}}$ as the universal equilibrium range (see Figure 2.1). The viscous dissipation and the energy transfer are the two predominant processes in this region. A natural choice for parameters at this scale are the rate at which small scales receive energy from the larger scales (denoted as \mathcal{T}_{EI}) and the kinematic viscosity ν .

It can be shown that the rate of dissipation ϵ is highly related to \mathcal{T}_{EI} , i.e., $\epsilon \approx \mathcal{T}_{\text{EI}}$ [46]. Kolmogorov showed that the small-scale motions have a universal form that is determined by ϵ and ν ; the Kolmogorov scales for length, velocity and time are respectively defined as

$$\eta = \left(\frac{\nu^3}{\epsilon} \right)^{1/4}, \quad (2.17)$$

$$u_\eta = (\epsilon \nu)^{1/4}, \quad (2.18)$$

$$\tau_\eta = \left(\frac{\nu}{\epsilon} \right)^{1/4}. \quad (2.19)$$

The Reynolds number based on these scales is given as

$$\text{Re}_\eta = \frac{\eta u_\eta}{\nu} = \frac{\nu^{3/4} \epsilon^{1/4} \nu^{1/4}}{\nu \epsilon^{1/4}} = 1. \quad (2.20)$$

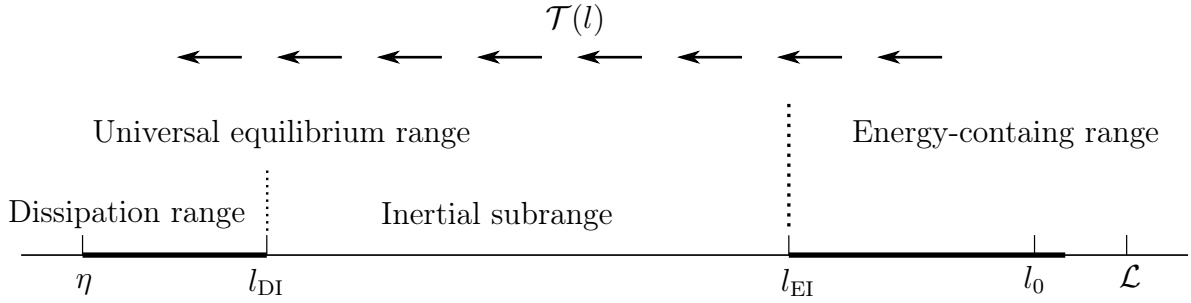


Figure 2.1: The energy cascade [46]

This is in agreement with Richardson's theory, which states that the energy cascade proceeds until the Reynolds number is small enough for dissipation to be effective. Kolmogorov found that there are two sub-regions within the universal equilibrium range, separated by the length scale $l_{DI} = 60\eta$. The motions in the inertial subrange ($l_{DI} < l < l_{EI}$) are determined by inertial effects, whereas viscous effects determine the motions in the dissipation range ($l < l_{DI}$). Using the Kolmogorov scales and the relation $\epsilon \sim u_0^3/l_0$, the ratio of the smallest to the largest scales are given as

$$\frac{\eta}{l_0} \sim Re^{-3/4} , \quad (2.21)$$

$$\frac{u_\eta}{u_0} \sim Re^{-1/4} , \quad (2.22)$$

$$\frac{\tau_\eta}{\tau_0} \sim Re^{-1/2} , \quad (2.23)$$

and thus the introductory questions have been answered – both the characteristic velocity and timescale decrease as the lengthscale approaches the Kolmogorov length scale η . It has yet to be determined how the kinetic energy is distributed over the eddies of different ranges.

We consider the case of homogenous turbulence and investigate the energy spectrum function $E(\kappa)$, where the motions of size l correspond to the wavenumber $\kappa = 2\pi/l$. The energy $K_{(\kappa_a, \kappa_b)}$ and the contribution to the dissipation rate $\epsilon_{(\kappa_a, \kappa_b)}$ contained in the wavenumber range (κ_a, κ_b) is given as [46]

$$K_{(\kappa_a, \kappa_b)} = \int_{\kappa_a}^{\kappa_b} E(\kappa) d\kappa , \quad (2.24)$$

$$\epsilon_{(\kappa_a, \kappa_b)} = \int_{\kappa_a}^{\kappa_b} 2\nu\kappa^2 E(\kappa) d\kappa . \quad (2.25)$$

Using dimensional analysis, it can be shown that [27]

$$E(\kappa) = C\epsilon^{2/3}\kappa^{-5/3} \text{ for } \frac{2\pi}{l_{EI}} < \kappa < \frac{2\pi}{l_{DI}} , \quad (2.26)$$

where C is a universal constant. A qualitative graph of the energy spectrum function for turbulent flows is illustrated in Figure 2.2. Assuming a general power law spectrum

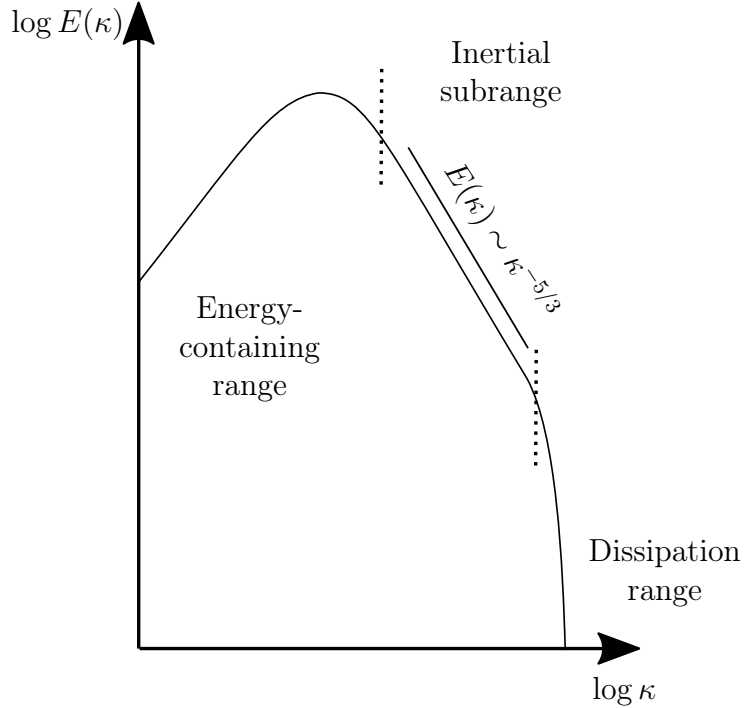


Figure 2.2: The energy spectrum [46]

$E(\kappa) = A\kappa^{-p}$, the energy contained in the range (κ, ∞) is [46]

$$K_{(\kappa, \infty)} = \int_{\kappa}^{\infty} E(\kappa') d\kappa' = \frac{A}{p-1} \kappa^{-(p-1)} \quad \text{for } p > 1 , \quad (2.27)$$

whereas the integral diverges for $p \geq 1$. The contribution of the dissipation rate for wavenumbers less than κ is [46]

$$\epsilon_{(0, \kappa)} = \int_0^{\kappa} 2\nu\kappa'^2 E(\kappa') d\kappa' = \frac{2\nu A}{3-p} \kappa^{3-p} \quad \text{for } p < 3 . \quad (2.28)$$

Choosing p according to equation (2.26), the energy decreases as $K_{(\kappa, \infty)} \sim \kappa^{-2/3}$ when approaching high wavenumbers. The dissipation rate, on the other hand, decreases as $\epsilon_{(0, \kappa)} \sim \kappa^{4/3}$ as κ approaches zero. Although the spectrum given in equation (2.26) is just applicable in the inertial subrange, the results are consistent with the observation that the majority of the kinetic energy is contained within larger-scale motions and dissipation mainly takes place within smaller-scale motions [46]. As mentioned in Chapter 3, the effect of smaller-scale motions are modeled when using LES. The observations made in this chapter indicate that accounting for the neglected dissipation is a crucial task of a turbulence model when simulating under-resolved flows.

Chapter 3

Large eddy simulation

A direct numerical simulation (DNS) solves the Navier–Stokes equations without any turbulence model, and thus must resolve every length scale. The vast computational cost of a DNS is predominantly due to the smallest scales even though the majority of the energy and anisotropy is contained in the larger scales. DNS is therefore highly impractical for the simulation of turbulent flows for industrial applications as its computational cost increases as the cube of the Reynolds number Re^3 [46].

The large eddy simulation directly represents the large unsteady turbulent motions and models the effect of smaller scale motions. The latter motions are to some extent universal whereas the former motions are effected by the flow geometry and are therefore not universal as shown in Subsection 2.2.2.

3.1 The filtered Navier–Stokes equations

According to Pope’s approach [46], there are four conceptual steps that have to be taken when using LES. First, a low-pass filtering operation is performed on the velocity field to obtain a filtered velocity field that can be adequately resolved on a coarse grid. If possible, the grid spacing should be chosen so that all the energy-containing motions are resolved. The general filtering operation was introduced by Leonard in [32] as a convolution of a unfiltered quantity $f(x, t)$ with a filter function $G(x)$

$$\bar{f}(x, t) = \int G(x - x') f(x', t) dx' , \quad (3.1)$$

where the filter function satisfies the normalization condition

$$\int G(x - x') dx' = 1 . \quad (3.2)$$

Using this filtering operation, the velocity field can be decomposed in a residual field \mathbf{u}' and a resolved field $\bar{\mathbf{u}}$ as

$$\mathbf{u}(\mathbf{x}, t) = \bar{\mathbf{u}}(\mathbf{x}, t) + \mathbf{u}'(\mathbf{x}, t) . \quad (3.3)$$

Table 3.1: The most common filter functions in their real and spectral representation [46]

Name	$G(x)$	$\hat{G}(\kappa)$
Box filter	$\frac{1}{\Delta} H\left(\frac{1}{2}\Delta - x \right)$	$\frac{2 \sin(\kappa\Delta/2)}{\kappa\Delta}$
Gaussian filter	$\left(\frac{6}{\pi\Delta^2}\right)^{1/2} \exp\left(-\frac{6x^2}{\Delta^2}\right)$	$\exp\left(-\frac{\kappa^2\Delta^2}{24}\right)$
Sharp spectral filter	$\frac{\sin(\pi x/\Delta)}{\pi x}$	$H(\kappa_c - \kappa)$

In contrast to the Reynolds decomposition, the filtered residual field is generally not zero, i.e., $\bar{\mathbf{u}}' \neq 0$ [46]. The most common filters are the box filter, the Gaussian filter, and the sharp spectral filter. Important aspects of those filters are better revealed in the wavenumber space, and thus we introduce the transfer function $\hat{G}(\kappa)$ as 2π times the Fourier transform of $G(x)$

$$\hat{G}(\kappa) = \int_x G(x) \exp(-i\kappa x) dx = 2\pi \mathcal{F}\{G(x)\} , \quad (3.4)$$

where i is the imaginary unit and κ is the wavenumber. The three mentioned one-dimensional filters are defined in Table 3.1 [46] in their real and spectral representation, where the Heaviside step function is defined as

$$H(x) = \begin{cases} 0, & x < 0 \\ 1, & x \geq 0 \end{cases} . \quad (3.5)$$

Using the box filter, the resolved velocity field $\bar{\mathbf{u}}$ is the spatial average of $\mathbf{u}(x', t)$ over the interval $x - \frac{1}{2}\Delta < x' < x + \frac{1}{2}\Delta$. Therefore, motions of every wavenumber contribute to the resolved velocity field. The sharp spectral filter, on the other hand, annihilates all motions whose absolute wavenumber is greater than the cutoff wavenumber

$$\kappa_c = \frac{\pi}{\Delta} , \quad (3.6)$$

and is, in comparison to the box filter, non-local in the physical space. The Gaussian filter is compact in both the physical and the spectral space. For further information on filter operations the reader is referred to [46]. For spatially uniform filter functions, the filtering and the differentiation operation commute [46], i.e.,

$$\overline{\nabla \cdot \mathbf{u}} = \int G(x - x') (\nabla \cdot \mathbf{u}(x', t)) dx' = \nabla \cdot \left(\int G(x - x') \mathbf{u}(x', t) dx' \right) = \nabla \cdot \bar{\mathbf{u}} . \quad (3.7)$$

By applying (3.7) to the continuity equation (2.3), it can be shown that both the filtered and the residual velocity field are divergence-free

$$\begin{aligned} \overline{\nabla \cdot \mathbf{u}} &= \nabla \cdot \bar{\mathbf{u}} = 0 , \\ \nabla \cdot \mathbf{u}' &= \nabla \cdot (\mathbf{u} - \bar{\mathbf{u}}) = 0 . \end{aligned} \quad (3.8)$$

The conservation equation governing the filtered velocity field are obtained by applying the filtering operation to the Navier–Stokes equations (2.10) assuming commutation of the filtering and differentiation operation

$$\begin{aligned} \frac{\partial \bar{\mathbf{u}}}{\partial t} + \nabla \cdot (\bar{\mathbf{u}} \otimes \bar{\mathbf{u}}) &= -\nabla \bar{p}_k + \nabla \cdot (\nu(\nabla \bar{\mathbf{u}} + (\nabla \bar{\mathbf{u}})^T)) + \bar{\mathbf{f}} , \\ \nabla \cdot \bar{\mathbf{u}} &= 0 . \end{aligned} \quad (3.9)$$

As one can easily see, an actual filter function $G(x)$ is never defined. When using LES, the computational grid is coarse (compared to DNS) and does not resolve all the turbulent motions; thus, the grid itself serves as an implicit filtering operation. For further information, the reader is referred to Section 3.2.

The set of equations (3.9) differs from the Navier–Stokes equations (2.10) as $\bar{\mathbf{u}} \otimes \bar{\mathbf{u}} \neq \bar{\mathbf{u}} \otimes \bar{\mathbf{u}}$. The difference is called the residual-stress tensor and defined as [46]

$$\boldsymbol{\tau}^R = \bar{\mathbf{u}} \otimes \bar{\mathbf{u}} - \bar{\mathbf{u}} \otimes \bar{\mathbf{u}} . \quad (3.10)$$

The residual kinetic energy is then obtained by taking the half of the trace of $\boldsymbol{\tau}^R$

$$k_r = \frac{1}{2} \text{tr}(\boldsymbol{\tau}^R) , \quad (3.11)$$

and the anisotropic residual-stress tensor is defined as [46]

$$\boldsymbol{\tau}^r = \boldsymbol{\tau}^R - \frac{2}{3} k_r \mathbf{I} . \quad (3.12)$$

By plugging equation (3.12) into equation the filtered Navier–Stokes equations (3.9), we obtain an alternative form as

$$\begin{aligned} \frac{\partial \bar{\mathbf{u}}}{\partial t} + \nabla \cdot (\bar{\mathbf{u}} \otimes \bar{\mathbf{u}}) &= -\nabla \bar{p} + \nabla \cdot (\nu(\nabla \bar{\mathbf{u}} + (\nabla \bar{\mathbf{u}})^T)) + \bar{\mathbf{f}} - \nabla \cdot \boldsymbol{\tau}^r , \\ \nabla \cdot \bar{\mathbf{u}} &= 0 . \end{aligned} \quad (3.13)$$

where $\bar{p} = \bar{p}_k + \frac{2}{3} k_r$ denotes the modified pressure. This new set of equations can be closed by modeling the residual-stress tensor $\boldsymbol{\tau}^r$ according to the linear eddy viscosity assumption (Section 3.2) and the filtered Navier–Stokes equations are then solved numerically for $\bar{\mathbf{u}}$ and \bar{p} (Chapter 4). As mentioned earlier, the filter operation does not appear directly in the filtered Navier–Stokes equations (3.9); however, it appears indirectly in the model for $\boldsymbol{\tau}^r$.

3.2 Eddy viscosity models

When modeling turbulence with a LES, the linear eddy viscosity assumption – introduced by Boussinesq in 1877 [52] – is predominantly used as it considerably reduces modeling effort compared to other choices [43]. This assumption is mathematically analogous to the

viscous stress relation for Newtonian fluids (see equation (2.7)), and relates the anisotropic residual-stress tensor to the filtered rate of strain

$$\bar{\mathbf{S}} = \frac{1}{2}(\nabla \bar{\mathbf{u}} + (\nabla \bar{\mathbf{u}})^T) \quad , \quad (3.14)$$

as [46]

$$\boldsymbol{\tau}^r \simeq -2\nu_{SGS}\bar{\mathbf{S}} \quad . \quad (3.15)$$

Here, ν_{SGS} denotes the sub-grid scale viscosity that is needed as the dissipative eddies are not captured with a grid coarser than the Kolmogorov length scale. By analogy to Prandtl's mixing length hypothesis [47], this artificial viscosity is modeled as a function of a model constant C_m , the characteristic filter width Δ and a differential operator D_m , which acts on the filtered velocity field $\bar{\mathbf{u}}$

$$\nu_{SGS} = (C_m \Delta)^2 D_m(\bar{\mathbf{u}}) \quad . \quad (3.16)$$

In the beginning of this chapter, we stated that the filter operation does not appear directly in the filtered Navier–Stokes equation but only indirectly in the model for $\boldsymbol{\tau}^r$. In the context of the high-order DG discretization, the filter just appears in form of its width, specified in equation (4.37). Hence, there is no explicit specification of the filter operation neither in the LES equations nor in the eddy-viscosity model. However, if desired, one could construct a consistent filter for any eddy viscosity model. Denoting the energy spectrum for an arbitrary flow as $E(\kappa)$ for a DNS and $\bar{E}(\kappa)$ for a LES, an appropriate filter function would be defined as [46]

$$\hat{G}_{SGS}(\kappa) = \left(\frac{\bar{E}(\kappa)}{E(\kappa)} \right)^{1/2} \quad . \quad (3.17)$$

This thought will no longer be pursued, instead we will apply equation (3.15) on the filtered Navier–Stokes equations (3.13), which yields

$$\begin{aligned} \frac{\partial \bar{\mathbf{u}}}{\partial t} + \nabla \cdot (\bar{\mathbf{u}} \otimes \bar{\mathbf{u}}) &= -\nabla \bar{p} + \nabla \cdot (\nu(\nabla \bar{\mathbf{u}} + (\nabla \bar{\mathbf{u}})^T)) + \bar{\mathbf{f}} - \nabla \cdot (-2\nu_{SGS}\bar{\mathbf{S}}) \quad , \\ \nabla \cdot \bar{\mathbf{u}} &= 0 \quad . \end{aligned} \quad (3.18)$$

By using the definition of the rate of strain, equation (3.18) can be rewritten as

$$\begin{aligned} \frac{\partial \bar{\mathbf{u}}}{\partial t} + \nabla \cdot (\bar{\mathbf{u}} \otimes \bar{\mathbf{u}}) &= -\nabla \bar{p} + \nabla \cdot ((\nu + \nu_{SGS})(\nabla \bar{\mathbf{u}} + (\nabla \bar{\mathbf{u}})^T)) + \bar{\mathbf{f}} \quad , \\ \nabla \cdot \bar{\mathbf{u}} &= 0 \quad . \end{aligned} \quad (3.19)$$

In the following, we discuss four static eddy-viscosity models and compare them using desirable properties [43], which can be reviewed in Table 3.2. For the ease of implementation, the differential operator D_m of an eddy-viscosity model should be defined locally and only

Table 3.2: Desirable properties for the differential operator of an eddy viscosity model [43]

P1	A positive quantity which involves only locally defined velocity gradients
P2	Cubic behavior near solid boundaries
P3	Zero for any two-dimensional flow
P4	Zero for axisymmetric or isotropic expansion/contraction

use local velocity gradients. A non-local differential operator would require the computation of the two-point correlation, which is expensive for complex geometries. Moreover, even though negative values could be related to the backscatter phenomenon (see [46] for more information), D_m should be strictly positive due to stability issues in complex flow configurations [38]. Both properties mentioned are collectively referred to as Property P1. Furthermore, in case of flow in near-wall regions, turbulent stresses should vanish due to the no-slip condition. As reported in [5], turbulent stresses, and thus the differential operator should decay as the cube of the distance to the solid boundary (Property P2). Moreover, the differential operator should tend to zero for every non-turbulent flow configurations, e.g., the case of pure shear or solid rotation. Even though two-dimensional turbulence has been evidenced, it lacks the important vortex-stretching mechanism [33]. Additionally, since the smallest resolved scales interact with sub-grid scales which are random like and purely three-dimensional, they cannot remain two-dimensional. Therefore, it seems appropriate that the differential operator should tend to zero for every two-dimensional flow (Property P3). A similar analysis shows that the turbulent stresses should tend to zero in case of isotropic and axisymmetric expansion (or contraction) (Property P4).

In the following subsections we investigate whether or not the static eddy-viscosity models satisfy the desired properties recalled in Table 3.2. It needs to be mentioned that these properties are not based on any mathematical theory, but they still seem desirable in a physical and a numerical sense.

In the following discussion, the index notation and the Einstein summation rule are used for the ease of presentation if not stated otherwise. Here, the entry of the i th row and j th column of matrix $\bar{\mathbf{S}}$ is denoted as \bar{S}_{ij} and repeated indices are implicitly summed over, i.e., $\bar{S}_{ij}\bar{S}_{ij} = \sum_i \sum_j \bar{S}_{ij}\bar{S}_{ij}$.

3.2.1 The Smagorinsky model

Smagorinsky proposed in [54] an eddy viscosity model that is based on the filtered rate of strain

$$D_m = D_s = \sqrt{2\bar{S}_{ij}\bar{S}_{ij}} . \quad (3.20)$$

By construction, the Smagorinsky model produces turbulent stresses as soon as velocity gradients exist. The model satisfies P1 as it only uses locally defined velocity gradients

and $\sqrt{2\bar{S}_{ij}\bar{S}_{ij}} \in \mathbb{R}^+$. The behavior near a solid boundary, which without loss of generality is located in the $(x_1, x_2 = 0, x_3)$ plane, can be examined using Taylor expansions. The resolved velocity near the boundary can be approximated as

$$\bar{\mathbf{u}} = \begin{bmatrix} ax_2 + \mathcal{O}(x_2^2) \\ b_1 x_2 + b_2 x_2^2 + \mathcal{O}(x_2^3) \\ cx_2 + \mathcal{O}(x_2^2) \end{bmatrix}, \quad (3.21)$$

where the coefficients a , b_1 , b_2 , and c are functions of space and time ($a = a(x_1, x_3, t)$). The first order term for \bar{u}_2 vanishes as the incompressibility constraint

$$\nabla \cdot \bar{\mathbf{u}}|_{x_2=0} = (a_{x_1}x_2 + b_1 + 2b_2x_2 + c_{x_3}x_2 + \mathcal{O}(x_2^2))|_{x_2=0} = 0, \quad (3.22)$$

is only satisfied if $b_1 = 0$. Note that subscripts denote partial derivatives, e.g., $a_{x_1} = \partial a / \partial x_1$ and that we will denote $b_2 = b$ in the following. The filtered velocity gradient $\bar{\mathbf{L}}$ can then be calculated as

$$\bar{\mathbf{L}} = \nabla \bar{\mathbf{u}} = \begin{bmatrix} a_{x_1}x_2 + \mathcal{O}(x_2^2) & a + \mathcal{O}(x_2) & a_{x_3}x_2 + \mathcal{O}(x_2^2) \\ b_{x_1}x_2^2 + \mathcal{O}(x_2^3) & 2bx_2 + \mathcal{O}(x_2^2) & b_{x_3}x_2^2 + \mathcal{O}(x_2^3) \\ c_{x_1}x_2 + \mathcal{O}(x_2^2) & c + \mathcal{O}(x_2) & c_{x_3}x_2 + \mathcal{O}(x_2^2) \end{bmatrix}. \quad (3.23)$$

Since S_{12} and S_{32} are of order $\mathcal{O}(1)$, $D_m = \mathcal{O}(1)$ as long as $a \neq 0$ or $c \neq 0$. In order to achieve a proper near-wall behavior, the Van Driest exponential damping function [60] has been extensively used in the early LES research [42]. This modification brought a significant improvement over the standard Smagorinsky model; however, it requires an arduous implementation. Even with the damping function, the altered Smagorinsky model has a near-wall behavior of $\mathcal{O}(x_2^2)$ and not the desired $\mathcal{O}(x_2^3)$. Moreover, the model constant must be changed for the Smagorinsky model in combination with the Van Driest damping function in order to sustain turbulence in a channel flow [39].

We investigate the Smagorinsky model on P3 by applying it on the case of pure shear and solid rotation. The latter is apparent in a flow configuration where the velocity profile is given as

$$\bar{\mathbf{u}} = \begin{bmatrix} x_2 & -x_1 & 0 \end{bmatrix}^T.$$

This velocity profile leads to a zero strain rate:

$$\bar{\mathbf{S}} = \begin{bmatrix} 0 & 0 & 0 \\ 0 & 0 & 0 \\ 0 & 0 & 0 \end{bmatrix},$$

and it follows that D_s vanishes in this case. The former is apparent in a flow of a viscous fluid between two infinite plates separated by the distance h_c , where one moves with the

velocity u_c , and the other one stagnates. Neglecting pressure gradients the steady state solution for the velocity is given as

$$\bar{\mathbf{u}} = \begin{bmatrix} \frac{x_2}{h_c} u_c & 0 & 0 \end{bmatrix}^T .$$

It follows that

$$\bar{\mathbf{S}} = \begin{bmatrix} 0 & \frac{u_c}{h_c} & 0 \\ 0 & 0 & 0 \\ 0 & 0 & 0 \end{bmatrix} ,$$

and thus

$$D_s = \sqrt{2} \frac{u_c}{h_c} \neq 0 .$$

Hence, the turbulent stress does not vanish for every two-dimensional flow configuration, and thus P3 is not fulfilled. Last, we investigate the Smagorinsky model on P4. If the resolved velocity field is in axisymmetric expansion or contraction, the velocity gradient tensor can be diagonalised as [43]

$$\bar{\mathbf{L}} = \begin{bmatrix} \beta & 0 & 0 \\ 0 & -\alpha & 0 \\ 0 & 0 & -\alpha \end{bmatrix} ,$$

where α is negative for an expansion and positive for a contraction. Since the velocity gradient tensor is a diagonal matrix, it follows that $\bar{\mathbf{S}} = \bar{\mathbf{L}}$ and $D_s = \sqrt{2(\beta^2 + 2\alpha^2)} \neq 0$. In case of isotropic expansion or contraction, $\beta = \alpha$, and thus $D_s = \sqrt{6\alpha^2} \neq 0$. Hence, P4 is not fulfilled and the Smagorinsky model satisfies just one of the four desirable properties.

3.2.2 The Vreman model

The filtering approach in the LES is different to the statistical approach used in the RANS simulation (for more information the reader is referred to [46]). The residual-stress tensor $\tau_{ij}^{\text{RANS}} = \langle u'_i u'_j \rangle$ in the RANS simulation satisfies three realizability conditions, introduced in [62]:

$$\begin{aligned} \tau_{ii}^{\text{RANS}} &\geq 0 & i \in \{1, 2, 3\} &, \\ |\tau_{ij}^{\text{RANS}}| &\leq (\tau_{ii}^{\text{RANS}} \tau_{jj}^{\text{RANS}})^{1/2} & i, j \in \{1, 2, 3\} &, \\ \det(\boldsymbol{\tau}^{\text{RANS}}) &\geq 0 & &. \end{aligned} \quad (3.24)$$

These properties generally hold for any positive (semidefinite) matrix as shown in [45]. The development of the Vreman model was highly motivated by the desire to construct an eddy viscosity model that fulfills the three realizability conditions (3.24). If satisfied, the

residual kinetic energy introduced in equation (3.11) is a positive quantity at any location for an arbitrary velocity field. We do not examine the derivation of the Vreman model, but the reader is referred to [61] for a detailed description. The Vreman model reads as

$$D_m = D_v = \begin{cases} 0, & \text{if } \bar{L}_{ij}\bar{L}_{ij} = 0 \\ \sqrt{\frac{\mathcal{L}_{11}\mathcal{L}_{22}-\mathcal{L}_{12}^2+\mathcal{L}_{11}\mathcal{L}_{33}-\mathcal{L}_{13}^2+\mathcal{L}_{22}\mathcal{L}_{33}-\mathcal{L}_{23}^2}{\bar{L}_{ij}\bar{L}_{ij}}}, & \text{otherwise} \end{cases}, \quad (3.25)$$

where $\mathcal{L} = \bar{\mathbf{L}}^T \bar{\mathbf{L}}$. It is easy to derive that D_v is zero for the case of pure shear; however, $D_v = \sqrt{\frac{1}{2}}$ for the case of solid rotation, and thus P3 is not fulfilled. The Vreman model does not meet property P4, but in contrast to the Smagorinsky model it vanishes in near-wall regions. However, D_v vanishes with $\mathcal{O}(x_2)$ and not as desired as the cube of the distance to the wall. Like the Smagorinsky model, the Vreman model just satisfies P1.

3.2.3 The WALE Model

Nicoud stated in [42] that the Smagorinsky model relates the sub-grid dissipation to the strain rate of the smallest resolved scales; however, it does not take the filtered rotation rate

$$\bar{\boldsymbol{\Omega}} = \frac{1}{2}(\nabla \bar{\mathbf{u}} - (\nabla \bar{\mathbf{u}})^T), \quad (3.26)$$

into account. In order to take better care of regions where vorticity dominates irrotational strain, the wall-adapting local eddy-viscosity (WALE) model has been proposed. Nicoud based his model on the traceless symmetric part of the square of the velocity gradient tensor $\tilde{\mathcal{L}} = \bar{\mathbf{L}} \bar{\mathbf{L}}$:

$$\chi_{ij} = \frac{1}{2}(\tilde{\mathcal{L}}_{ij} + \tilde{\mathcal{L}}_{ji}) - \frac{1}{3}\delta_{ij}\tilde{\mathcal{L}}_{kk}, \quad (3.27)$$

where the Kronecker $\boldsymbol{\delta}$ is defined as

$$\delta_{ij} = \begin{cases} 0, & \text{if } i \neq j \\ 1, & \text{if } i = j \end{cases}. \quad (3.28)$$

Using $\bar{\boldsymbol{\Omega}}$ and $\bar{\mathbf{S}}$, equation (3.27) can be rewritten as

$$\chi_{ij} = \bar{S}_{ik}\bar{S}_{kj} + \bar{\Omega}_{ik}\bar{\Omega}_{kj} - \frac{1}{3}\delta_{ij}(\bar{S}_{mn}\bar{S}_{mn} - \bar{\Omega}_{mn}\bar{\Omega}_{mn}). \quad (3.29)$$

In order to have a model that is not affected by any coordinate translation or rotation, the WALE model is based on the second invariant of $\boldsymbol{\chi}$, which is finite and proportional to $\chi_{ij}\chi_{ij}$ [42]. It is easy to examine that $\chi_{ij}\chi_{ij}$ behaves like $\mathcal{O}(x_2^2)$ near a solid boundary. A natural choice of D_w would then be $(\chi_{ij}\chi_{ij})^{3/2}$; however this quantity has a unit of $1/s^6$

and must therefore be scaled (see [42] for more information). The final WALE model, which yields the correct near-wall behavior of $\mathcal{O}(x_2^3)$, is then given as

$$D_m = D_w = \frac{(\chi_{ij}\chi_{ij})^{2/3}}{(\bar{S}_{ij}\bar{S}_{ij})^{5/2} + (\chi_{ij}\chi_{ij})^{5/4}} . \quad (3.30)$$

Just like D_v , the differential operator of the WALE model D_w vanishes in case of pure shear, but not in case of solid rotation [43]. D_w vanishes in case of isotropic expansion or contraction, but not for the more general axisymmetric case, and thus P4 is not fulfilled. The WALE model uses local velocity gradients and is strictly positive, and thus meets property P1.

3.2.4 The σ -model

The development of the σ -model was motivated by fulfilling all properties from Table 3.2. The model is based on the three singular values of the filtered velocity gradient $\bar{\mathbf{L}}$ denoted by $\sigma_1 \geq \sigma_2 \geq \sigma_3 \geq 0$. By definition, those values are always positive and equal the square root of the eigenvalues of $\mathcal{L} = \bar{\mathbf{L}}^T \bar{\mathbf{L}}$. The singular values are computed after the method introduced by Hasan et al. in [17] as this method is self-contained and does not require the use of an external library. First the three invariants of \mathcal{L} are computed as

$$\mathcal{I}_1 = \text{tr}(\mathcal{L}) , \quad (3.31)$$

$$\mathcal{I}_2 = \frac{1}{2}(\text{tr}(\mathcal{L})^2 - \text{tr}(\mathcal{L}\mathcal{L})) , \quad (3.32)$$

$$\mathcal{I}_3 = \det(\mathcal{L}) . \quad (3.33)$$

Next, the following angles from the above invariants are computed as

$$\alpha_1 = \frac{\mathcal{I}_1^2}{9} - \frac{\mathcal{I}_3}{3} , \quad (3.34)$$

$$\alpha_2 = \frac{\mathcal{I}_2^3}{27} - \frac{\mathcal{I}_1\mathcal{I}_2}{6} + \frac{\mathcal{I}_3}{2} , \quad (3.35)$$

$$\alpha_3 = \frac{1}{3} \arccos \frac{\alpha_2}{\alpha_1^{3/2}} . \quad (3.36)$$

Last, the singular values can be computed by using both the invariants and the angles

$$\sigma_1 = \left(\frac{\mathcal{I}_1}{3} + 2\sqrt{\alpha_1} \cos \alpha_3 \right)^{1/2} , \quad (3.37)$$

$$\sigma_2 = \left(\frac{\mathcal{I}_1}{3} - 2\sqrt{\alpha_1} \cos \left(\frac{\pi}{3} + \alpha_3 \right) \right)^{1/2} , \quad (3.38)$$

$$\sigma_3 = \left(\frac{\mathcal{I}_1}{3} - 2\sqrt{\alpha_1} \cos \left(\frac{\pi}{3} - \alpha_3 \right) \right)^{1/2} . \quad (3.39)$$

The smallest singular value σ_3 equals zero if and only if either a row or a column of \mathbf{L} is zero up to a rotation of the coordinate system – making σ_3 an indicator for P3. In the case of an axysimmetric expansion/contraction, the singular values are either $\sigma_1 > \sigma_2 = \sigma_3$ or $\sigma_1 = \sigma_2 > \sigma_3$ and in the case of isotropic expansion/contraction $\sigma_1 = \sigma_2 = \sigma_3$ making the quantity $(\sigma_1 - \sigma_2)(\sigma_2 - \sigma_3)$ a well-suited indicator for P4. It can be shown that the singular values have a near-wall behavior of [43]

$$\begin{aligned}\sigma_1 &= \mathcal{O}(x_2^0) & , \\ \sigma_2 &= \mathcal{O}(x_2^1) & , \\ \sigma_3 &= \mathcal{O}(x_2^2) & ,\end{aligned}\tag{3.40}$$

and thus the product $\sigma_3(\sigma_1 - \sigma_2)(\sigma_2 - \sigma_3)$ has a near-wall behavior of $\mathcal{O}(x_2^3)$ which satisfies P2. Scaling the model with $1/\sigma_1^2$ to obtain a unit of $1/s$ (see [43] for further information) leads to the final σ -model

$$D_m = D_\sigma = \frac{\sigma_3(\sigma_1 - \sigma_2)(\sigma_2 - \sigma_3)}{\sigma_1^2} .\tag{3.41}$$

The σ -model is to the best of the author's knowledge the only local eddy viscosity model that satisfies all properties given in Table 3.2.

3.2.5 Model constants and summary of the local eddy viscosity models

In the former sections, we have shown different differential operators D_m that can be used for an edddy viscosity model and stated that the characteristic filter width is proportional to the grid size. It has yet to be determined how to choose the filter constants C_m . An asymptotic value for the Smagorinsky model can be obtained by assuming isotropic homogenous turbulence. In [35], Lilly found that C_s can be related to the Kolmogorov constant with

$$C_s = \frac{\left(\frac{2}{3}C_k\right)^{3/4}}{\pi} .\tag{3.42}$$

This leads to a Smagorinsky constant $C_s \approx 0.165$ if assuming $C_k \approx 1.6$ [43]. Theoretical analysis similar to Lilly's procedure cannot be conducted for more complex eddy viscosity models and the model constant must be determined by performing numerical experiments. In Chapter 5, we show that the determination of an appropriate model constant is the major challenge of turbulence modeling with local eddy viscosity models. The properties and model constants of the four local eddy viscosity models are summarized in Table 3.3 [43].

3.2.6 A dynamic eddy viscosity model

In the 1990s, Germano proposed an eddy viscosity model (based on the local Smagorinsky model) [14] that computes a model constant dynamically in regards to space and time. To

Table 3.3: Properties of the four local eddy viscosity models [43]

Model	Smagorinsky [54]	Vreman [61]	WALE [42]	σ [43]
D_m	3.20	3.25	3.30	3.41
Model constant	$C_s \approx 0.165$	$C_v \approx 0.28$	$C_w \approx 0.50$	$C_\sigma \approx 1.35$
Near-wall behavior	$\mathcal{O}(x_2^0)$	$\mathcal{O}(x_2^1)$	$\mathcal{O}(x_2^3)$	$\mathcal{O}(x_2^3)$
Vanishes for solid rotation	Yes	No	No	Yes
Vanishes for pure shear	No	Yes	Yes	Yes
Vanishes in axisymmetric case	No	No	No	Yes
Vanishes in isotropic case	No	No	Yes	Yes
Meets P1	✓	✓	✓	✓
Meets P2			✓	✓
Meets P3				✓
Meets P4				✓

achieve this, two different filters, namely the grid filter \bar{G} and the test filter \tilde{G} are used. The two filter must fulfill the restriction that $\Delta > \bar{\Delta}$. Finally, we denote the product of the two filters as $\tilde{G} = \tilde{G}\bar{G}$ and apply it to the incompressible Navier–Stokes equations

$$\frac{\partial \tilde{\bar{u}}}{\partial t} + \nabla \cdot (\tilde{\bar{u}} \otimes \tilde{\bar{u}}) = -\nabla \tilde{\bar{p}} + \nabla \cdot (\nu(\nabla \tilde{\bar{u}} + (\nabla \tilde{\bar{u}})^T)) + \tilde{\bar{f}} - \nabla \cdot \mathbf{T}^R , \quad (3.43)$$

where the twice filtered residual-stress tensor is defined as [14]

$$T_{ij}^R = \widetilde{\bar{u}_i \bar{u}_j} - \widetilde{\bar{u}_i} \widetilde{\bar{u}_j} . \quad (3.44)$$

The stresses that are resolved for the grid filter but not for the test filter can then be computed as

$$\mathcal{L}_{ij}^R = \widetilde{\bar{u}_i \bar{u}_j} - \widetilde{\bar{u}_i} \widetilde{\bar{u}_j} . \quad (3.45)$$

Using the standard residual stress tensor (3.10), \mathcal{L} can be rewritten as

$$\mathcal{L}_{ij}^R = T_{ij}^R - \widetilde{\tau}_{ij}^R . \quad (3.46)$$

Note that \mathcal{L}_{ij}^R is known in terms of \bar{u}_i . Both anisotropic residual-stress tensors are then modeled with a Smagorinsky-like approach [14]

$$\tau_{ij}^R \simeq -2c\bar{\Delta}^2 \bar{S}_{ij} |\bar{S}| \quad (3.47)$$

$$T_{ij}^R \simeq -2c\tilde{\bar{\Delta}}^2 \tilde{\bar{S}}_{ij} |\tilde{\bar{S}}| , \quad (3.48)$$

where $|\bar{\mathbf{S}}| = \sqrt{2\bar{S}_{mn}\bar{S}_{mn}}$, and $|\tilde{\mathbf{S}}| = \sqrt{2\tilde{S}_{mn}\tilde{S}_{mn}}$. The coefficient C^2 from equation (3.16) has been replaced by c , allowing for negative values to account for the backscatter phenomenon. The anisotropic part of \mathcal{L}_{ij}^R can then be modeled as [46]

$$\mathcal{L}_{ij}^r = T_{ij}^r - \widetilde{\tau_{ij}^r} \simeq -2c(\widetilde{\Delta}^2 \tilde{S}_{ij} |\tilde{\mathbf{S}}| - \overline{\Delta}^2 \widetilde{\bar{S}_{ij}} |\bar{\mathbf{S}}|) = c M_{ij}^r . \quad (3.49)$$

When using LES, both \mathcal{L}_{ij}^r and M_{ij}^r are known, and an optimal c can then be determined as

$$c = \frac{M_{ij}^r \mathcal{L}_{ij}^r}{M_{mn}^r M_{mn}^r} \quad (3.50)$$

By construction, the dynamic model assumes similar sub-grid scale stresses for the grid and the test level. In comparison to the local eddy viscosity model, this model can account for the backscatter phenomenon, which was found to be important in some cases [34]. Germano showed that the ratio $\widetilde{\Delta}/\overline{\Delta} > 1$ is crucial as small values lead to numerical instabilities and large values relate stresses of large energy-containing structures to the sub-grid scale stresses. Due to high implementation afford and instabilities issues due to the backscatter phenomenon [38], we will not consider the dynamic model in this work. For more information on this model the reader is referred to [46] and [14].

Chapter 4

Numerical discretization

As mentioned in Chapter 1, the incompressible Navier–Stokes equations have not been solved analytically yet; however, by discretization of equation (3.19) in both space and time, a numerical solution for the resolved velocity and the modified pressure can be obtained. Spatial discretization is obtained by using the DG method and temporal discretization is obtained by using the high-order dual splitting method introduced in [24]. In the following, we apply the spatial and temporal discretization methods on the filtered Navier–Stokes equations. Furthermore, we review the concept of implicit large eddy simulation – an alternative turbulence modeling approach. Lastly, we discuss the implementation of our method, using the finite element library `deal.II` [2].

4.1 Temporal discretization

The dual splitting scheme is based on the backward differentiation formula (BDF) – an implicit method for the numerical integration of ordinary differential equations – in combination with a projection method introduced by Chorin [6]. In the following, we review the basic concept of the projection method and then apply the high-order dual splitting method to equation (3.19).

4.1.1 High-order dual splitting scheme

The high-order dual splitting scheme solves the filtered Navier–Stokes equations in three substeps. This scheme is used in [18] and [12] in combination with the DG method. Krank et al. showed in [28] its performance on under-resolved turbulent flows.

Convective step The first step deals with the nonlinear convective term and the body force \mathbf{f} , where an explicit treatment is used for efficiency reasons. A first intermediate velocity field is obtained by evaluating the following equation

$$\frac{\gamma_0 \hat{\mathbf{u}} - \alpha_0 \mathbf{u}^n - \alpha_1 \mathbf{u}^{n-1}}{\Delta t} = -\beta_0 \nabla \cdot \mathbf{F}(\mathbf{u}^n) - \beta_1 \mathbf{F}(\mathbf{u}^{n-1}) + \mathbf{f}^{n+1} , \quad (4.1)$$

Table 4.1: Coefficients of time integration scheme and extrapolation scheme

Coefficients	1st Order	2nd Order
γ_0	1	3/2
α_0	1	2
α_1	0	-1/2
β_0	1	2
β_1	0	-1

where a second order scheme has been used for both the BDF time integration and the extrapolation of the convective flux. Note that the implicit Euler method (a first order time integration scheme [4]) is used in the first time step. The coefficients for (4.1) are listed in Table 4.1.

Pressure and projection step Next, the pressure at the end of the time step as well as a second intermediate (divergence-free) velocity are computed from the following formulas

$$\frac{\gamma_0 \hat{\mathbf{u}} - \gamma_0 \hat{\mathbf{u}}}{\Delta t} = \nabla p^{n+1} \quad , \quad (4.2)$$

$$\nabla \cdot \hat{\mathbf{u}} = 0 \quad . \quad (4.3)$$

A Poisson equation for the pressure is obtained by taking the divergence of equation (4.2)

$$\nabla^2 p^{n+1} = -\frac{\gamma_0}{\Delta t} \nabla \cdot \hat{\mathbf{u}} \quad . \quad (4.4)$$

The second intermediate velocity is then computed by using the Leray projection, i.e., projecting the intermediate velocity $\hat{\mathbf{u}}$ on divergence-free field

$$\hat{\mathbf{u}} = \hat{\mathbf{u}} - \frac{\Delta t}{\gamma_0} \nabla p^{n+1} \quad . \quad (4.5)$$

Viscous step Last, the viscous term is taken into account. It is treated implicitly due to stability reasons

$$\frac{\gamma_0 \mathbf{u}^{n+1} - \gamma_0 \hat{\mathbf{u}}}{\Delta t} = \nabla \cdot ((\nu + \nu_{SGS})(\nabla \mathbf{u}^{n+1} + (\nabla \mathbf{u}^{n+1})^T)) \quad . \quad (4.6)$$

Boundary conditions On Γ_D we specify the value for the resolved velocity \mathbf{u} and the derivative of the pressure p [23] as

$$\mathbf{u} = g_{\mathbf{u}} \quad , \quad (4.7)$$

$$\nabla p^{n+1} \cdot \mathbf{n} = - \left[\frac{\partial \mathbf{u}^{n+1}}{\partial t} + \sum_{q=0}^{J_p-1} \beta_q ((\mathbf{u}^{n-q} \cdot \nabla) \mathbf{u}^{n-q} + \nu \nabla \times (\nabla \times \mathbf{u}^{n-q}) - \mathbf{f}^{n+1}) \right] \cdot \mathbf{n} \quad , \quad (4.8)$$

where the Neumann condition (4.8) arises from the momentum equation (2.4). Decoupling of pressure and velocity in equation (4.8) is obtained by treating the convective and viscous step explicitly with an extrapolation scheme; the coefficients β_q are defined in Table 4.1. Note that the viscous term in the pressure boundary equation (4.8) is an approximation to the exact viscous term as we neglect the influence of the sub-grid scale viscosity

$$\begin{aligned}\nabla \cdot ((\nu + \nu_{SGS})(\nabla \mathbf{u} + (\nabla \mathbf{u})^T)) &= (\nu + \nu_{SGS})\nabla^2 \mathbf{u} + (\nabla(\nu_{SGS} + \nu)) \cdot ((\nabla \mathbf{u} + (\nabla \mathbf{u})^T)) \\ &\simeq (\nu + \nu_{SGS})\nabla^2 \mathbf{u} \simeq \nu\nabla^2 \mathbf{u} \\ &= -\nu \underbrace{\nabla \times (\nabla \times \mathbf{u})}_{\text{rotational form}} .\end{aligned}\quad (4.9)$$

The rotational form is obtained by using a vector identity and the incompressibility constraint

$$\nabla^2 \mathbf{u} = \nabla(\nabla \cdot \mathbf{u}) - \nabla \times (\nabla \times \mathbf{u}) = -\nabla \times (\nabla \times \mathbf{u}) .\quad (4.10)$$

Karniadakis et. al [24] and Orszag et. al [44] have shown that the rotational formulation effectively reduces boundary divergence errors and that its use is essential in obtaining a high-order time accurate splitting scheme. On the Neumann boundary Γ_N , we generally set both the modified pressure and the derivative of the velocity to zero [59]

$$\begin{aligned}(\nabla \mathbf{u} + (\nabla \mathbf{u})^T) \cdot \mathbf{n} &= 0 , \\ p &= g_p .\end{aligned}\quad (4.11)$$

Gravemeier et. al showed in [15] that this boundary condition eventually leads to an unstable numerical scheme as vortices leaving the computational domain provoke reverse flow. Therefore, we will use this advanced boundary condition if necessary, e.g, for the backward facing step problem considered in Section 5.2.

4.2 Spatial discretization

Using the DG method, the physical domain Ω is approximated by the numerical domain $\Omega_h \subset \mathbb{R}^d$ that is either a polygon ($d = 2$) or a polyhedral ($d = 3$) with its boundary denoted by $\partial\Omega_h = \Gamma$. Let $\mathcal{T} = \{K\}$ be a triangulation of Ω_h into nonoverlapping elements K . Two adjacent cells K^+ and K^- with unit pointing outward normal vector \mathbf{n}^- and \mathbf{n}^+ , respectively, share an interior facet $F = \partial K^+ \cap \partial K^-$. A boundary facet, on the other hand, lies on Γ . Following [10], we define an average operator $\{\{\cdot\}\}$ and the jump operators $[\cdot]$ and $[\cdot]$ as $\{\{\mathbf{u}\}\} = \frac{\mathbf{u}^- + \mathbf{u}^+}{2}$, $[\mathbf{u}] = \mathbf{u}^- \otimes \mathbf{n}^- + \mathbf{u}^+ \otimes \mathbf{n}^+$, and $[\mathbf{u}] = \mathbf{u}^- - \mathbf{u}^+$, respectively. Using DG methods, the exact solution of a problem $\psi(x, t)$ is approximated by $\psi_h(x, t) \in \Psi_h$, where Ψ_h is the finite element function space defined as

$$\Psi_h = \{\psi_h \in L^2(\Omega_h) : \psi_h \in P_k(K) \quad \forall K \in \mathcal{T}\} .\quad (4.12)$$

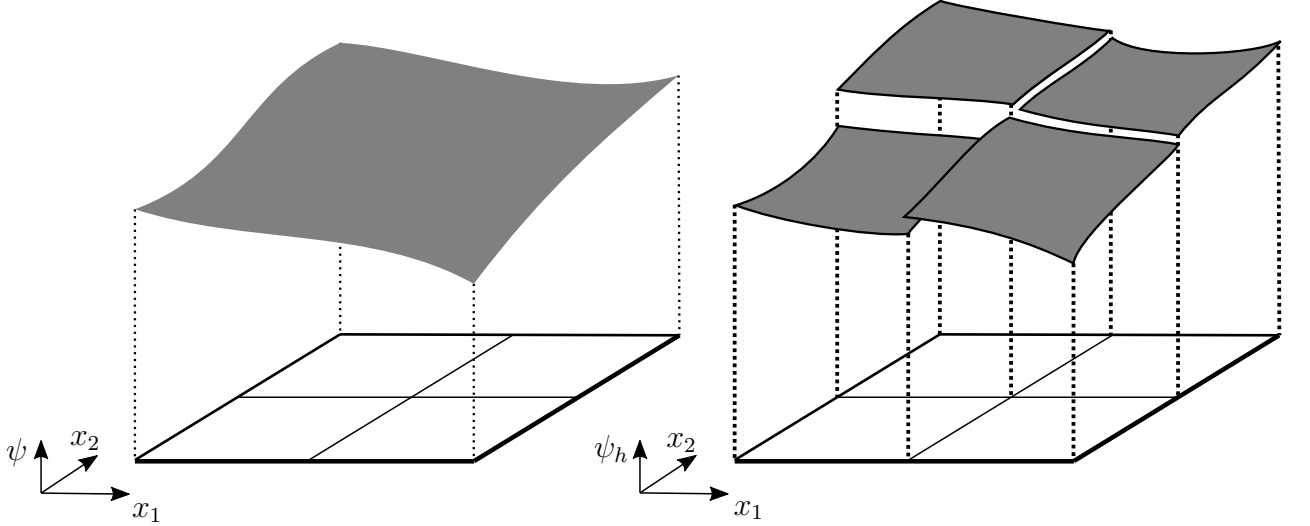


Figure 4.1: Comparison of smooth function ψ to piecewise smooth function ψ_h [8]

Here, $P_k(K)$ denotes the vector space of polynomials with real coefficients and degree less than or equal to k on the element K . In this work, we use a mixed-order formulation, where the velocity and the pressure are approximated by polynomials of order $k_u = k+1$ and $k_p = k$, respectively. Optimal rates of convergence for this approach have been demonstrated in [10].

The Hilbert space of square-integrable functions L^2 , with inner product $(\cdot, \cdot)_{L^2}$ and norm $\|\cdot\|_{L^2}$, is defined as

$$(u, v)_{L^2} = \int uv \quad u, v \in L^2 \quad , \\ \|u\|_{L^2} = (u, u)_{L^2} \quad u \in L^2 \quad . \quad (4.13)$$

Due to the discontinuity of the solution at interior facets – illustrated in Figure 4.1 – an integral over the numerical domain Ω_h is defined as the sum of integrals over the nonoverlapping elements K :

$$(u, v)_{\Omega_h} = \sum_{K \in \mathcal{T}} (u, v)_K = \sum_{K \in \mathcal{T}} \int_K uv d\Omega_h \quad .$$

In the following, we will review the spatial discretization of the three sub-steps obtained by the splitting method based on the work in [8].

4.2.1 Convective step

The weak formulation of the convective step is obtained by multiplying equation (4.1) with a test function $\mathbf{v}_h \in \mathcal{V}_h$, where \mathcal{V}_h is a multidimensional version of the vector space (4.12)

defined as

$$\mathcal{V}_h = \left\{ \boldsymbol{v}_h \in [L^2(\Omega_h)]^3 : \boldsymbol{v}_h \in [P_k(K)]^3 \quad \forall K \in \mathcal{T} \right\} . \quad (4.14)$$

Integration over the the numerical domain Ω_h yields

$$\begin{aligned} \sum_{K \in \mathcal{T}} \left(\boldsymbol{v}_h, \frac{\gamma_0 \hat{\boldsymbol{u}}_h - \alpha_0 \boldsymbol{u}_h^n - \alpha_1 \boldsymbol{u}_h^{n+1}}{\Delta t} \right)_K &= - \sum_{K \in \mathcal{T}} \beta_0 (\boldsymbol{v}_h, \nabla \cdot \boldsymbol{F}(\boldsymbol{u}_h^n))_K \\ &\quad - \sum_{K \in \mathcal{T}} \beta_1 (\boldsymbol{v}_h, \nabla \cdot \boldsymbol{F}(\boldsymbol{u}_h^{n-1}))_K \\ &\quad + \sum_{K \in \mathcal{T}} (\boldsymbol{v}_h, \boldsymbol{f}^{n+1})_K . \end{aligned} \quad (4.15)$$

Multidimensional integration by parts is an essential tool for obtaining an useful weak formulation – applying it to the convective term $\boldsymbol{F}(\boldsymbol{u}_h)$ yields

$$\begin{aligned} (\boldsymbol{v}_h, \nabla \cdot \boldsymbol{F}(\boldsymbol{u}_h))_K &= \int_K \boldsymbol{v}_h (\nabla \cdot \boldsymbol{F}(\boldsymbol{u}_h)) dK \\ &= \int_K \nabla \cdot (\boldsymbol{F}(\boldsymbol{u}_h)^T \boldsymbol{v}_h) dK - \int_K \nabla \boldsymbol{v}_h : \boldsymbol{F}(\boldsymbol{u}_h) dK \\ &= \int_{\partial K} \boldsymbol{v}_h \cdot (\boldsymbol{F}^* \cdot \boldsymbol{n}) \partial K - \int_K \nabla \boldsymbol{v}_h : \boldsymbol{F}(\boldsymbol{u}_h) dK \\ &= (\boldsymbol{v}_h, \boldsymbol{F}^* \cdot \boldsymbol{n})_{\partial K} - (\nabla \boldsymbol{v}_h, \boldsymbol{F}(\boldsymbol{u}_h))_K , \end{aligned} \quad (4.16)$$

where \boldsymbol{F}^* denotes the numerical flux. The solution is discontinuous between element boundaries; however, continuity is enforced by the numerical flux as it uses information from both elements adjacent to the particular facet. The reader is referred to [18] for an extensive discussion on numerical fluxes. In this work, we consider the local Lax–Friedrichs flux [18] given as

$$\boldsymbol{F}^* = \{ \{ \boldsymbol{F}(\boldsymbol{u}_h) \} \} + \frac{\Lambda}{2} [\![\boldsymbol{u}_h]\!] . \quad (4.17)$$

Here, Λ is defined as $\Lambda = \max(2|\boldsymbol{u}^- \cdot \boldsymbol{n}|, 2|\boldsymbol{u}^+ \cdot \boldsymbol{n}|)$ [28]. Using equation (4.16), the final weak formulation of the convective step reads as: Find $\hat{\boldsymbol{u}}_h \in \mathcal{V}_h$ such that

$$\begin{aligned} \left(\boldsymbol{v}_h, \frac{\gamma_0 \hat{\boldsymbol{u}}_h - \alpha_0 \boldsymbol{u}_h^n - \alpha_1 \boldsymbol{u}_h^{n+1}}{\Delta t} \right)_K &= + \beta_0 (\nabla \boldsymbol{v}_h, \boldsymbol{F}(\boldsymbol{u}_h^n))_K - \beta_0 (\boldsymbol{v}_h, \boldsymbol{F}^{*,n} \cdot \boldsymbol{n})_{\partial K} \\ &\quad + \beta_1 (\nabla \boldsymbol{v}_h, \boldsymbol{F}(\boldsymbol{u}_h^{n-1}))_K - \beta_1 (\boldsymbol{v}_h, \boldsymbol{F}^{*,n-1} \cdot \boldsymbol{n})_{\partial K} \\ &\quad + (\boldsymbol{v}_h, \boldsymbol{f}^{n+1})_K \quad \forall \boldsymbol{v}_h \in \mathcal{V}_h, \forall K \in \mathcal{T} . \end{aligned} \quad (4.18)$$

Due to the discontinuous nature of the DG discretization, the summation over all elements K can be omitted and instead we obtain an independent equation for every element K .

4.2.2 Pressure and projection step

For the pressure step, we transform the underlying Poisson problem (4.4) into a system of first order equations [3]

$$\begin{aligned} -\nabla \cdot \boldsymbol{\sigma} &= \frac{\gamma_0}{\Delta t} \nabla \cdot \hat{\mathbf{u}} \quad , \\ \boldsymbol{\sigma} &= \nabla p^{n+1} \quad , \end{aligned} \quad (4.19)$$

using the auxiliary variable $\boldsymbol{\sigma}$. Following the procedure in [3], where the auxiliary variable σ_h has been eliminated, the final weak formulation (primal formulation) reads as follows: Find $p_h \in \Psi_h$ such that

$$\begin{aligned} & + (\nabla \psi_h, \nabla p_h)_K - (\nabla \psi_h, (p_h - p_h^*) \mathbf{n})_{\partial K} \\ & - (\psi_h, \boldsymbol{\sigma}_h^* \cdot \mathbf{n})_{\partial K} = \left(\nabla \psi_h, \frac{\gamma_0}{\Delta t} \hat{\mathbf{u}}_h \right)_K - \left(\psi_h, \frac{\gamma_0}{\Delta t} \mathbf{u}_h^* \right)_{\partial K} \quad \forall \psi_h \in \Psi_h, \forall K \in \mathcal{T} . \end{aligned} \quad (4.20)$$

The superscript $n + 1$ for the pressure has been omitted for the ease of notation. The numerical flux \mathbf{u}_h^* is defined as the average value of the adjacent cells, i.e. $\mathbf{u}_h^* = \{\{\mathbf{u}_h\}\}$ [10]. Moreover, we consider the symmetric interior penalty Galerkin (SIPG) method [3] that defines the two remaining numerical fluxes as follows

$$\begin{aligned} p_h^* &= \{\{p_h\}\} \quad , \\ \boldsymbol{\sigma}_h^* &= \{\{\nabla p_h\}\} - \tau [\![p_h]\!] \quad . \end{aligned} \quad (4.21)$$

The second term on the right hand side is a stabilization term that restricts jumps between element boundaries and enforces continuity in a weak sense. The penalty parameter τ is defined in [53]. For more information on the SIPG method, the reader is referred to [53]. The weak formulation of the projection step reads as follows: Find $\hat{\mathbf{u}}_h \in \mathcal{V}_h$ such that

$$(\mathbf{v}_h, \hat{\mathbf{u}}_h)_K - (\mathbf{v}_h, \hat{\mathbf{u}}_h)_K = \left(\nabla \mathbf{v}_h, \frac{\Delta t}{\gamma_0} p_h^{n+1} \right)_K - \left(\mathbf{v}_h, \frac{\Delta t}{\gamma_0} p_h^{*,n+1} \mathbf{n} \right)_{\partial K} \quad \forall \mathbf{v}_h \in \mathcal{V}_h, \forall K \in \mathcal{T} . \quad (4.22)$$

The numerical flux is defined as [10] $p_h^{*,n+1} = \{\{p_h^{n+1}\}\}$.

4.2.3 Viscous step

The DG formulation of the viscous term is obtained by solving the following system of equations [9]

$$\begin{aligned} -\nabla \cdot \boldsymbol{\sigma} &= \frac{\gamma_0 \mathbf{u} - \gamma_0 \hat{\mathbf{u}}}{\Delta t} \\ \boldsymbol{\sigma} &= ((\nu + \nu_{SGS})(\nabla \mathbf{u} + (\nabla \mathbf{u})^T)) \end{aligned} \quad (4.23)$$

Both equations are multiplied by weighting functions and integration by parts is performed. The primal formulation reads as [9]: Find $\mathbf{u}_h \in \mathcal{V}_h$ such that

$$\begin{aligned} & + (\nabla \mathbf{v}_h, ((\nu + \nu_{SGS})(\nabla \mathbf{u}_h + (\nabla \mathbf{u})^T)))_K \\ & - (\nabla \mathbf{v}_h, ((\nu + \nu_{SGS})((\mathbf{u}_h - \mathbf{u}_h^*) \otimes \mathbf{n} - ((\mathbf{u}_h - \mathbf{u}_h^*) \otimes \mathbf{n})^T)))_K \\ & - (\mathbf{v}_h, \boldsymbol{\sigma}_h^* \cdot \mathbf{n})_{\partial K} = (\mathbf{v}_h, \mathbf{f})_K \quad \forall \mathbf{v}_h \in \mathcal{V}_h, \forall K \in \mathcal{T}, \end{aligned} \quad (4.24)$$

The numerical fluxes are computed as

$$\begin{aligned} \mathbf{u}_h^* &= \{\{\mathbf{u}_h\}\} , \\ \boldsymbol{\sigma}_h^* &= \nu^* \{\{\nabla \mathbf{u}_h + (\nabla \mathbf{u}_h)^T\}\} - \nu^* \tau ([\![\mathbf{u}_h]\!] + [\![\mathbf{u}_h]\!]^T) . \end{aligned} \quad (4.25)$$

The penalty parameter τ is again defined as in [53], and the numerical flux of the viscosity is defined as the harmonic mean of the adjacent cells

$$\nu^* = 2 \frac{(\nu + \nu_{SGS})^- (\nu + \nu_{SGS})^+}{(\nu + \nu_{SGS})^- + (\nu + \nu_{SGS})^+} \quad (4.26)$$

4.3 Instabilities and the implicit large eddy simulation

The combination of the DG discretization with the high-order dual splitting scheme has been reported and analyzed to yield instabilities [11, 12] for small time steps. Furthermore, Krank et al. [28] demonstrated a mass-conservation error arising from the continuity equation in the under-resolved limit. Based on the work made in [19, 56], Krank et al. [28] introduced two penalty terms in the projection step (4.22) to attack these instabilities. On the one hand, a jump penalty term should restrict jumps of the velocity field between element interfaces. On the other hand, a div-div penalty term should decrease the influence of the error in the continuity equation as the second intermediate velocity field is not exactly divergence-free. Recently, Fehn et al. showed [10] that the instabilities reported in [11, 12] could be treated by correct integration (by parts) of the right-hand side in the pressure step (4.20) and in the projection step (4.22).

However, the penalty terms introduced in [28] are still necessary as they tackle the other source of instability. Furthermore, the terms that were originally intended to stabilize the numerical scheme introduce numerical dissipation, and can therefore account for the lacking physical dissipation as the dissipative scales are not resolved when using LES. This leads to the widely used concept of implicit large eddy simulation (ILES). The reader is referred to [16] for an excessive discussion on implicit large eddy simulation. In this work the modified projection step reads as: Find $\hat{\mathbf{u}}_h \in \mathcal{V}_h$ such that

$$\begin{aligned} & + \underbrace{(\nabla \cdot \mathbf{v}_h, \tau_D \nabla \cdot \hat{\mathbf{u}}_h)_K}_{\text{div-div penalty}} + \underbrace{(\mathbf{v}_h, \tau_C [\![\hat{\mathbf{u}}_h]\!])_{\partial K}}_{\text{jump penalty}} \\ & + (\mathbf{v}_h, \hat{\mathbf{u}}_h)_K = (\mathbf{v}_h, \hat{\mathbf{u}}_h)_K - (\mathbf{v}_h, \frac{\Delta t}{\gamma_0} \nabla p_h^{n+1})_K \quad \forall \mathbf{v}_h \in \mathcal{V}_h, \forall K \in \mathcal{T}, \end{aligned} \quad (4.27)$$

where the div-div and the continuity parameter are defined as $\tau_D = \Delta t \|\hat{\hat{\mathbf{u}}}_h^{\text{mean}, K}\| h_{\text{eff}}$ and $\tau_C = \Delta t \|\hat{\hat{\mathbf{u}}}_h^{\text{mean}, K}\|$, respectively. The effective length scale is defined as

$$h_{\text{eff}} = \frac{V_K^{1/3}}{k+1} , \quad (4.28)$$

where V_K is the volume of the element K . The mean velocity within a given element K can be computed as

$$\|\hat{\hat{\mathbf{u}}}_h^{\text{mean}, K}\| = \frac{1}{V_K} \left\| \int_K \hat{\hat{\mathbf{u}}}_h d\Omega_h \right\| . \quad (4.29)$$

To the author's best knowledge, the ILES approach is widely used for under-resolved flows discretized by a DG scheme, whereas the eddy viscosity approach is rare. Marek et al. showed [37] that an eddy-viscosity model has the capacity to stabilize a DG scheme (using the same DG discretization of spatial derivative operators as is used in this work) – making numerical dissipation obsolete. In this work, we want to investigate if an eddy-viscosity turbulence model generally has the ability to stabilize a DG scheme, or if the combination of ILES and eddy-viscosity approach is more advantageous.

$$\begin{aligned} & + \underbrace{\left(\nabla \cdot \mathbf{v}_h, \tau_D \nabla \cdot \hat{\hat{\mathbf{u}}}_h \right)_K}_{\text{div-div penalty}} + \underbrace{\left(\mathbf{v}_h, \tau_C [\hat{\hat{\mathbf{u}}}_h] \right)_{\partial K}}_{\text{jump penalty}} \\ & + \left(\mathbf{v}_h, \hat{\hat{\mathbf{u}}}_h \right)_K = (\mathbf{v}_h, \hat{\hat{\mathbf{u}}}_h)_K - (\mathbf{v}_h, \Delta t \nabla p_h^{n+1})_K \quad \forall \mathbf{v}_h \in \mathcal{V}_h, \forall K \in \mathcal{T} , \end{aligned} \quad (4.30)$$

where the div-div and the continuity parameter are defined as $\tau_D = \Delta t \|\hat{\hat{\mathbf{u}}}_h^{\text{mean}, K}\| h_{\text{eff}}$ and $\tau_C = \Delta t \|\hat{\hat{\mathbf{u}}}_h^{\text{mean}, K}\|$, respectively. The effective length scale is defined as

$$h_{\text{eff}} = \frac{V_K^{1/3}}{k+1} , \quad (4.31)$$

where V_K is the volume of the element K and the mean velocity within a given element K can be computed as

$$\|\hat{\hat{\mathbf{u}}}_h^{\text{mean}, K}\| = \frac{1}{V_K} \left\| \int_K \hat{\hat{\mathbf{u}}}_h d\Omega_h \right\| . \quad (4.32)$$

4.4 Element shape and basis functions

In this section, we present the finite elements and the basis functions [8] that are used for this work. Furthermore, we demonstrate the transformation from arbitrary cells in the

physical space to a reference cell. Since turbulence is a three-dimensional phenomenon (see Chapter 3), we just consider hexahedral elements for which the multidimensional shape functions $N_i(\xi)$ are a product of one-dimensional Lagrange polynomials of order k

$$l_j^k(\xi) = \prod_{\substack{i=0, \\ i \neq j}}^k \frac{\xi - \bar{\xi}_i}{\bar{\xi}_j - \bar{\xi}_i} \quad \forall j = 0, \dots, k \quad , \quad (4.33)$$

$$N_i(\xi) = N_{i_1, i_2, i_3}(\xi) = \prod_{n=1}^3 l_{i_n}^k(\xi_n) \quad \text{where } i_n = 0, \dots, k, \forall n \in \{1, 2, 3\} \quad (4.34)$$

The nodes $\{\bar{\xi}_i\}$ are the Legendre–Gauss–Lobatto (LGL) nodes, which are in comparison to equidistant nodes more densely distributed towards the edges. The approximate solution ψ_h to ψ can be written as the sum of the contribution of each element ψ_h^e as

$$\psi_h(\mathbf{x}, t) = \bigoplus_{e=1}^{N_{el}} \psi_h^e(\mathbf{x}, t) \quad , \quad (4.35)$$

where ψ_h^e is obtained by multiplying the basis functions N_i^e with the nodal solution values at the LGL nodes

$$\psi_h^e(\mathbf{x}, t) = \sum_{i=1}^{N_{dofs,K}} N_i^e(\mathbf{x}) \psi_i^e(t) \quad . \quad (4.36)$$

The number of degrees of freedom in element K is denoted as $N_{dofs,K} = (k+1)^3$. In order to obtain $N_i^e(\mathbf{x})$, we need to define an affine mapping function for each element that assigns every point on the reference cell a point on the physical cell, i.e., $\mathbf{F}_m : \xi \mapsto \mathbf{x}$.

4.5 The characteristic filter width

In this section, a formula for the characteristic filter width is presented. This is of high importance when using a linear eddy viscosity model as the filter width scales the sub-grid scale viscosity (3.16). Since the grid serves as an implicit filter operation itself, the filter width should depend on the size of the grid, i.e., the size of the element K . When using DG methods, the polynomial order of the approximation k contributes to the effective mesh resolution as well. Therefore, a simple model for the filter width is [37]

$$\Delta = h_{\text{eff}} \quad , \quad (4.37)$$

where h_{eff} is defined in equation (4.31). This model is consistent with the finite volume approach as $\Delta = V_K^{1/3}$ for $k = 0$. Recently, Moura et al. investigated normalized Gaussian-

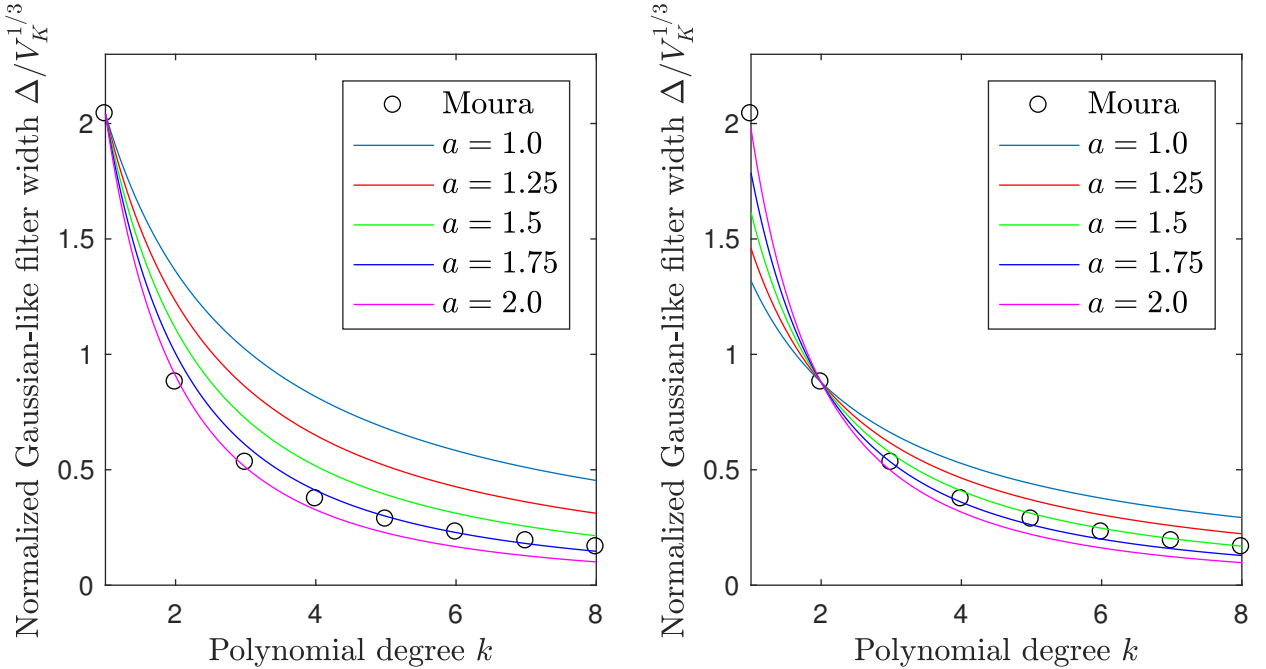


Figure 4.2: Curve fitting of normalized Gaussian-like filter width data [41]

like filter widths with numerical simulations. They performed several DNS for the Taylor–Green vortex [58] and then identified the smallest wavenumber κ_s whose amplitude scales by 99% when propagation over h_{eff} . A Gaussian like filter width can then be computed by setting $\kappa_s \approx \kappa_c$ (see equation (3.6)). We have analyzed this data by fitting the normalized Gaussian-like filter width data using the relation

$$\Delta(a) = \frac{V_K^{1/3}}{(k+1)^a} \quad \text{for } a \geq 1 , \quad (4.38)$$

where $\Delta(a) = \Delta$ for $a = 1$. On the left hand side of the Figure 4.2, the data has been fitted by requiring agreement with the data point at $k = 1$. On the right hand side, the same procedure has been done with the data point at $k = 2$. The data is best fitted for this approach when using the relation (4.38) with exponential coefficient $a = 1.75$. The analysis in [41] was performed for the linear advection equation with standard upwinding, and thus results of their work can not be directly adopted to our DG scheme. However, we will investigate the influence of different amplifying exponents a on numerical results in Chapter 5.

4.6 Implementation and computation of integrals

In this section, we show how the integrals arising from the weak formulation are solved numerically and address the implementation in general. The Gaussian quadrature rule

- constructed to yield an exact result for polynomials of degree $(2N_{qp} - 1)$ – is used to compute integrals numerically

$$\int_{[-1,1]^3} f(\boldsymbol{\xi}) d\boldsymbol{\xi} = \sum_{q=1}^{N_{qp}^3} w_q f(\boldsymbol{\xi}_q) \quad \forall f \in P_{2N_{qp}-1} \quad , \quad (4.39)$$

where N_{qp} is the number of Gauss points. The Gauss points, and weights are denoted as $\boldsymbol{\xi}_q$ and w_q , respectively (see [1] for more information). Since we want to solve integrals on the computational domain, we need to use the mapping introduced in the Subsection 4.4

$$\int_K f(\mathbf{x}) d\mathbf{x} = \int_{[-1,1]^3} f(\boldsymbol{\xi}) |\det(\mathbf{J})| d\boldsymbol{\xi} = \sum_{q=1}^{N_{qp}^3} w_q f(\boldsymbol{\xi}_q) |\det(\mathbf{J})| \quad \forall f \in P_{2N_{qp}-1} \quad , \quad (4.40)$$

where the Jacobian matrix $\mathbf{J} = \frac{\partial \mathbf{x}}{\partial \boldsymbol{\xi}}$ has been used. Here, we need to introduce an error e_a due to non-exact integration of $f(x)$ (since it is generally a polynomial of arbitrary order) known as aliasing

$$\int_{[-1,1]^3} g(\boldsymbol{\xi}) d\boldsymbol{\xi} = \sum_{q=1}^{N_{qp}^3} w_q g(\boldsymbol{\xi}_q) + e_a \quad \forall g \in P_k \text{ for } k > 2N_{qp} - 1 \quad . \quad (4.41)$$

If not stated otherwise, $N_{qp}^3 = (k + 1)^3$ Gauss quadrature points are used [8]. The computation of face-integrals is processed in a similar order, and can be reviewed in [8]. The implementation of this work is based on the C++ finite element library **deal.II** [2], which makes use of a parallel memory-efficient framework for finite element operator application [30]. The basic idea behind this approach is to apply the operation by a cell-wise quadrature instead of assembling and storing sparse matrices.

Chapter 5

Numerical results

In this chapter, the performance of LES with a combination of an ILES approach and an additional eddy viscosity model is investigated for the flow of a turbulent channel and a backward facing step. On the one hand, we want to examine if eddy viscosity models have the ability to stabilize a high-order DG scheme. On the other hand, we want to find the combination of ILES and the eddy viscosity approach that yields the best results, when compared with DNS solutions. Moreover, we want to investigate which of the four eddy viscosity models introduced in Chapter 3 is the best choice for high-order DG methods. The four different eddy viscosity models are abbreviated in the figure legends of this chapter according to Table 5.1.

Table 5.1: Abbreviations for the four eddy viscosity models

Eddy viscosity model	Smagorinsky	Vreman	WALE	σ
Abbreviation	smag	vrem	wale	sigm

5.1 Turbulent channel flow

The flow in a turbulent channel is one of the simplest wall-bounded turbulent flows, which might be one of the reason that it has been extensively studied. Moser et al. [40] conducted direct numerical simulations for three different friction Reynolds number

$$\text{Re}_\tau = \frac{u_\tau H}{2\nu} \in \{180, 395, 590\} . \quad (5.1)$$

Here, $H/2$ denotes the channel-half height. The friction velocity u_τ is defined as

$$u_\tau = \sqrt{\frac{\tau_w}{\rho}} , \quad (5.2)$$

where τ_w denotes the wall shear stress. In the following, the geometry and the mesh are described, and results of numerical solutions are presented.

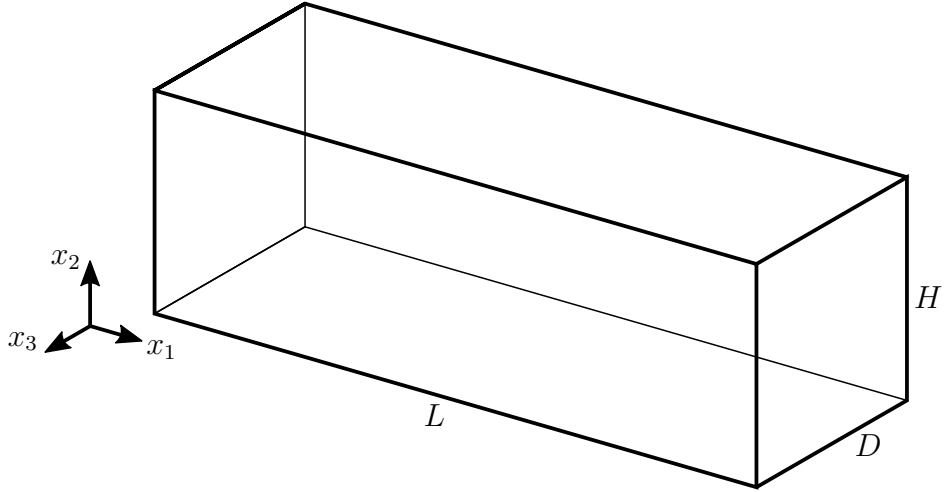


Figure 5.1: Computational domain of the turbulent channel

5.1.1 Computational domain

The geometry of the turbulent channel is visualized in Figure 5.1 and its length parameters are given in Table 5.2. An initially coarse grid (refine level $l = 0$) is uniformly refined (refine levels $l \geq 1$) as illustrated in Figure A.1. The mesh is then graded towards the no-slip boundaries according to the hyperbolic mesh mapping [28]

$$x_2 \mapsto f(x_2) = \frac{H}{2} \frac{\tanh(\gamma_{tc}(2x_2 - 1))}{\tanh(\gamma_{tc})} , \quad (5.3)$$

where γ_{tc} is given in Table 5.2. This treatment efficiently improves resolution of near-wall turbulent structures [28].

Table 5.2: Turbulent channel flow parameters

parameters	values
L	2π
H	2
D	π
γ_{tc}	1.8

5.1.2 Boundary and initial conditions

A velocity profile in x_1 -direction is described for $t = 0$ as

$$u_1(x_2, t = 0) = u_{\max}(1 - x_2^6)(1 + R) ,$$

where R is a random number between -0.5 and 0.5 . The initial velocities in $u_2(\mathbf{x}, t = 0)$ and $u_3(\mathbf{x}, t = 0)$ are set equal to zero. We choose periodic boundary conditions in x_1 - and x_3 -direction and no-slip boundary conditions in the x_2 -direction. As there is no inflow profile prescribed, the periodic flow needs to be driven by a volume force in x_1 -direction

$$\begin{aligned}\tilde{f}_1 &= \tau_w \frac{2}{H} \quad , \\ &= \frac{2u_\tau^2}{H\rho} = \frac{2\text{Re}_\tau^2 \nu^2}{H\rho(H/2)^2} = \frac{\text{Re}_\tau^2 \nu^2}{\rho} \quad .\end{aligned}$$

Using $\rho = 1$ and setting the viscosity to $\nu = \text{Re}_\tau$, the volume force is given as $\tilde{f}_1 = 1$.

5.1.3 Time advancement and post-processing

As mentioned in Chapter 4, time integration of our method is achieved by using the high-order dual splitting scheme. Due to the explicit treatment of the convective step (4.1), a time step has to be chosen smaller than the critical time step according to the Courant–Friedrichs–Lewy (CFL) condition

$$\Delta t_{\text{crit}} = \frac{\text{CFL} h_{\min}}{k^{3/2} \|\mathbf{u}_{\max}\|} \quad . \quad (5.4)$$

An estimate of a maximum velocity is denoted as $\|\mathbf{u}_{\max}\|$ and the minimum vertex distance is described with h_{\min} . The CFL number was chosen to be $\text{CFL} = 1.0$ for this flow problem.

A numerical simulation of a turbulent channel flow runs over a time interval of 50 seconds, where the first 30 seconds are discarded as an appropriate turbulent velocity field has to be developed. Statistical quantities can then be obtained for the remaining time interval. In order to compare our performance with the DNS of Moser et al. [40] (denoted as DNS MKM99), we need to compute mean velocity profiles, root mean square (RMS) values, and turbulent stresses. These statistical quantities are obtained by averaging the velocity profiles in time and in the homogeneous directions (x_1 -direction and x_3 -direction). Implemented is this method by first computing a spatial average value at a certain height x_2

$$\langle u_i(x_2, t) \rangle_{\text{hom}} = \frac{1}{LD} \int_0^L \int_{-D}^0 u_i(\mathbf{x}, t) dx_3 dx_1 \quad \text{for } i \in \{1, 2, 3\} \quad . \quad (5.5)$$

Additionally, we take the average in time

$$\langle u_i(t) \rangle = \frac{1}{t_{\text{comp}}} \int_{30s}^{50s} \langle u_i(x_2, t) \rangle_{\text{hom}} dt \quad \text{for } i \in \{1, 2, 3\} \quad . \quad (5.6)$$

In our implementation, this is done by adding up $\langle u_i(x_2, t) \rangle_{\text{hom}}$ at every tenth time step Δt and dividing the sum by the number of samples, i.e,

$$\langle u_i(t) \rangle \approx \frac{1}{N_{\text{samples}}} \sum_{j=0}^{N_{\text{samples}}} \langle u_i(x_2, t_j) \rangle_{\text{hom}} \quad (5.7)$$

The different quantities are then computed as

mean velocity: $\langle u_i \rangle$ for $i \in \{1, 2, 3\}$,

RMS-values: $\sqrt{\langle u_i'^2 \rangle} = \sqrt{\langle (u_i - \langle u_i \rangle)^2 \rangle} = \sqrt{\langle u_i^2 \rangle - \langle u_i \rangle^2}$ for $i \in \{1, 2, 3\}$,

Reynolds stress: $\langle u'_1 u'_2 \rangle = \langle (u_1 - \langle u_1 \rangle)(u_2 - \langle u_2 \rangle) \rangle = \langle u_1 u_2 \rangle - \langle u_1 \rangle \langle u_2 \rangle$.

Here the quantity \mathbf{u}' is meant to be a fluctuation from a statistical point of view. It is important to note the difference between the decomposition of the velocity in resolved and unresolved scales (3.3), and the decomposition in a statistical mean and a fluctuating part

$$\mathbf{u} = \langle \mathbf{u} \rangle + \mathbf{u}' . \quad (5.8)$$

5.1.4 Evaluation

In this subsection, we want to investigate two questions: On the one hand, we want to analyze if an eddy viscosity model has the ability to stabilize the numerical scheme without requiring further numerical stabilization terms. On the other hand, we want to investigate if the use of the ILES approach in combination with an eddy viscosity model is advantageous. We do so by performing numerical simulations for the turbulent channel at the Reynolds numbers $\text{Re}_\tau = 180, 395, 590$ in the respective order. For this flow, we know that the ILES approach yields excellent results [28]. For the ease of illustration, the obtained quantities from the numerical simulation are normalized as

$$\begin{aligned} (u_1)^+ &= u_1/u_\tau , \\ (u'_i)^+ &= \sqrt{\langle u_i'^2 \rangle}/u_\tau \quad \text{for } i \in \{1, 2, 3\} , \\ (u'_1 u'_2)^+ &= \langle u'_1 u'_2 \rangle/u_\tau^2 . \end{aligned}$$

For a better understanding, all RMS quantities are illustrated in one plot, however, $(u'_2)^+$ as well as $(u'_3)^+$ are shifted upwards for clarity (see Table 5.3).

Table 5.3: Offset for the quantities $(u'_2)^+$ and $(u'_3)^+$

Figure	5.2	5.3	5.4	5.5	5.6	5.7	5.7
Offset for $(u'_2)^+$	1.5	1.5	1.5	2.0	2.0	2.0	2.0
Offset for $(u'_3)^+$	1.5	1.5	1.5	3.0	3.0	3.0	3.0

Turbulent channel flow at $\text{Re}_\tau = 180$

The first question is investigated by evaluating numerical simulations for the flow of the lowest Reynolds number as it should be the easiest to stabilize. In the following, the combination of polynomial degree $k = k_u$ (and thus $k_p = k - 1$), and refinement level l used in a simulation will be denoted as a 2-tuple (l, k) . In order to correctly resolve the near-wall flow, we limit the numerical simulations of the turbulent channel to the

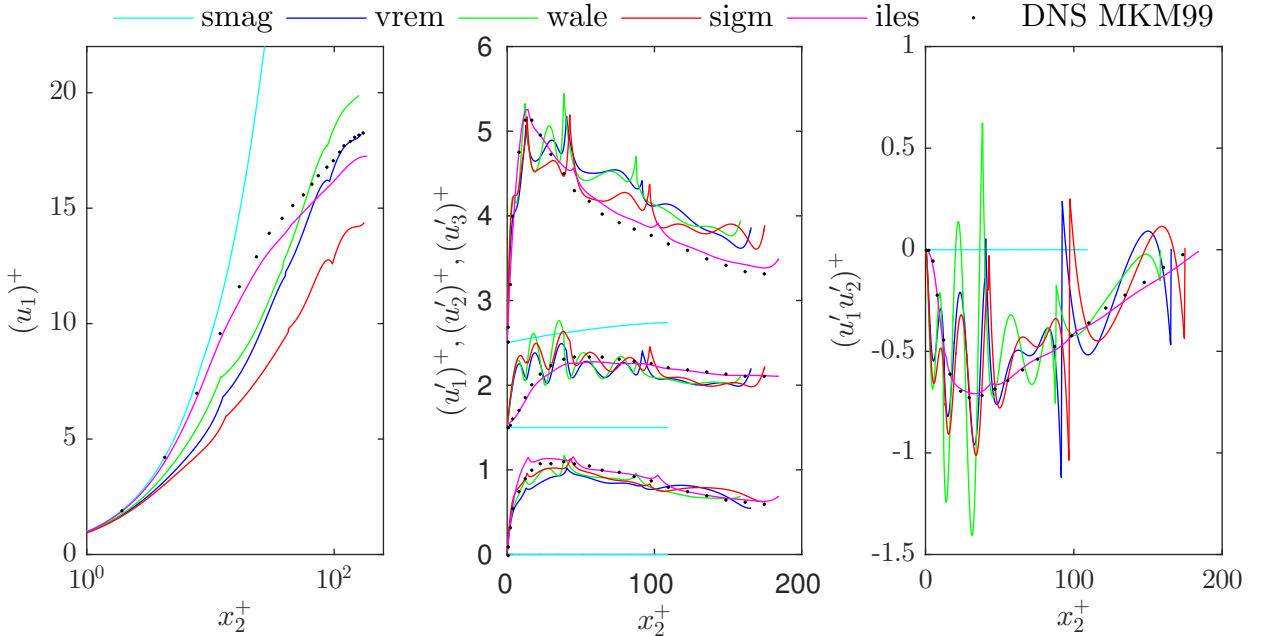


Figure 5.2: Turbulent channel flow $\text{Re}_\tau = 180$ without numerical dissipation and spatial discretization (3, 3)

refinement levels $l \geq 3$. Using a polynomial degree $k = 3$ and a global refinement level $l = 3$, we obtain the results illustrated in Figure 5.2. For the Smagorinsky model, the RMS quantities as well as the Reynolds stress are small compared to the DNS predictions. The strong fluctuations of the LES (for the RMS quantities and the Reynolds stress) with the eddy viscosity approach, using either the Vreman, WALE, or σ -model, indicate an almost unstable numerical scheme, whereas the ILES (denoted as 'None') is able to stabilize the DG scheme and gives predictions close to the DNS. Further investigations showed that the instability is increasing with increasing polynomial order k and increasing Reynolds number Re_τ – indicating that the eddy viscosity model is unable to stabilize a high-order DG scheme and that numerical dissipation is needed.

We further investigate if the accuracy of the ILES approach can be improved with an additional eddy viscosity model. In Figure 5.3, results for combinations of numerical dissipation with an eddy viscosity model are illustrated. The additive dissipation due to either of the four eddy viscosity model results in an increased mean velocity $(u_1)^+$. All four models in combination with numerical dissipation overpredict the mean velocity $(u_1)^+$; however, the Smagorinsky model is the only of the four eddy viscosity models that overpredicts this quantity for the approach without numerical dissipation (over the whole range of x_2^+) as well. Furthermore, this approach is not able to correctly resolve either the RMS values or the Reynolds stress. Both observations indicate that the Smagorinsky model adds to much dissipation – making the flow laminar. Therefore, we will not consider the Smagorinsky model in the following simulations of the turbulent channel flow. In order to decrease the added numerical dissipation for the remaining three models, we decrease

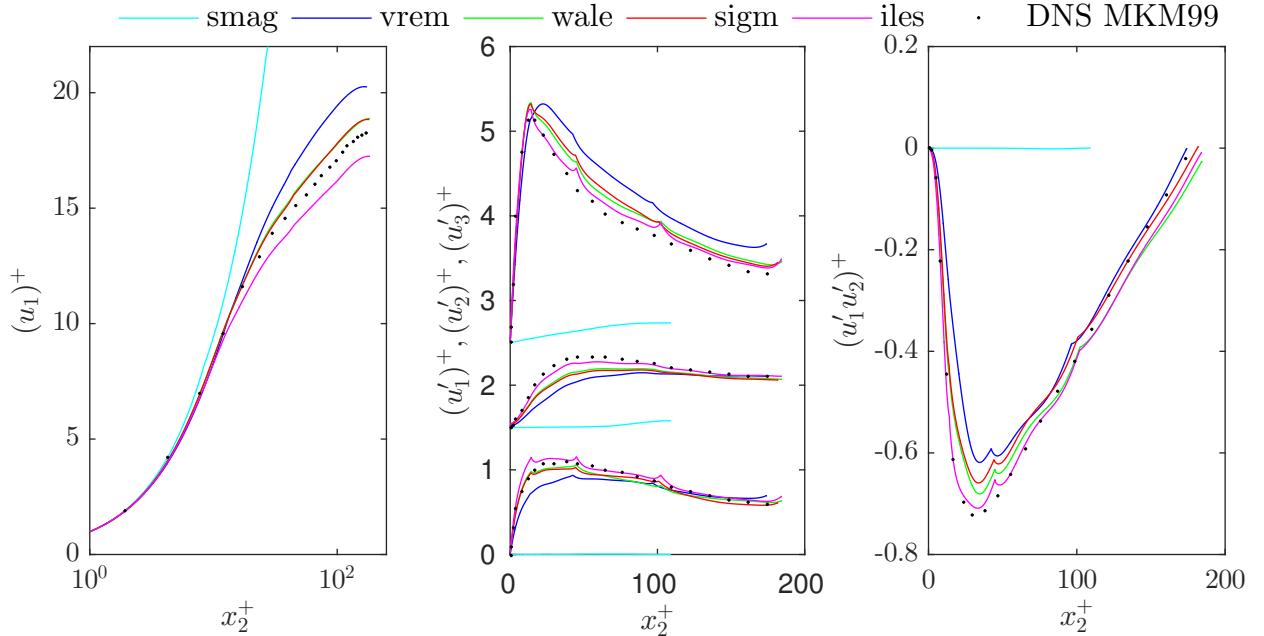


Figure 5.3: Turbulent channel flow $\text{Re}_\tau = 180$ with numerical dissipation and spatial discretization (3, 3)

the model constant C_m

$$\nu_{\text{SGS}} = (C_m^{\text{new}} \Delta)^2 D_m, \quad C_m^{\text{new}} = \frac{C_m}{\sqrt{2}} \quad . \quad (5.9)$$

This modification yields more accurate results; illustrated in Figure 5.4. The predictions of the mean velocity for the combination of ILES with the WALE-model as well as the σ -model are in excellent agreement with the DNS predictions, whereas the Vreman model still overpredicts this quantity. The agreement of RMS values and Reynolds stress slightly declines when adding an eddy viscosity model to the ILES approach. Next, we investigate if the combination of the two models is conferrable to turbulent channel flows of higher Reynolds numbers.

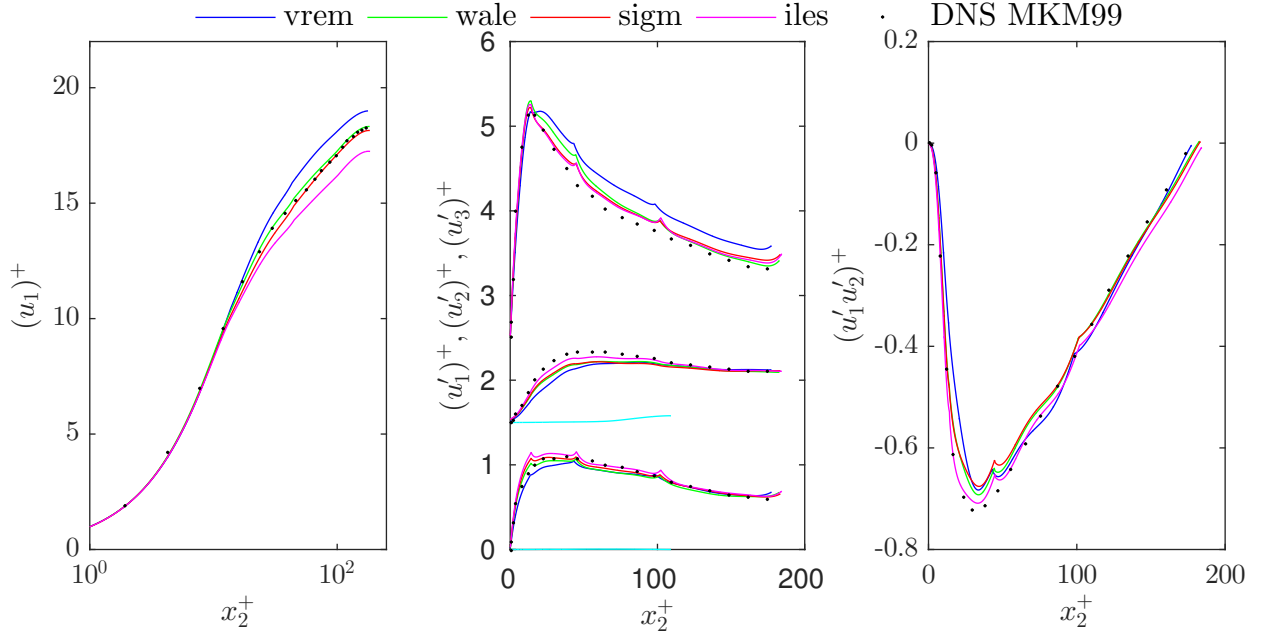


Figure 5.4: Turbulent channel flow $\text{Re}_\tau = 180$ with decreased eddy viscosity constant $C_m^{\text{new}} = C_m/\sqrt{2}$ and spatial discretization (3,3)

Turbulent channel flow at $\text{Re}_\tau = 395$

Numerical simulations for this flow have been carried out using the new model constant C_m^{new} . The graph of the mean-velocity in Figure 5.5 shows that the eddy viscosity influence should be further decreased, indicating that C_m is a function of the Reynolds number. Since fluctuations can be seen for every model, even for the pure ILES approach, we increase the polynomial degree to $k = 6$, resulting in a higher effective resolution. The simulation of the turbulent channel flow at $\text{Re}_\tau = 395$ with global refinement $l = 3$ and polynomial order $k = 6$ (Figure 5.6) yields good results for both the ILES approach and the combination approaches. Besides the results of the Reynolds stress, the additional eddy viscosity model could not improve the ILES approach; however, it stands to reason that a further decreased model constant C_m could improve the combination approaches.

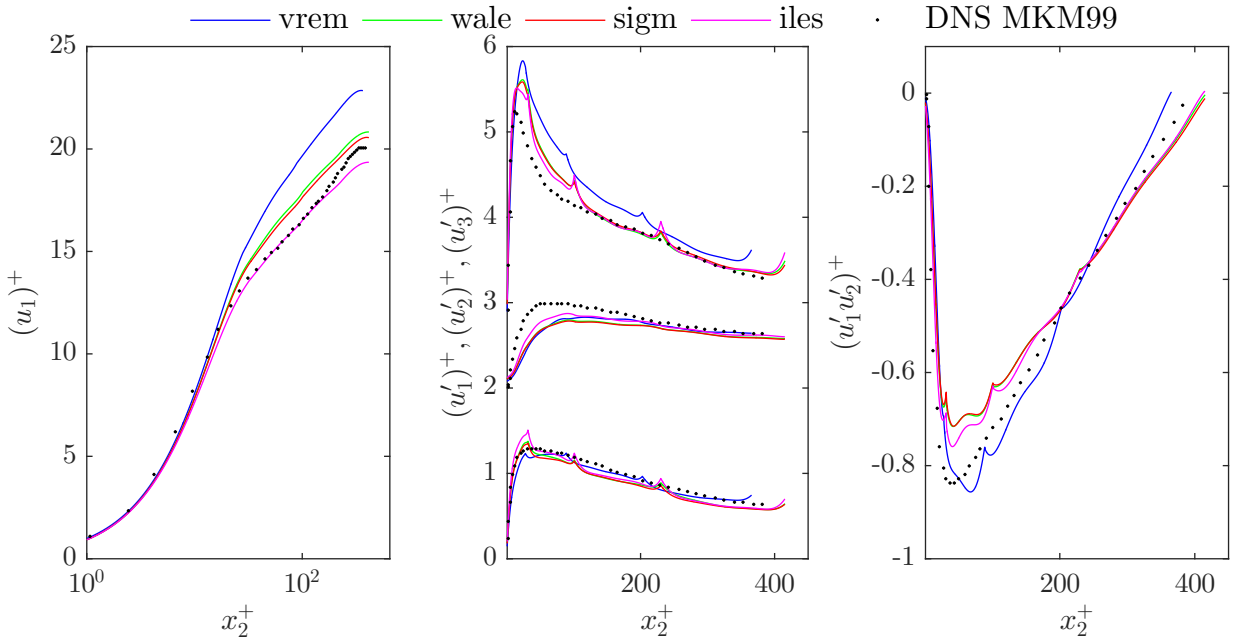


Figure 5.5: Turbulent channel flow $\text{Re}_\tau = 395$ with decreased eddy viscosity constant $C_m^{\text{new}} = C_m/\sqrt{2}$ and spatial discretization (3, 3)

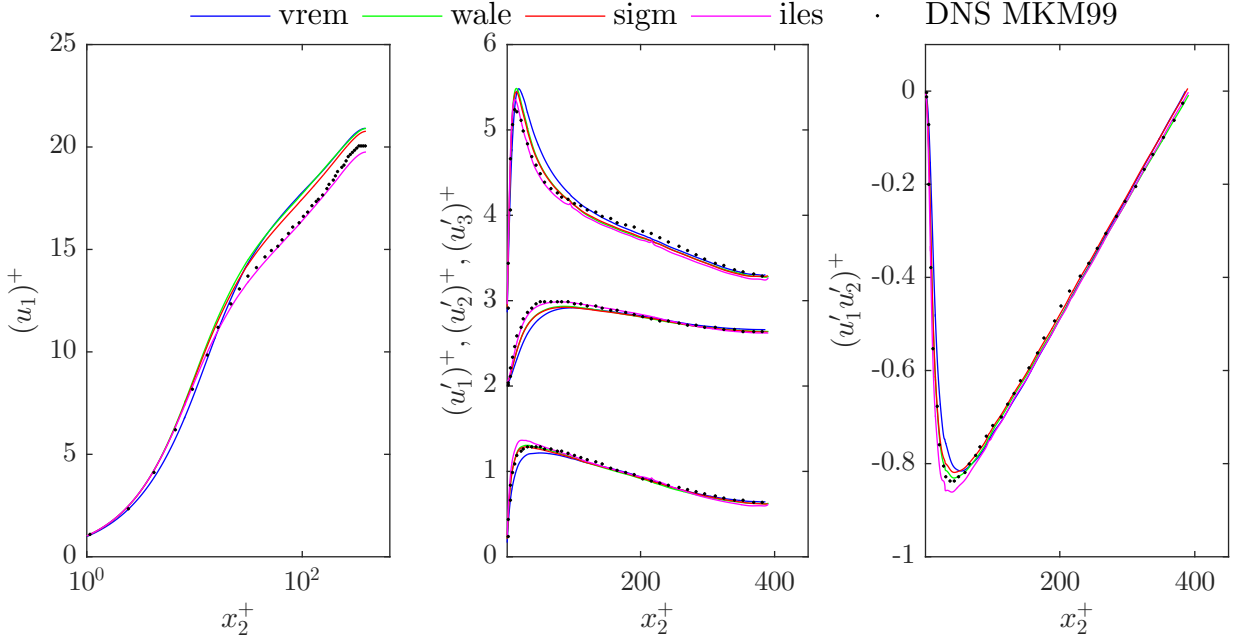


Figure 5.6: Turbulent channel flow $\text{Re}_\tau = 395$ with decreased eddy viscosity constant $C_m^{\text{new}} = C_m/\sqrt{2}$ and spatial discretization (3, 6)

Turbulent channel flow at $\text{Re}_\tau = 590$

Last, we want to perform numerical simulations for the turbulent channel flow at Reynolds number $\text{Re}_\tau = 590$. Using the model constant C_m^{new} , results of this problem are illustrated in Figure 5.7. Again, it seems that the model constant is chosen to be too high as the mean velocity is overpredicted for every eddy viscosity model. Therefore, we compare different model constants (see Table 5.4) for the σ -model. We choose this particular eddy viscosity model as it yielded the best results for the former simulation, and moreover, is the only model that satisfies all properties given in Table 3.2.

Table 5.4: Model constants C_σ for several σ -model

σ -model	sigm1	sigm2	sigm3
C_σ	1.35	$1.35/\sqrt{2}$	$1.35/2$

As can be seen in Figure 5.8, the lowest model constant $C_m = 1.35/2$ yields the best results, indicating that the model constant could even be further decreased. Therefore, for this flow problem the model constant for the σ -model yielding the best results lies in the range $1.35/2 > C_\sigma^{\text{opt}} > 0$, where $C_\sigma = 0$ is the pure ILES approach.

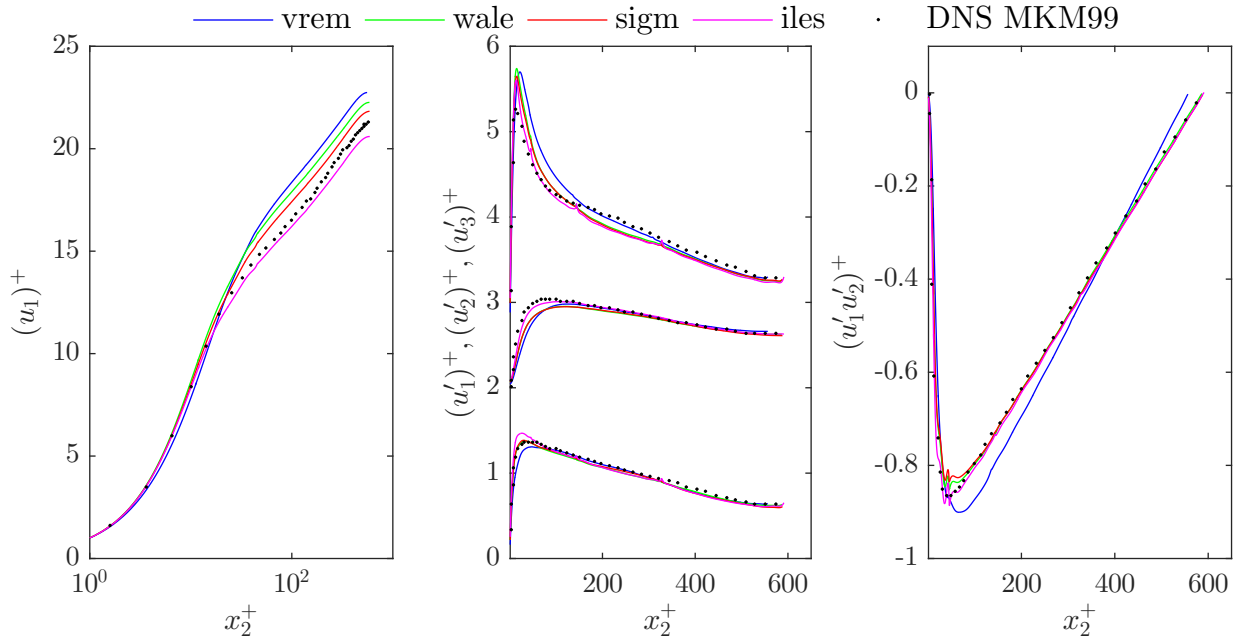


Figure 5.7: Turbulent channel flow $\text{Re}_\tau = 590$ with decreased eddy viscosity constant $C_m^{\text{new}} = C_m/\sqrt{2}$ and spatial discretization (3, 6)

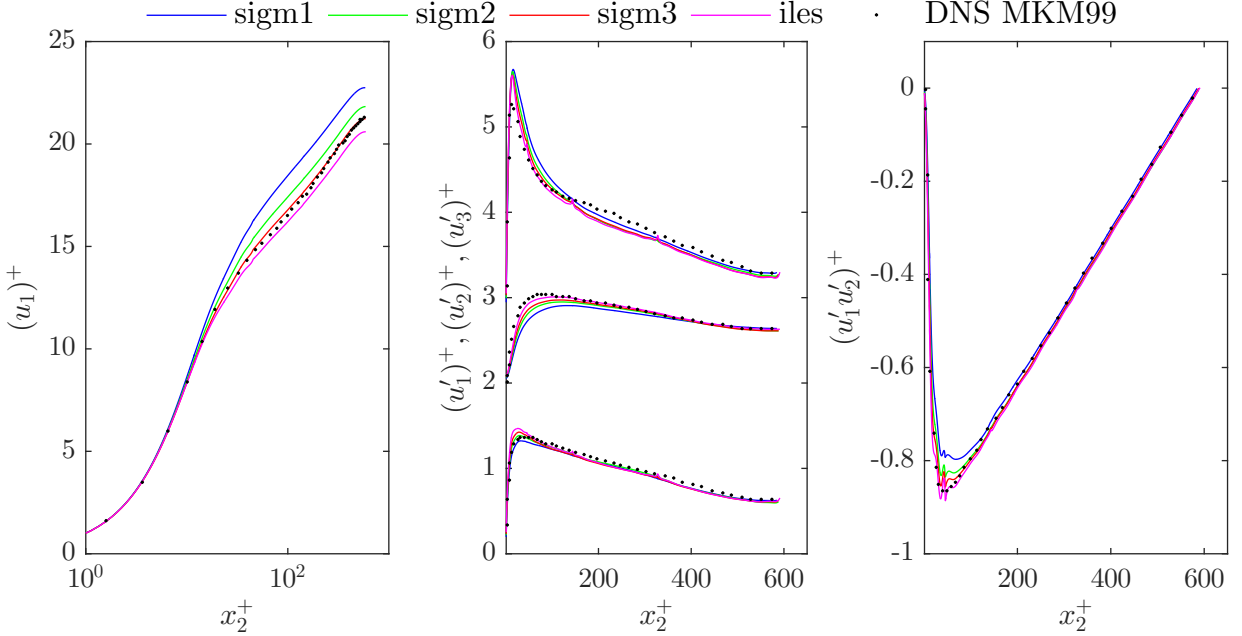


Figure 5.8: Turbulent channel flow $\text{Re}_\tau = 590$ for several σ -models and spatial discretization (3, 6)

5.1.5 Discussion of results

The observations made in this chapter show that the choice of the model constant C_m is crucial when adding an eddy viscosity model to the ILES approach. Due to the high computational effort when simulating turbulence, an intensive parameter study for C_m could not be carried out; however, evaluation of our numerical simulations indicate that C_m is a function of the polynomial degree k , the Reynolds number, and the refinement level l (or more specifically the grid size h). When an appropriate model constant has been chosen, the ILES approach could be slightly improved for this flow problem with the used resolution; however, choosing an inappropriate model constant results in significantly less accurate results. Moreover, our observations indicate that an eddy viscosity model is generally not able to stabilize a DG scheme without using further numerical stabilization terms. The Smagorinsky model was not able to reproduce either the correct RMS values or the Reynolds stress, when using its standard model constant given in Table 3.3. The WALE model as well as the σ -model show good results, that are significantly better than results obtained with the Vreman model. Given those observations, we conclude that an proper near-wall behavior is crucial when simulating wall-bounded turbulent flows with a combination approach of ILES and an eddy viscosity model.

It needs to be mentioned here, that the observations made in Section 4.5 indicate that the characteristic filter width should be modified similarly to how the model constant has been modified throughout this section. In this case, C_m could be a true constant.

5.2 Backward facing step

As a second test case, the flow over a backward facing step has been chosen. This flow problem involves the effect of separated boundary layers and an adverse pressure gradient, both of which the turbulent channel flow was missing. Furthermore, we have to deal with the issue of prescribing appropriate turbulent inflow data as the backward facing step does not have periodic boundary conditions in the streamwise direction.

The flow of a backward facing step with the Reynolds number based on the step height

$$Re_h = \frac{u_{\max} h}{\nu} = 5000 , \quad (5.10)$$

has been experimentally studied by Jovic et al. [20]. Here, u_{\max} and h denote the maximum velocity and the step height, respectively. A DNS under a similar configuration ($Re_h \approx 5100$) has been conducted by Le et al. [31] (denoted as DNS LMK97). Results of a large eddy simulation with a wall modeling approach have recently been presented in [29] (denoted as LES KW16). Simulations on similar turbulent flows using the large eddy simulation have been conducted in [13] and [21]. In the following, we describe the computational domain of the backward facing step and extensively discuss the importance of the velocity field prescribed at the inflow boundary.

5.2.1 Computational domain

Figure 5.9 shows the schematic view of the computational flow domain. The dimensions of the geometry are summarized in Table 5.5. The coordinate system is placed at the lower step corner as shown in Figure 5.9. The original mesh ($l = 0$) and one globally refined mesh ($l = 1$) are illustrated in Figure A.2. Both configurations have been modified according to the mapping

$$x_2 \mapsto f(x_2) = 6h + 4h \frac{\tanh(\gamma_{\text{ bfs}}(x_2 - 6h)/4h)}{\tanh \gamma_{\text{ bfs}}} \quad (5.11)$$

The expansion ratio ER of a backward facing step is defined as the rate of the height after the step to the height before the step. The backward facing step used in this simulation has an expansion ratio

$$\text{ER} = \frac{L_{x_2}}{L_{x_2} - h} = 1.2 \quad (5.12)$$

The length L_r denotes the reattachment length, i.e, for this flow problem, the position x_1 where $\partial u_1(x_1)/\partial x_2 = 0$.

5.2.2 Boundary and initial conditions

The initial velocity profile is set equal to zero, i.e., $\mathbf{u}(\mathbf{x}, t = 0) = \mathbf{0}$. Symmetry boundary conditions are prescribed at the top wall ($x_2 = L_{x_2}$) and outflow boundary conditions

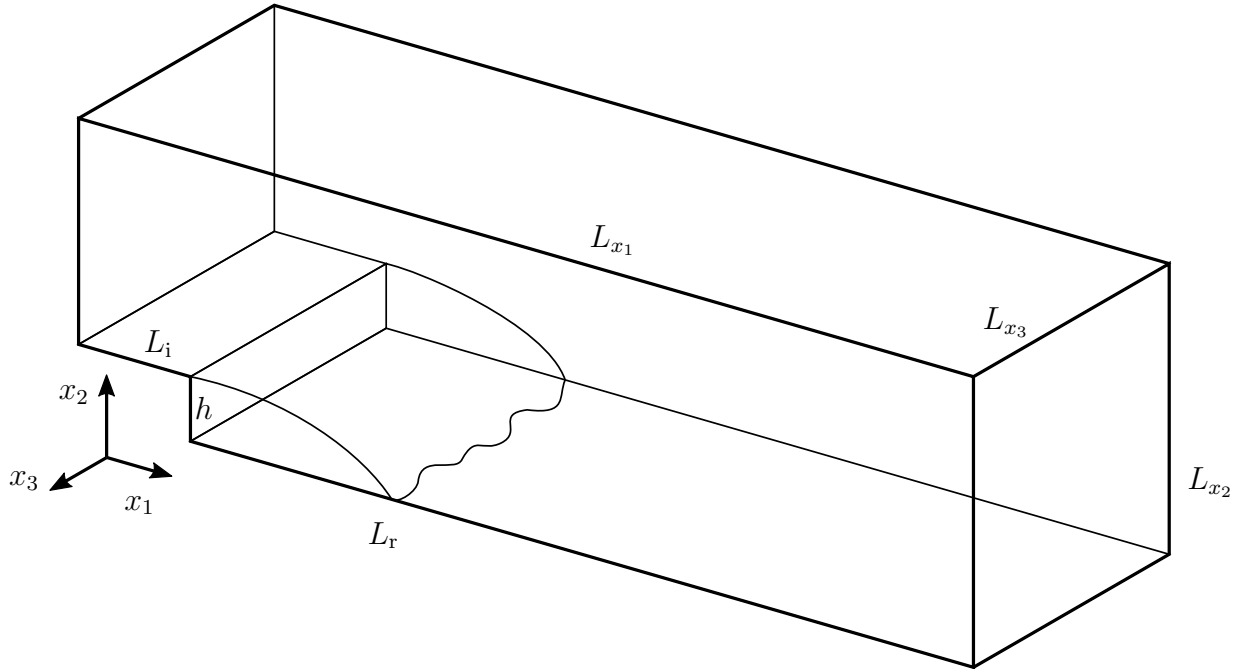


Figure 5.9: Computational domain of the backward facing step $ER = 1.2$

Table 5.5: Backward facing step flow parameters

parameters	values
L_{x_1}	30h
L_{x_2}	6h
L_{x_3}	4h
L_i	10h
γ_{bfs}	1.1
ER	1.2

as introduced in [15] are prescribed at $x_1 = (L_{x_1} - L_i)$. Periodic boundary conditions are used in spanwise (x_3) direction. The mean inflow velocity profile is obtained from Spalart's boundary layer simulation [55] at $Re_\theta = 670$, where θ denotes the boundary layer thickness. In order to understand how a boundary layer simulation can serve as an inflow condition for a backward facing step, we first have to introduce the different layers of near-wall flow, illustrated in Figure 5.10 [46].

The total shear stress τ in a wall-flow is the sum of the viscous stresses and the Reynolds stresses. Due to the no-slip condition, the latter has to vanish in the near-wall region, and thus the wall shear stress τ_w is entirely due to the contribution of the viscous stresses [46].

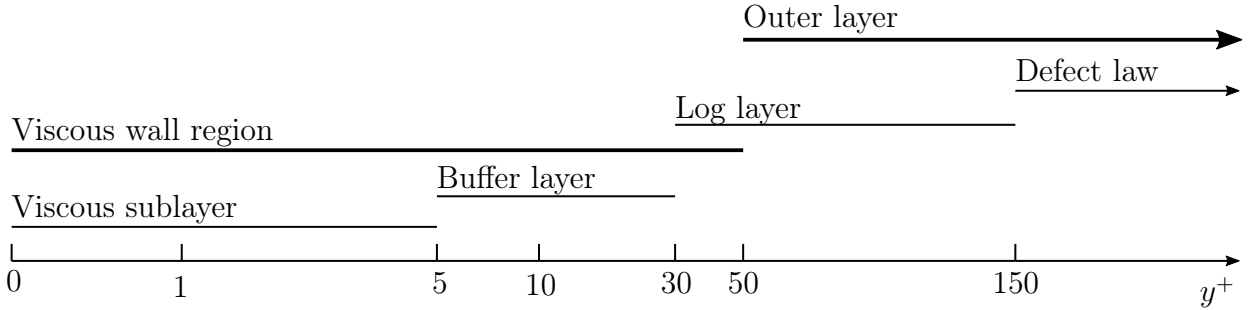


Figure 5.10: Different layers for near-wall flow [46]

Using τ_w , a dimensionless distance from the wall can be described as

$$x_2^+ = \frac{x_2 u_\tau}{\nu} . \quad (5.13)$$

The dimensionless velocity is then obtained as

$$u_1^+ = \frac{u_1}{u_\tau} . \quad (5.14)$$

Different layers in the near-wall region can be defined based on the dimensionless distance x_2^+ . Molecular viscosity has a direct effect on the shear stress in the viscous wall region ($x_2^+ < 5$), whereas the direct effect of viscosity is negligible in the outer layer ($x_2^+ \geq 50$). The viscous wall region can be further broken down in the the viscous sub-layer ($x_2^+ \leq 5$), where Reynolds stresses are negligible compared to viscous stresses, and the buffer layer ($5 < x_2^+ \leq 30$) – the region of transition between viscosity-dominated and turbulence-dominated flow. For fully-turbulent flows in the viscous sub-layer, DNS results show that the linear relation

$$u_1^+ = x_2^+ \quad \text{for } x_2^+ \leq 5 , \quad (5.15)$$

approximates the exact solution well. For larger x_2^+ , von Kármán proposed a logarithmic law [22] – commonly known as the law of the wall – that approximates the velocity u^+ as

$$u_1^+ = \frac{1}{\kappa_K} \ln(x_2^+) + C^+ , \quad (5.16)$$

with the von Kármán constant κ_K and the constant C^+ . The law of the wall is normally applicable for $x_2^+ > 30$; however, the accuracy of this law varies significantly over x_2^+ . Numerical results of Spalart's simulation suggest the values $C^+ = 4.3$ and $\kappa_K = 0.38$ for the law of the wall in the region from $50 < x_2^+ \leq 150$. The velocity profile in the buffer layer is similar to the law of the wall

$$u_1^+ = \frac{1}{c_1} \ln(x_2^+) + c_2 \quad \text{for } 5 < x_2^+ < 30 . \quad (5.17)$$

The constants c_1 and c_2 are determined by satisfying the continuity condition at $x_2^+ = 5$ and $x_2^+ = 30$. In the region $x_2^+ > 150$, the defect law

$$u_1^+ = \begin{cases} C_d \ln \frac{x_2}{\delta} + \frac{u_{\max}}{u_\tau}, & \text{if } C_d \ln \frac{x_2}{\delta} < 0 \\ \frac{u_{\max}}{u_\tau}, & \text{otherwise} \end{cases} \quad \text{for } x_2^+ \geq 150 , \quad (5.18)$$

holds. Here, the boundary layer thickness δ is defined as $\delta = 1.2h$. By construction, the defect law fulfills $u(\delta) = u_{\max}$. The constant C_d is determined by requiring continuity at $x_2^+ = 150$. In order to scale the $u_1^+(x_2^+)$ values obtained from the boundary layer simulation to the desired Reynolds number $Re_h = 5000$, we have to determine the friction velocity u_τ . Spalart reported the relation of the free flow velocity u_∞ with the velocity at the boundary layer $u_1(\delta) = 0.9974u_\infty$. Moreover, the relation $(u_\infty - u_1(\delta))/u_\tau = 0.052$ [55] was found. Assuming that $u_\infty \approx u_{\max}$, the following expression for the friction velocity is obtained

$$u_\tau = (1 - 0.9974) \frac{u_{\max}}{0.052} \quad (5.19)$$

Using a viscosity $\nu = 1.5 \cdot 10^{-5} \frac{\text{m}^2}{\text{s}}$, a step height $h = 0.0098\text{m}$ and a maximum velocity $u_{\max} = Re_h \nu / h \approx 7.653 \frac{\text{m}}{\text{s}}$, the friction velocity is computed as $u_\tau = 3.675 \cdot 10^{-5} \frac{\text{m}}{\text{s}}$. In order to obtain a turbulent inflow profile, velocity fluctuations u'_i must be prescribed.

5.2.3 Time advancement and post-processing

The simulation of the backward facing step runs for a total time $t_{\text{tot}} = 382h/u_{\max}$; where the first time of $273h/u_{\max}$ is discarded to allow for the flow of initial transients [31]. The time step size is calculated according to equation (5.4), using $CFL = 0.1$. The statistical quantities in this problem are computed differently to the turbulent channel as the flow is not periodic in x_1 -direction. The spatial average along lines in the (x_1, x_2) -plane can be evaluated by taking the average in x_3 -direction

$$\langle u_i(x_1, x_2, t) \rangle_{\text{hom}} = \frac{1}{L_{x_3}} \int_{-L_{x_3}}^0 u_i(\mathbf{x}, t) dx_3 \quad \text{for } i \in \{1, 2, 3\} . \quad (5.20)$$

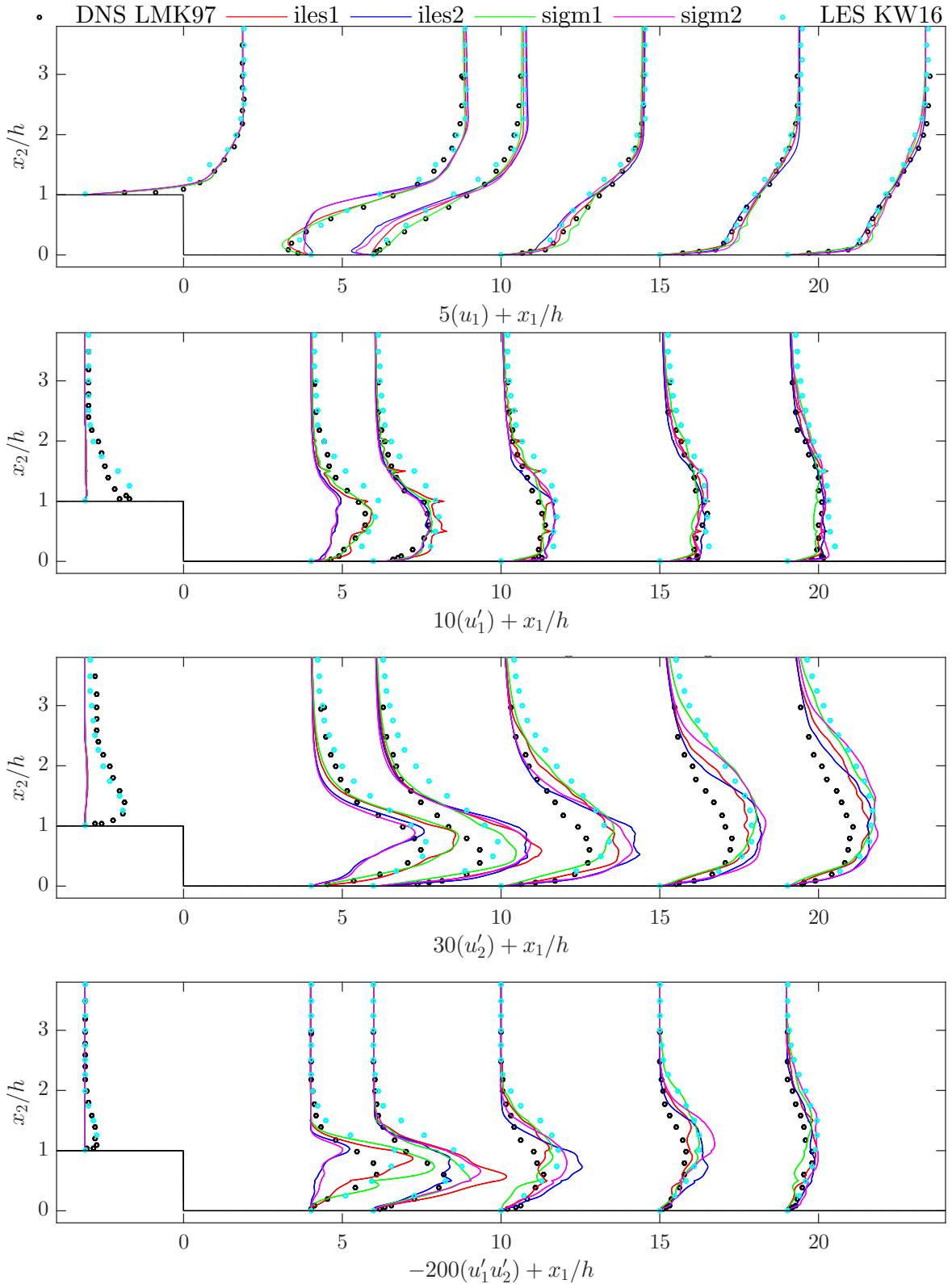


Figure 5.11: Numerical results for large eddy simulations (implicit and σ -model) of a backward facing step ($ER = 1.2$) compared with DNS [31] and LES [29] solutions

5.2.4 Evaluation and the importance of turbulent inflow data

It is well-known that properly chosen boundary conditions are essential in correctly representing a physical system as they determine a unique solution of the Navier–Stokes equation from a mathematical point of view [26]. In order to simulate turbulent flows, some kind of turbulent boundary condition must be prescribed. In Section 5.1, we saw that the turbulent channel flow, a simulation with periodic boundary condition in flow direction, is able to generate turbulence on its own after a certain transition time. Obtaining turbulent inflow data for a spatially inhomogeneous flow, on the other hand, needs modeling approaches, three of which are considered in this work. A review of the different methods used to generate turbulent inflow data is given in [57].

Random fluctuations method A turbulent inlet velocity field for spatially inhomogeneous flows can most easily be obtained by superimposing random fluctuations on a mean velocity profile [26]. In the case of the backward facing step, we aim to obtain a turbulent inflow profile by adding a random perturbation of 10% of the maximal velocity

$$u_i^{\text{turb}}(x_2, t) = \langle u_i(x_2, t) \rangle + \frac{u_{\max}}{10} R'(t) \quad \forall i \in \{1, 2, 3\} , \quad (5.21)$$

where R' is a random number between -1 and 1 . Using this method, numerical results for mean velocity profiles ($u_1 = \langle u_1 \rangle / u_{\max}$, RMS quantities ($u'_i = \sqrt{\langle u_i'^2 \rangle} / u_{\max}$, and the Reynolds stress ($u'_1 u'_2 = \langle u'_1 u'_2 \rangle / u_{\max}^2$) are obtained and can be seen in Figure 5.11. The ILES approach is used for both with and without an eddy viscosity model (σ -model). The different models are defined in Table 5.6. Results are obtained using the refined mesh $l = 1$.

Table 5.6: Model description for backward facing step ER = 1.2

model	ILES	ILES	σ -model $C_\sigma = 1.35$	σ -model $C_\sigma = 1.35$
name	iles1	iles2	sigm1	sigm2
polynomial degree k	3	6	3	6

The mean velocity profile is in well agreement with the DNS solution, indicating that it was a good choice to base the mean inflow profile on Spalart’s boundary layer simulation [55]. However, it can be seen that the random fluctuations method is not able to produce enough turbulence as the Reynolds stress and the RMS quantities are almost zero for $x_1 < 0$. One could argue that kinetic energy is distributed equally over the whole range of wavenumbers when using random fluctuations – contradicting the correct physical observations we made in Section 2.2. The lack of energy contained in the low-wavenumber region then results in an immediate damping of the imposed pseudo turbulence [26]. Klein et al. [26] state that it is desirable to design the computational domain in a way that the inflow boundary is far away from the area of interest. Hence, we aim to improve the random fluctuation method by increasing the inflow length of the backward

facing step. This approach has been used in [29] by increasing $L_i = 10h$ to $L_i^{\text{new}} = 30h$. However, within our approach, no significant improvements could be recognized, and thus the increased computing effort due to the larger inflow area could not be compensated.

Synthetic turbulence method A more advanced approach to generate turbulence inflow data is the synthetic turbulence method. The main idea behind this approach is to generate inflow data that satisfies certain statistical properties, which may be known from experiments or previously made simulations. The easiest synthetic approach is to alter the white noise amplitude in equation (5.21) according to the turbulence intensity

$$\text{TI}_i(x_2) = \frac{\sqrt{\langle u_i'^2(x_2) \rangle}}{\langle u_i(x_2) \rangle} \quad \forall i \in \{1, 2, 3\} \quad , \quad (5.22)$$

where the necessary quantities are obtained by Spalart's boundary layer simulation [55]. A velocity inflow profile using this method could then be chosen as

$$u_i^{\text{turb}}(x_2, t) = u_i(x_2, t) + \frac{u_{\max}}{5} R'(t) \text{TI}_i(x_2) \quad \forall i \in \{1, 2, 3\} \quad . \quad (5.23)$$

This method has a drawback of a missing correlation between the different components of the fluctuation, e.g., $\text{TI}_1(\langle u_1 \rangle)$ is just a function of $\langle u_1 \rangle$ and does not depend on either $\langle u_2 \rangle$ or $\langle u_3 \rangle$.

Another method to generate synthetic turbulent inflow data is presented in [26]. This method assumes that velocity fluctuations can be computed by filtering random data r

$$u'_{i,m} = \sum_{n=-N}^N b_n r_{m+n} \quad , \quad (5.24)$$

where b_n are the filter coefficients, and the random data satisfies the conditions $\langle r_m \rangle = 0$ and $\langle r_m r_m \rangle = 1$. Using that $\langle r_m r_n \rangle = 0 \quad \forall m \neq n$, the two-point correlation can be computed as

$$\frac{\langle u'_{i,m} u'_{i,m+k} \rangle}{\langle u'_{i,m} u'_{i,m} \rangle} = \sum_{j=-N+k}^N b_j b_{j-k} \left/ \sum_{j=-N}^N b_j^2 \right. \quad . \quad (5.25)$$

This method can easily be extended to three dimensions by the convolution of three one-dimensional filters. In order to compute the filter coefficients we estimate the autocorrelation function as

$$R(k) = \exp \left(\frac{-\pi k^2}{4n^2} \right) \quad , \quad (5.26)$$

where n is a parameter that has to be chosen. The filter coefficients can then be computed as

$$b_k \approx \tilde{b}_k \left/ \left(\sum_{j=-N}^N \tilde{b}_j^2 \right)^{1/2} \right. \quad \text{with } \tilde{b}_k = \exp \left(\frac{-\pi k^2}{2n^2} \right) \quad . \quad (5.27)$$

The velocity fluctuations can then be computed as a convolution of random data with the filter coefficients [26]. In order to account for cross correlations between different velocity components, a method that transforms the fluctuations [36] should be used. This transformation, however, needs the six quantities $\langle u_i u_j \rangle \forall i, j \in \{1, 2, 3\}$ (as input data), which could not be found, and thus rendering this method impractical.

Precursor simulation method Another approach to tackle the difficult generation of turbulent inflow data is the precursor simulation method. In this approach, a turbulent flow is precomputed and then introduced in the main simulation as inflow data. A precursor simulation implies additional computing and storage effort; however, it has the evident advantage of not being dependent on data from DNS, or any other previous experiments. Since our obtained results for the backward facing step ($ER = 1.2$) could correctly reproduce turbulence and a proper near-wall behavior, we will consider another backward facing step ($ER = 1.5$) with a precursor simulation.

5.3 Backward facing step with precursor simulation

In this section, we consider a turbulent channel flow to generate inflow data for the backward facing step. This method has been successfully used by Rasthofer and Gravemeier [48] and it was found that running the simulations simultaneously considerably reduces the storage effort. The work in [48] considers a backward facing step of expansion ratio $ER = 1.5$ (see Figure 5.12) at Reynolds number

$$Re_H = \frac{u_c H}{\nu} = 5540 , \quad (5.28)$$

where u_c denotes the mean centerline velocity. An experimental study of a similar flow has been carried out by Kasagi and Matsunaga in [25], where the step height is $H = 0.041\text{m}$, and a friction Reynolds number $Re_\tau = 290$ based on the kinematic viscosity $\nu = 1.5268 \cdot 10^{-5} \frac{\text{m}}{\text{s}^2}$ was evaluated upstream of the step.

5.3.1 Computational domain

Figure 5.12 shows the computational domain of the backward facing step with precursor simulation. A uniform grid (abbreviated as uni) as well as a stretched grid (abbreviated as str) according to the mapping

$$x_2 \mapsto f(x_2) = \begin{cases} -0.5H \left(1 - \frac{\tanh(60(-0.5H-x_2))}{\tanh(-30H)} \right) & \text{for } x_2 < 0 \\ H \left(1 - \frac{\tanh(40(H-x_2))}{\tanh(40H)} \right) & \text{for } x_2 \geq 0 \end{cases} , \quad (5.29)$$

have been used. The meshes for both methods are visualized in Figure A.3.

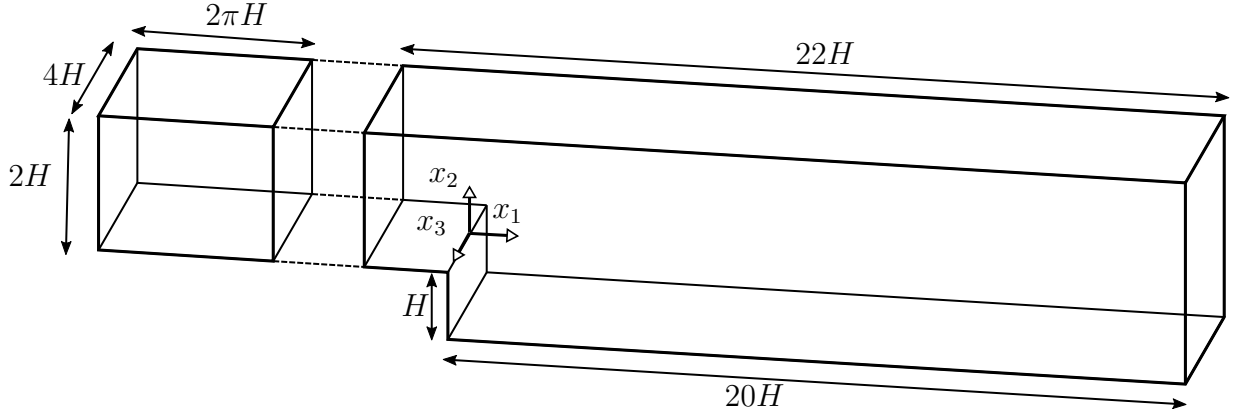


Figure 5.12: Sketch of backward facing step ($ER = 1.5$) geometry with turbulent channel as a precursor simulation

5.3.2 Boundary and initial conditions

Precursor simulation The initial and boundary conditions for the turbulent channel are chosen in a similar manner as in Subsection 5.1.2. Assuming equilibrium of forces, the friction Reynolds number can be used to calculate the volume force for the precursor simulation as

$$f_1 \cdot \underbrace{(2H \cdot 4H \cdot 2\pi H)}_{\text{volume of turbulent channel}} = \tau_w \cdot \underbrace{(2 \cdot 4H \cdot 2\pi H)}_{\text{solid wall areas}} ,$$

$$f_1 = \tau_w / H ,$$

where the wall shear stress is given by

$$\tau_w = \rho u_\tau^2 = \rho (\text{Re}_\tau \nu / H)^2 .$$

Assuming that $\rho = 1 \frac{\text{kg}}{\text{m}^3}$, the volume force in x_1 -direction can then be computed as

$$f_1 = \rho \frac{\text{Re}_\tau^2 \nu^2}{H^3} \approx 0.2844518 \frac{\text{N}}{\text{m}^3} . \quad (5.30)$$

Backward facing step Unlike the backward facing step ($ER = 1.2$) in Section 5.2, this version has a no-slip boundary condition at the wall at $x_2 = 2H$. The outflow velocity profile of the turbulent channel is used as the inflow velocity profile for the backward facing step at $x_1 = -2H$. Symmetric boundary conditions are chosen in spanwise direction (at $x_3 = 2H$ and $x_3 = -2H$). The outflow boundary conditions at $x_1 = 20H$ are chosen as described in [15].

5.3.3 Time advancement and post-processing

The simulation of this backward facing step runs for a total time of $t_{\text{tot}} = 6\text{s}$. The first two seconds are discarded, and statistical quantities are computed for the remaining time

($2\text{s} \leq t \leq 6\text{s}$) by averaging at every tenth time step. The CFL numbers for the uniform and stretched grid are chosen as $\text{CFL}_{\text{uni}} = 0.15$ and $\text{CFL}_{\text{str}} = 0.50$, respectively. The averaging process is performed as described in Subsection 5.2.3

5.3.4 Evaluation

For this simulation, statistical quantities are computed for the positions $x_1 = 0.0, 1.0, \dots, 10.0$, and compared with experimental data (denoted as Exp KM95) [25]. We further compare our obtained results to a LES (denoted as RG13) [48] with roughly 10^6 degrees of freedom (DOF), and thus choose the polynomial degree k and the refinement level l accordingly. Two simulations are carried out; one with the combination of polynomial degree $l = 3$ and $k = k_u = 2$ (denoted as (3, 2)), resulting in 1002496 DOF. A second simulation uses the combination (2, 5), resulting in 1088384 DOF.

The obtained quantities are normalized as

$$\begin{aligned}(u_1) &= \langle u_1 \rangle / u_c , \\ (u'_i) &= \frac{5}{u_c} \sqrt{\langle u_i'^2 \rangle} \quad \text{for } i \in \{1, 2, 3\} , \\ (u'_1 u'_2) &= \frac{50}{u_c^2} \langle u'_1 u'_2 \rangle ,\end{aligned}$$

where u_c is the mean inflow velocity for the backward facing step. Furthermore, the skin friction coefficient C_f is computed at the lower solid wall in x_2 -direction (at $x_2 = -H$) as

$$C_f = \frac{\tau_w}{\frac{1}{2} \rho u_c^2} \tag{5.31}$$

In order to test which grid (uni or str) is better suited for our numerical scheme, we first carried out numerical results for the pure ILES approach. As seen in Figure 5.13, the simulation for the stretched grid as well as the simulation for the uniform grid using polynomial degree $k = 5$ and refinement level $l = 2$ are in excellent agreement with the results of RG13. The ILES with (3, 2) and uniform mesh is not able to reproduce the correct near-wall behavior. The simulations with (2, 5) give better predictions for the Reynolds stress, compared to the simulations with (3, 2), as seen in Figure 5.15. A clear statement for the accuracy of the different approaches in predicting the RMS quantities can not be given (Figure 5.14). For the approach with $l = 2$ and $k = 5$, we will perform numerical simulations using the uniform grid. This decision is not based on the discussed results, but rather due to undesirable large cells for the stretched grid at refinement level $l = 2$. For the approach (3, 2), the stretched grid will be used as the uniform grid is not able to correctly resolve the obtained quantities in near-wall regions. Note that in the following, the combination of eddy viscosity model with numerical dissipation is referred to by the name of the eddy viscosity model.

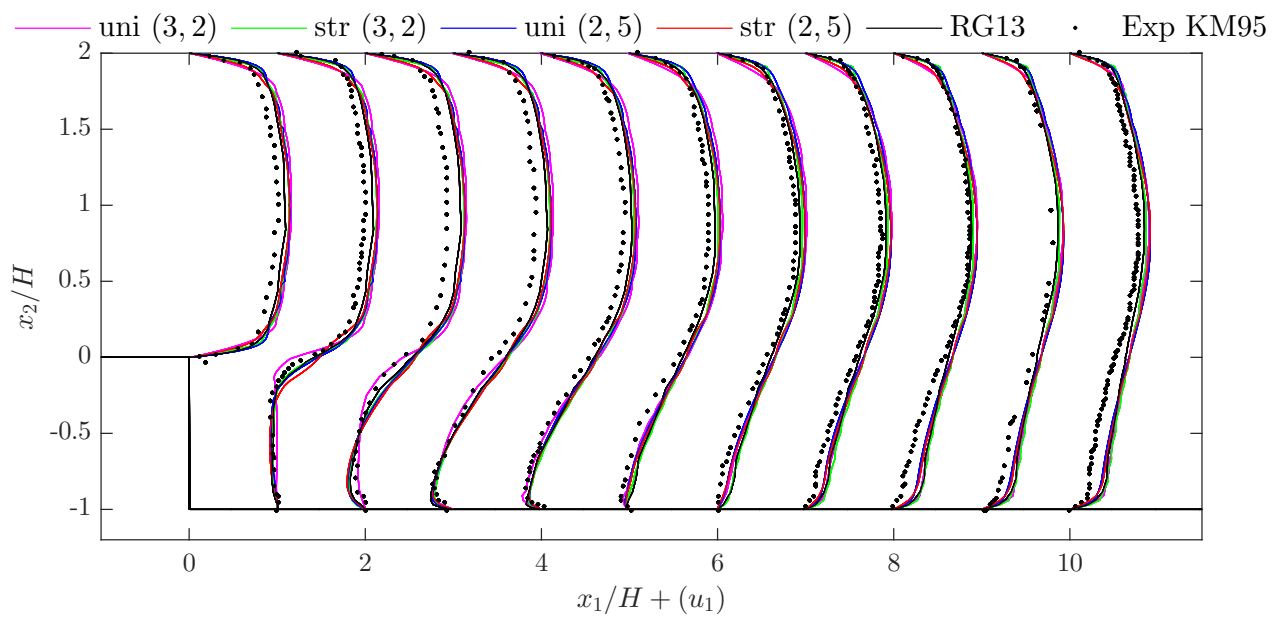


Figure 5.13: Plot of the mean velocity for the pure ILES approach

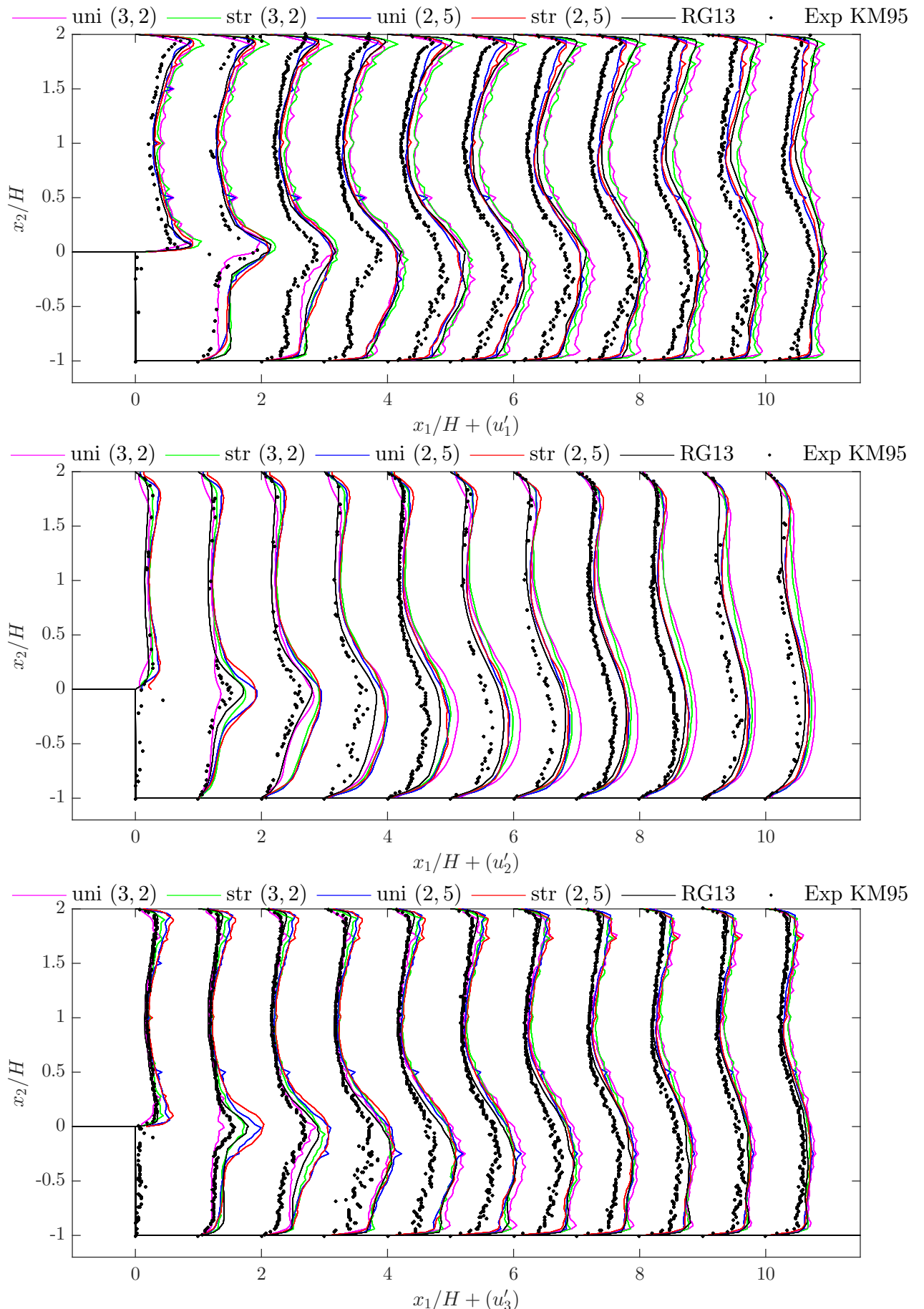


Figure 5.14: Plot of the RMS values for the pure ILES approach

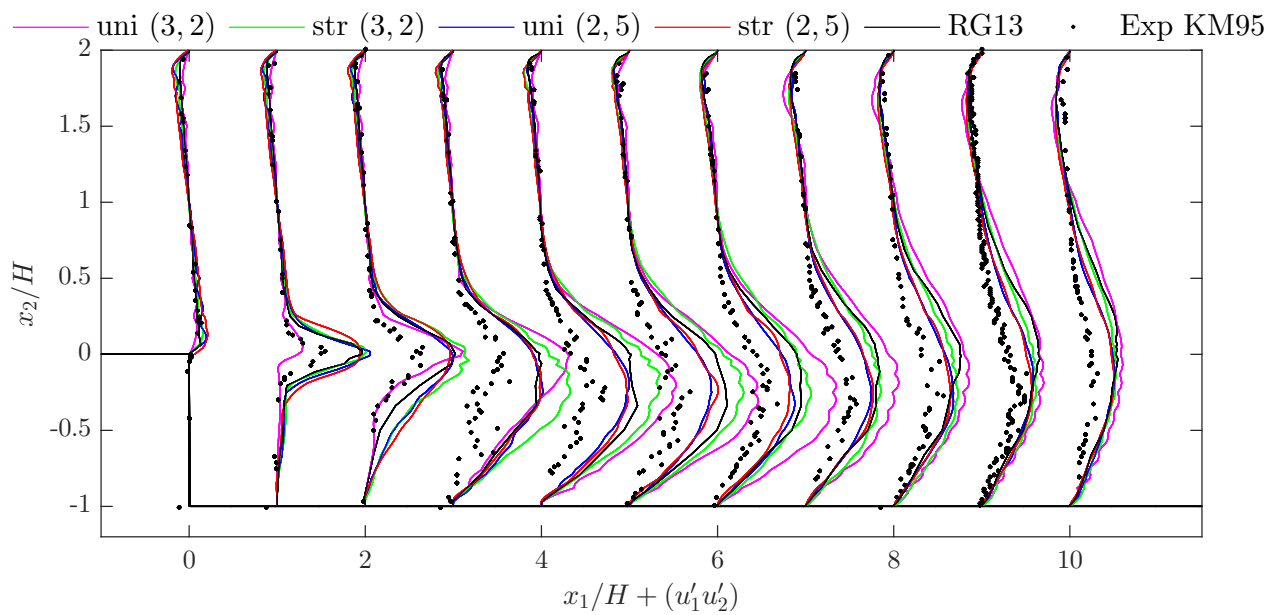


Figure 5.15: Plot of the Reynolds stress for the pure ILES approach

Numerical simulation for refinement level $l = 3$ and polynomial degree $k = 2$ using a stretched grid In Figure 5.16, it can be seen that the Vreman model as well as the WALE model and the σ -model are in good agreement with the reference data. The Vreman model is in better agreement for $x_2 < 0$, the other two models predict the mean velocity better for $x_2 \geq 0$. The Smagorinsky model can not resolve the correct near-wall behavior and has a significantly higher maximum velocity than the reference data. Both observations indicate that the Smagorinsky model makes the initial turbulent flow laminar. Moreover, the Smagorinsky model fails to resolve the correct RMS values as well as the Reynolds stress, as can be seen in Figure 5.17 and Figure 5.18. The WALE model and the σ -model give results close the predictions of the LES RG13. The predictions of the Vreman model for the RMS quantities as well as the Reynolds stresses is especially for $x_1/H < 4$ in good agreement with the experimental data, however, it significantly overpredicts these quantities $x_1/H \geq 7$. The pure ILES approach is generally in good agreement with the predictions of the LES RG13, however, overpredicts the quantity (u'_2) as well as the Reynolds stress $(u'_1 u'_2)$. The skin friction coefficient C_f is in good agreement with the reference LES for the pure ILES approach as well as the WALE model and the σ -model for $x_1/H \leq 6$ (see Figure 5.19). The Vreman model overpredicts the reattachment point. The three combination models mentioned overpredict the skin friction coefficient for larger x_1/H values. The Smagorinsky model is not in agreement with the reference data. A clear statement regarding a superior model can not be given.

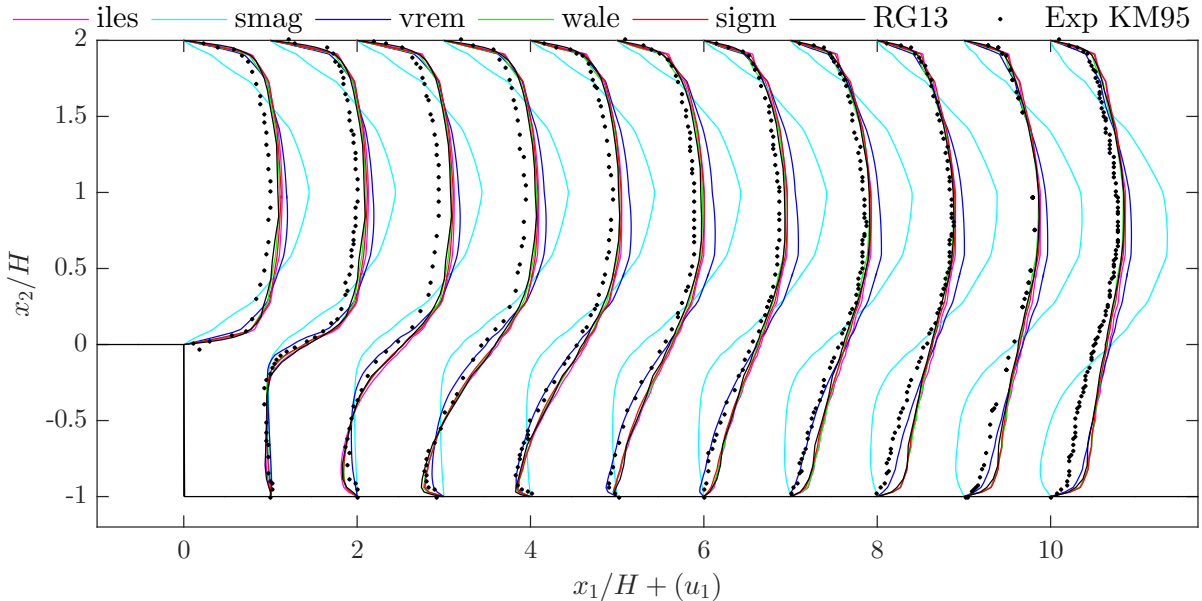


Figure 5.16: Plot of the mean velocity for combination of eddy viscosity model with numerical dissipation and spatial discretization (3, 2)

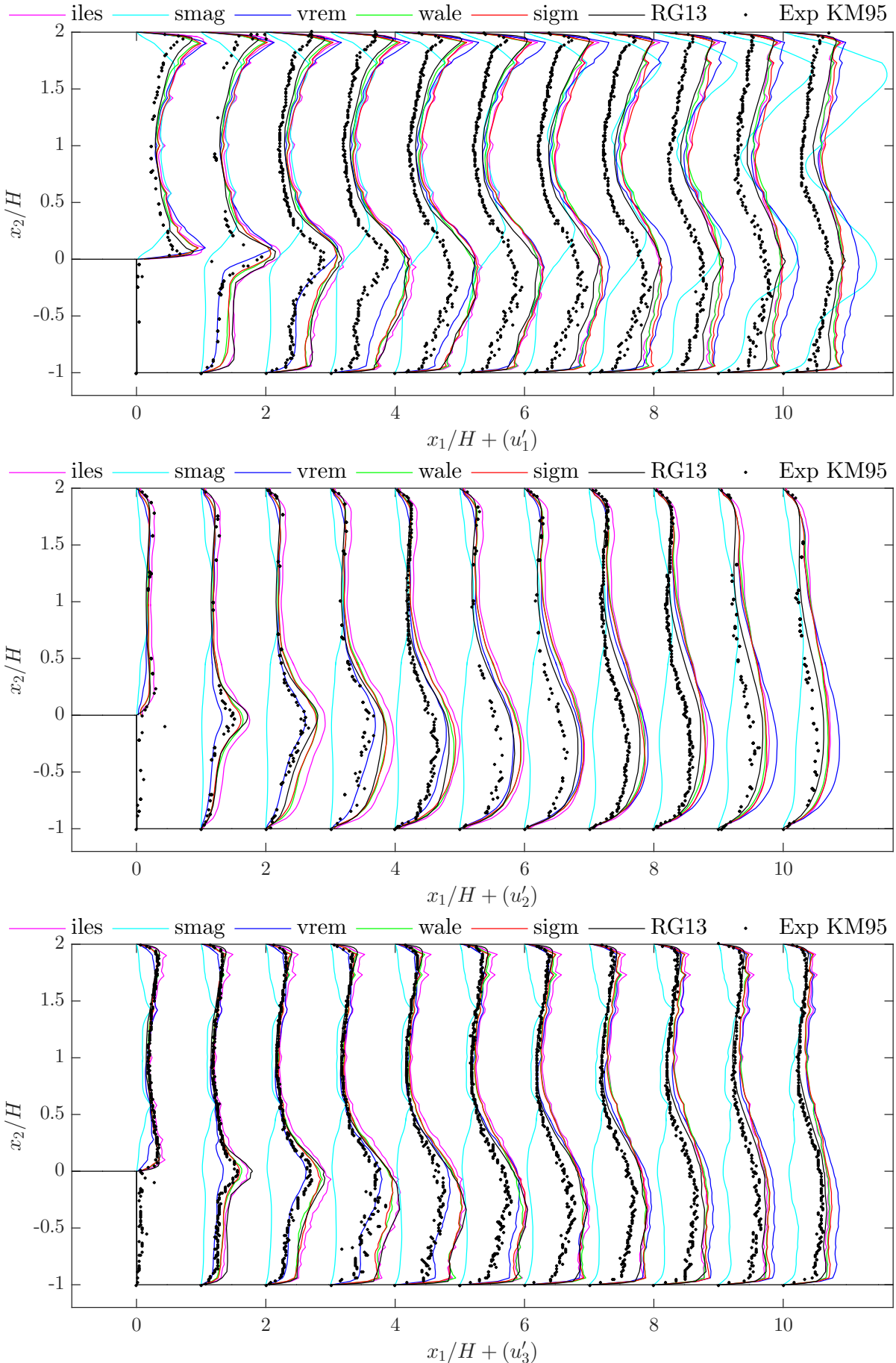


Figure 5.17: Plot of the RMS values for combination of eddy viscosity model with numerical dissipation and spatial discretization (3, 2) 60

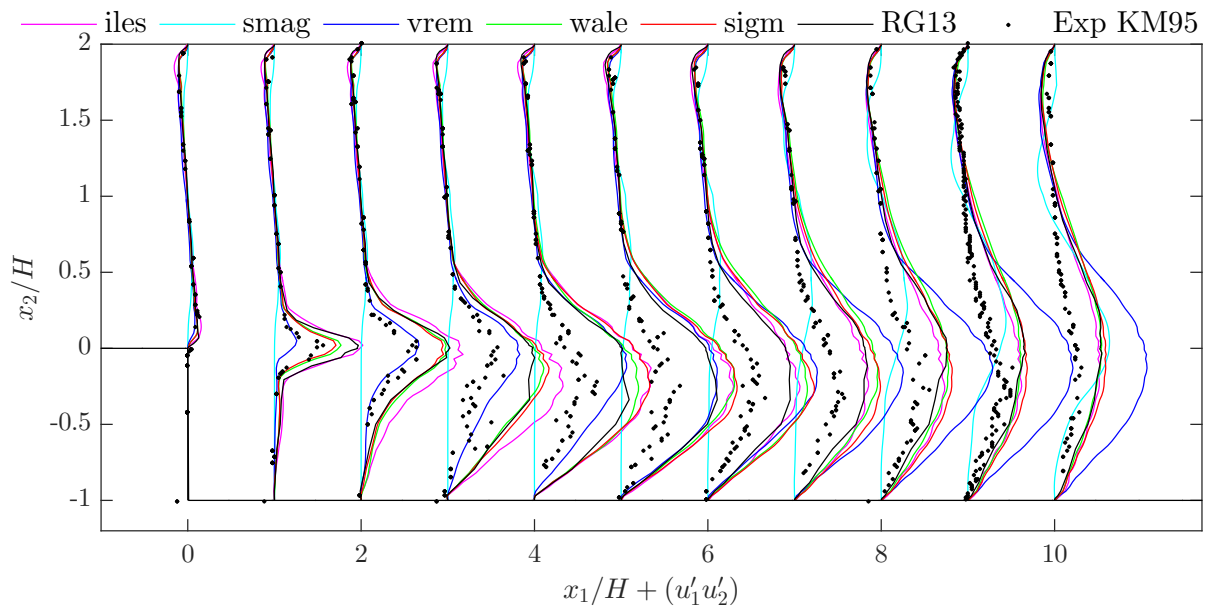


Figure 5.18: Plot of the Reynolds stress for combination of eddy viscosity model with numerical dissipation and spatial discretization (3, 2)

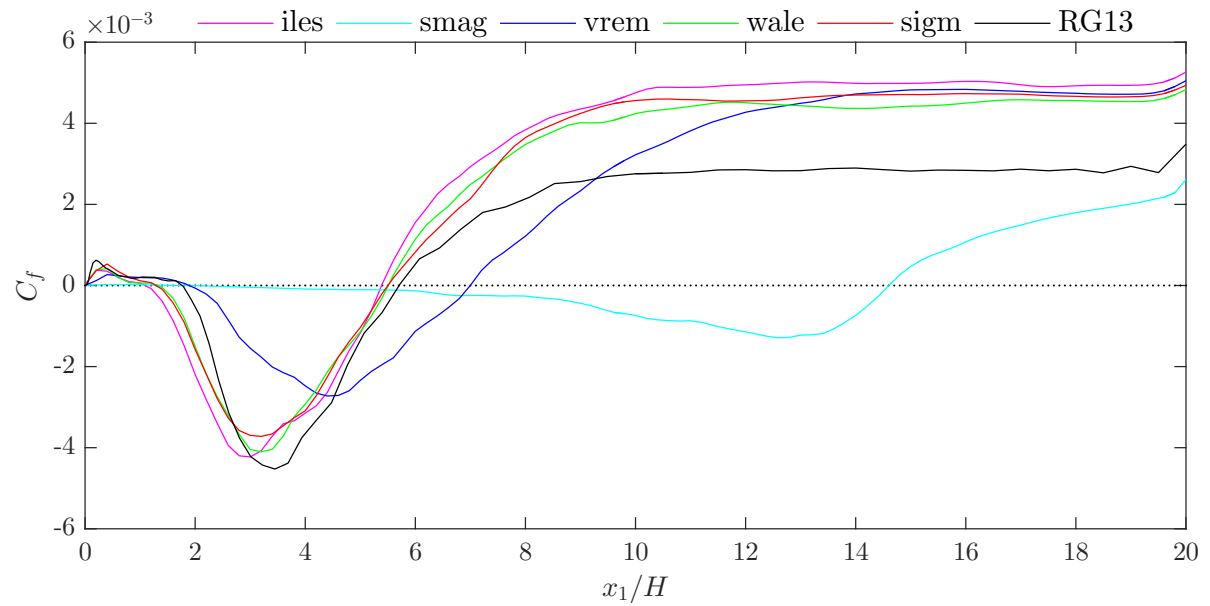


Figure 5.19: Plot of the skin friction for combination of eddy viscosity model with numerical dissipation and spatial discretization (3, 2)

Numerical simulation for refinement level $l = 2$ and polynomial degree $k = 5$ using a uniform grid

The prediction of the mean velocity (Figure 5.20) is overall quite similar to the predictions of the simulation with (3, 2); however, the Vreman model agrees for this simulation more with the reference LES predictions (RG13) than with the experimental data. Furthermore, the Vreman model predicts the mean velocity less accurately when approaching the upper wall, compared to the (3, 2) simulation. The WALE model as well as the σ -model show similar behavior for both simulations. Regarding the RMS quantities, the Vreman model is closer to the LES reference data, when compared to the (3, 2) simulation. Similarly to the mean velocity predictions, the Vreman model is less accurate than both the WALE model and the σ -model (especially as x_2/H approaches the upper wall at $x_2/H = 2$). The Smagorinsky model predicts the RMS quantities as well as the Reynolds stress as zero for almost all locations; however, the RMS quantity (u'_1) is overpredicted for some x_2/H at $x_1/H \geq 6$. For this simulation, the pure ILES approach gives significantly better results for the Reynolds stress compared to the simulation (3, 2). The Vreman model is in better agreement, especially for $x_2/H \geq 8$, than before as well. The predictions of the WALE model and the σ model have not changed significantly between the two different simulations. The pure ILES approach is generally in good agreement with the LES reference data, however, overpredicts the RMS quantity (u'_2) for the locations $x_1/H \leq 4$. For $x_1/H \geq 3$, the pure ILES approach is in better agreement with the experimental data than the combination models. The skin friction predictions in Figure 5.23 are similar to the prediction of the numerical simulation (3, 2); however, the Vreman model predicts the reattachment point more accurately.

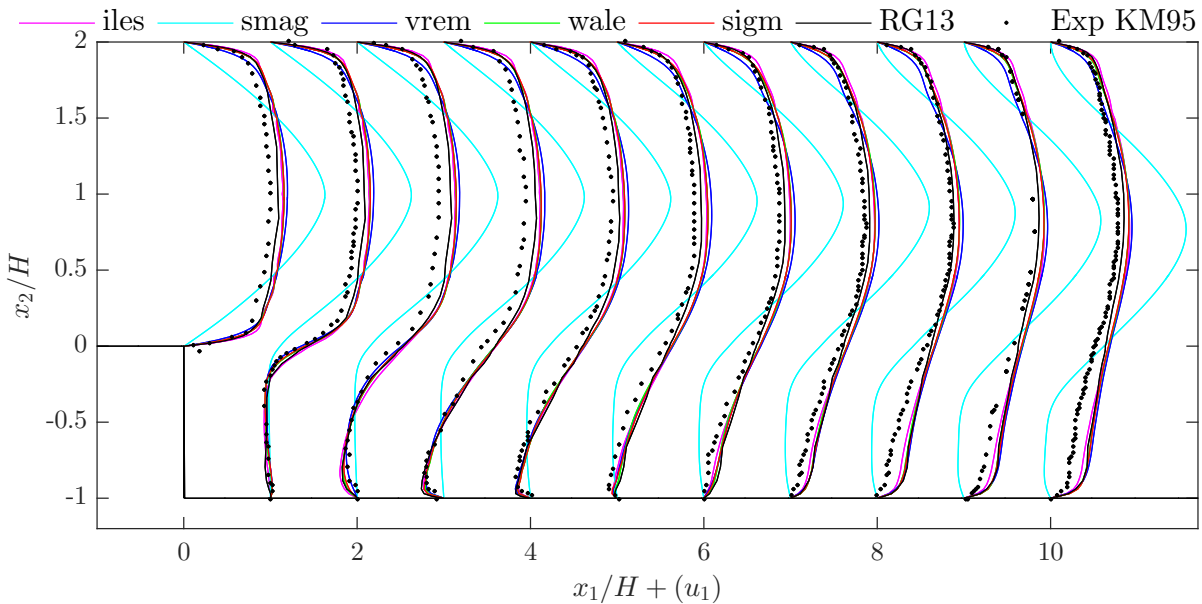


Figure 5.20: Plot of the mean velocity for combination of eddy viscosity model with numerical dissipation and spatial discretization (2, 5)

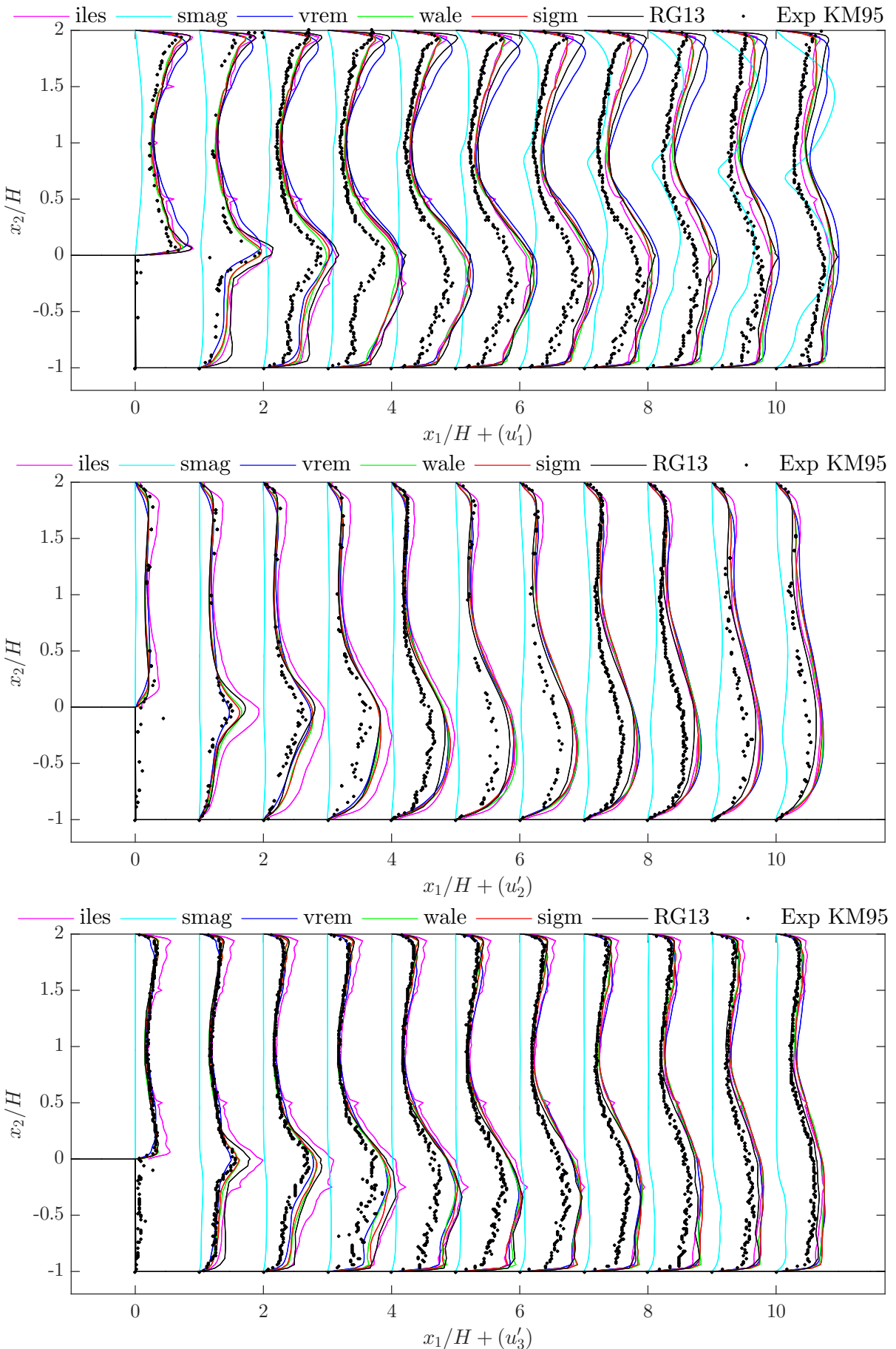


Figure 5.21: Plot of the RMS values for combination of eddy viscosity model with numerical dissipation and spatial discretization (2, 5) 63

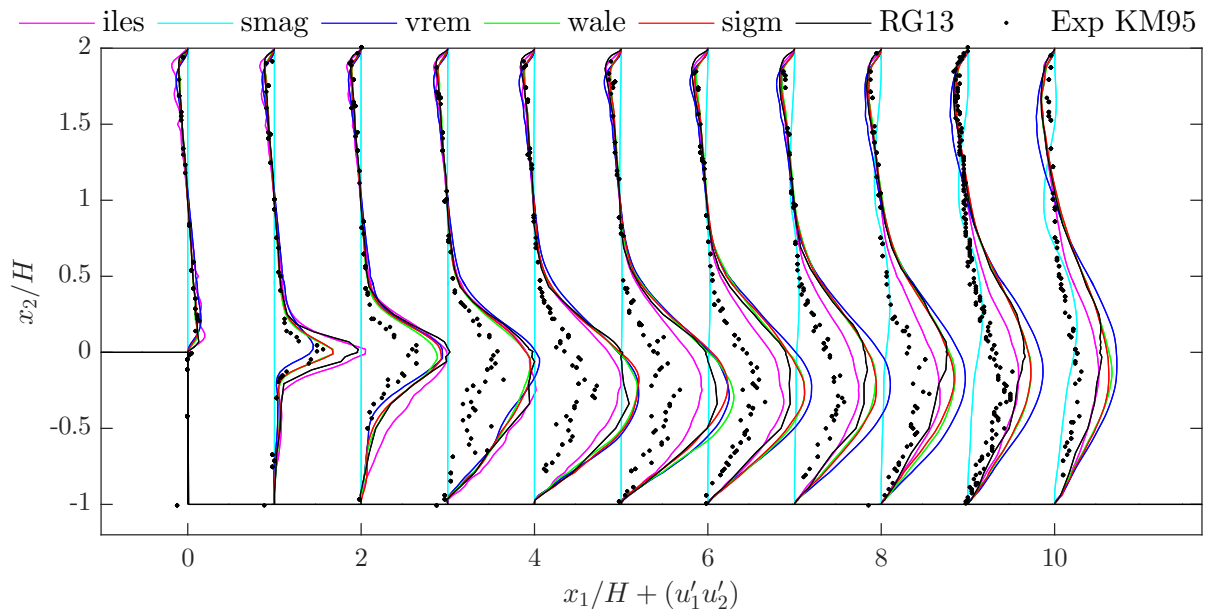


Figure 5.22: Plot of the Reynolds stress for combination of eddy viscosity model with numerical dissipation and spatial discretization (2, 5)

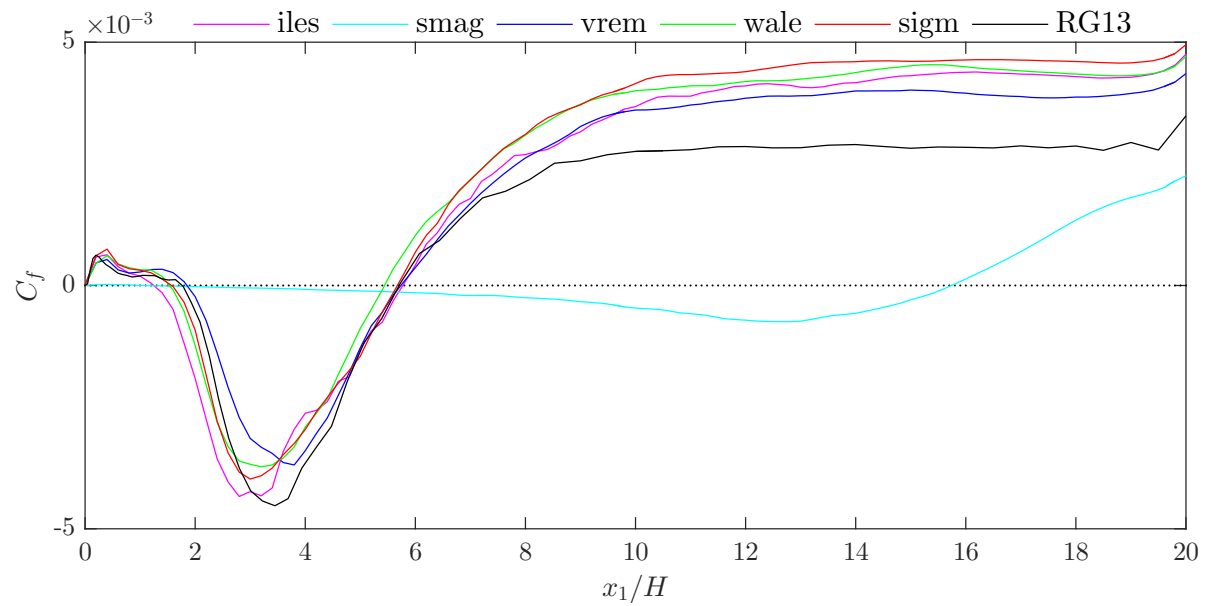


Figure 5.23: Plot of the skin friction for combination of eddy viscosity model with numerical dissipation and spatial discretization (2, 5)

Table 5.7: Global wall time for the numerical simulations of the backward facing step ER = 1.5

Model	iles	smag	vrem	wale	sigm
Global wall time (3, 2) in CPUh	26.532	28.364	43.253	46.493	47.161
Increase of time compared to iles in %	-	6.9	63	75.2	77.8
Global wall time (2, 5) in CPUh	167.073	169.127	176.840	181.920	186.753
Increase of time compared to iles in %	-	1.2	5.8	8.9	11.8

5.3.5 Discussion of results

The Smagorinsky model does not give reasonable results when used for this turbulent flow problem, which is in agreement with results obtained in Section 5.1. The other three eddy viscosity models could partially improve the pure ILES approach, especially in the (u'_2) prediction for the (2, 5) simulation as well as in the Reynolds stress prediction for the (3, 2) simulation. In contrast to the turbulent channel flow, simulations for different model constants were not carried out. A clear difference between the accuracy of the (3, 2) simulation and the (2, 5) could not be seen. For this flow problems, computation times were measured and are shown in Table 5.7. The global wall time is computed as

$$\text{Global wall time [CPUh]} = \text{computation time [s]} \cdot \text{number of MPI processes} \cdot \frac{1[\text{h}]}{3600[\text{s}]} \quad (5.32)$$

The high uncertainty of the obtained results combined with additional computational costs when using a combination approach makes its use impractical. We suggest that the effort of using an additional eddy viscosity model in combination with the pure ILES approach can only be justified if better results are consistently obtained.

Chapter 6

Conclusion and outlook

This thesis deals with turbulence modeling for large eddy simulation of incompressible flows using high-order discontinuous Galerkin methods. A common approach of the LES method is shown and applied to the governing equations. The resulting unclosed set of equations is closed by modeling the anisotropic shear-stress tensor with local linear eddy viscosity models. Those models account for the unresolved smallest-scales by adding an artificial sub-grid viscosity ν_{SGS} to the laminar viscosity ν . The computation of the sub-grid viscosity ν_{SGS} is performed element-wise – a cheap method as the eddy viscosity models just need to evaluate local velocity gradients. When using a DG discretization in combination with the high-order dual splitting scheme, the artificial viscosity can then be directly embedded in the viscous step. However, an issue in the boundary conditions has been observed, resulting in the disregard of the spatial variability of the quantity ν_{SGS} . The characteristic filter width Δ , a quantity that is associated with the turbulence model, has been chosen to be equal to the effective length scale h_{eff} .

In order to clarify the difference between the modeling of physical dissipation (achieved for example by an eddy viscosity model) and numerical dissipation, the idea of the implicit large eddy simulation has been reviewed. Several numerical simulations for two turbulent flow problems are carried out to investigate two major questions.

- Does an eddy viscosity model have the ability to stabilize a DG scheme?
- Is the addition of an eddy viscosity model to the ILES approach advantageous?

Numerical solutions of the turbulent channel flow indicate that neither of the four tested eddy viscosity models is able to stabilize our DG scheme in the absence of numerical dissipation. This observation is contradicting recent findings in research. As reported in previous work, the pure ILES approach for DG schemes yields excellent results. Within our work, an additional eddy viscosity model could improve the accuracy of the pure ILES approach in some cases. Of the four models used, the WALE model and the σ -model, both of which decay as the cube of the distance to a solid wall, showed the best results. The Smagorinsky model, on the other hand, yields extraordinarily poor results, most likely

due to the presence of turbulent stresses in near-wall regions. The Vreman model, an eddy viscosity model that vanishes linearly with the distance to a solid boundary, showed modest results. To sum up, our results indicate that a physically correct near-wall behavior is important when using an eddy viscosity model in combination with an ILES approach.

Moreover, numerical simulations of the turbulent channel flow for different Reynolds numbers and effective resolutions indicate, that the model constant should C_m change with the Reynolds number Re , the grid size h , and the polynomial degree k . However, since our choice of the characteristic filter width is rather based on logical consequences than any mathematical theory, it is just as likely that C_m is a true constant and Δ should vary. In general, we can just say the product of both quantities is a function of the earlier mentioned parameters, i.e., $(C_m\Delta) = f(Re, h, k)$. The high uncertainty of the obtained results, e.g., due to the correct determination of the model constant, as well as the additional computation time renders the combination approach impractical. Especially when a pure ILES approach yields results of the same (or even better) accuracy, an additional eddy viscosity model is not required.

As a part of future work, more numerical simulations of the ILES approach in combination with an eddy viscosity model could be performed. As simulating turbulence is generally associated with an heavy computational effort, an easy turbulent flow problem like the Taylor–Green vortex might be best suited for performing a parameter study of the quantity $(C_m\Delta)$. Performing simulation for more sophisticated problems like the backward facing step might be interesting as well, as they could give a better insight of the method in realistic engineering problems.

Within this work, we had to face the difficulty of generating appropriate turbulent inflow data when dealing with inhomogeneous flow problems. The random fluctuations method could not give the desired results as DG schemes effectively damp fluctuations of high frequency. Synthetic turbulence methods, on the other hand, rely to much on previous work, e.g., DNS or experiments, and are therefore especially not suited for engineering problems. Using a precursor simulation, we could ensure to prescribe a fully-turbulent velocity profile at the inflow boundary of our actual simulation. The computational cost of our simulation are just slightly increased, as the computational domain of the precursor simulation is small compared to the simulation domain. Generally, it does not matter how turbulence is generated, however, its presence is crucial in order to test turbulence models.

Again it has to be mentioned, that the turbulence modeling of this work is confined to linear eddy viscosity models. When using LES in combination with the DG discretization, other modeling methods might be better suited. Or perchance, our numerical scheme is just better suited for the ILES approach than an eddy viscosity approach. For this reason, more research should be carried out to get a better understanding in modeling turbulence, when using a DG discretization scheme for the simulation of under-resolved flows.

Appendix A

Appendix

A.1 Mesh for turbulent channel problem

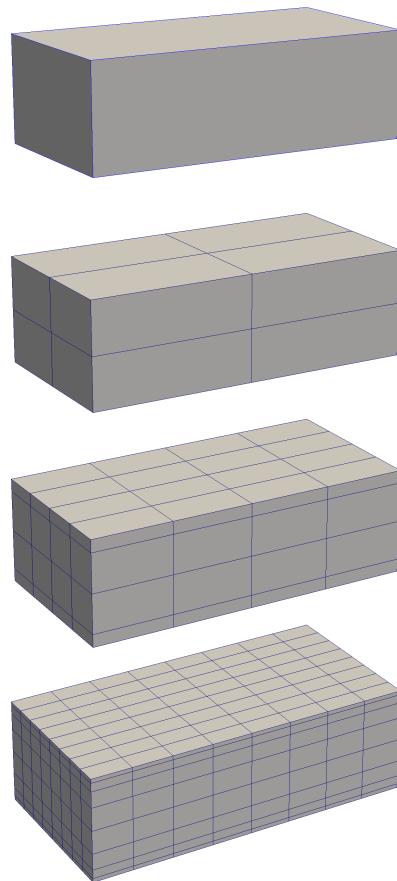


Figure A.1: Refine levels $l = 0, 1, 2, 3$ for turbulent channel problem

Table A.1: Mesh refinement for turbulent channel problem

refinement level l	0	1	2	3
Number of cells	1	8	64	512

A.2 Mesh for backward facing step problem $ER = 1.2$

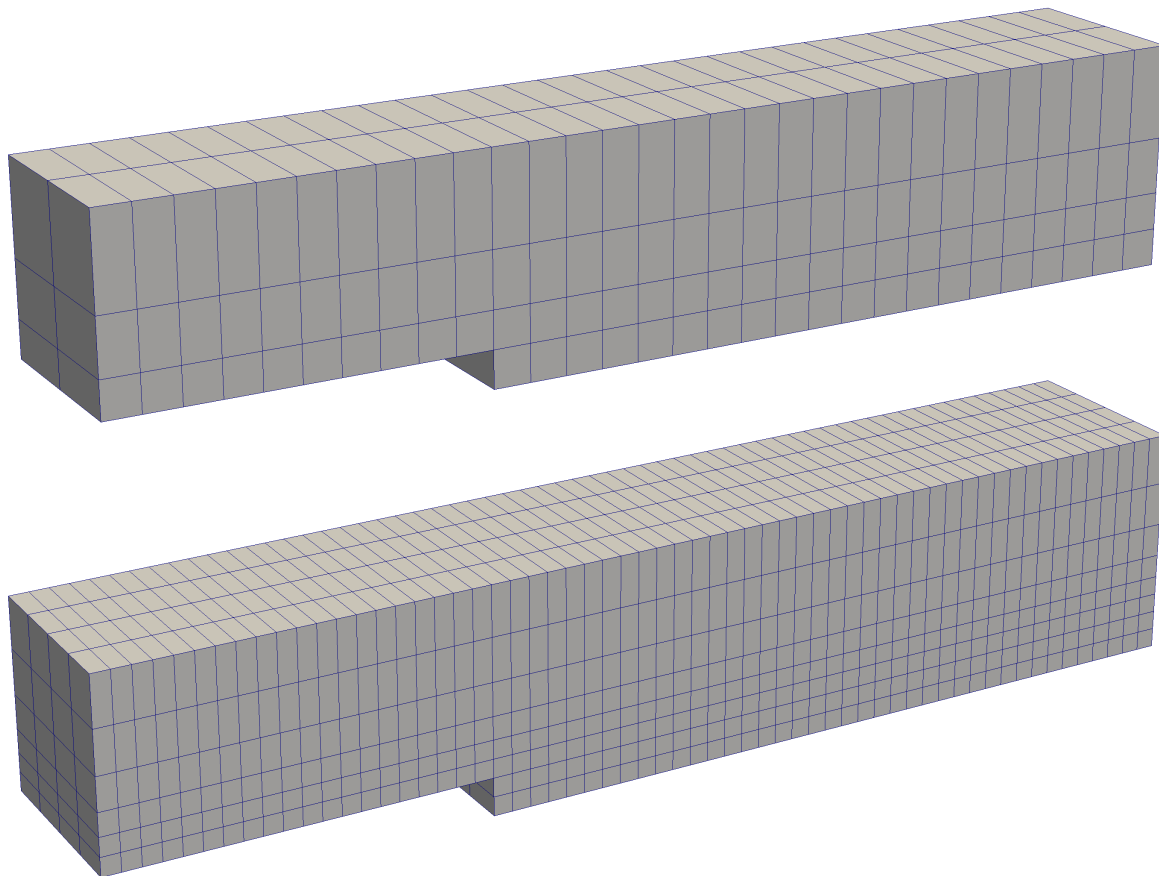


Figure A.2: Refine levels $l = 0, 1$ for backward facing step problem $ER = 1.2$

Table A.2: Mesh refinement for backward facing step problem $ER = 1.2$

refinement level l	0	1
Number of cells	220	1760

A.3 Mesh for backward facing step problem $ER = 1.5$ with precursor

Table A.3: Mesh refinement for backward facing step problem $ER = 1.5$ with precursor

mesh	uni $l = 2$	str $l = 3$
Number of cells: backward facing step	1344	10752
Number of cells: precursor	64	512
Number of cells int total	1408	11264

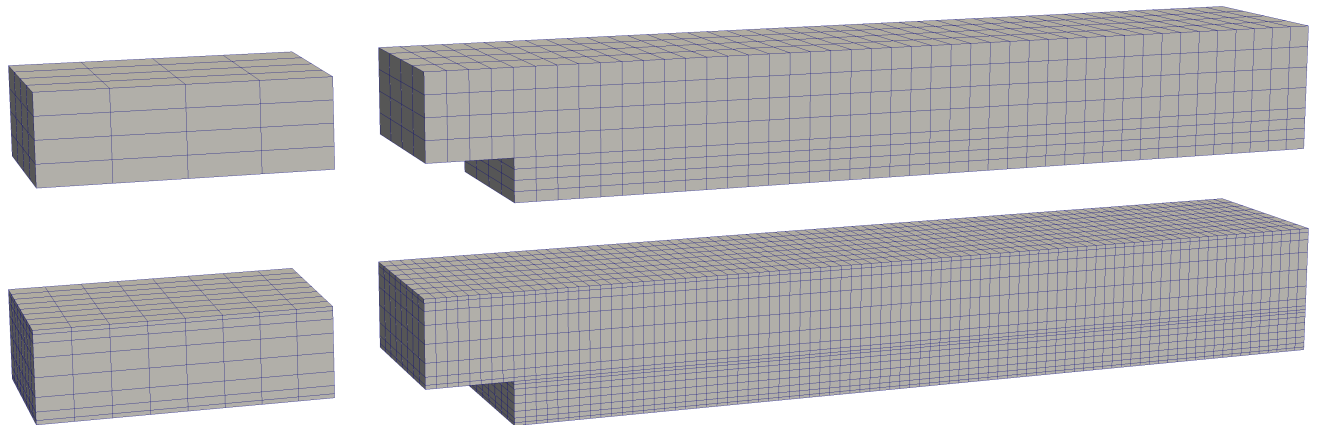


Figure A.3: Mesh for the uniform grid ($l = 2$) and the stretched grid ($l = 3$) of a backward facing step problem $ER = 1.5$

Bibliography

- [1] M. Abramowitz, I. A. Stegun, et al. *Handbook of mathematical functions with formulas, graphs, and mathematical tables*, volume 9. Dover, New York, 1972.
- [2] D. Arndt, W. Bangerth, D. Davydov, T. Heister, L. Heltai, M. Kronbichler, M. Maier, J.-P. Pelteret, B. Turcksin, and D. Wells. The `deal.II` library, version 8.5. *Journal of Numerical Mathematics*, 2017.
- [3] D. N. Arnold, F. Brezzi, B. Cockburn, and L. D. Marini. Unified analysis of discontinuous Galerkin methods for elliptic problems. *SIAM journal on numerical analysis*, 39(5):1749–1779, 2002.
- [4] J. C. Butcher. *Numerical methods for ordinary differential equations*. John Wiley & Sons, 2016.
- [5] D. R. Chapman and G. D. Kuhn. The limiting behaviour of turbulence near a wall. *Journal of Fluid Mechanics*, 170:265–292, 1986.
- [6] A. J. Chorin. Numerical solution of the Navier–Stokes equations. *Mathematics of computation*, 22(104):745–762, 1968.
- [7] C. L. Fefferman. Existence and smoothness of the Navier–Stokes equation. *The millennium prize problems*, pages 57–67, 2006.
- [8] N. Fehn. A discontinuous Galerkin approach for the unsteady incompressible Navier–Stokes equations. Master’s thesis, Institute for Computational Mechanics, Technical University of Munich, 2015.
- [9] N. Fehn. A comparison of high-order discontinuous Galerkin solvers for the incompressible Navier–Stokes equations based on a high-performance, matrix-free implementation. Technical report, Institute for Computational Mechanics, Technical University of Munich, 2016.
- [10] N. Fehn, W. A. Wall, and M. Kronbichler. On the stability of projection methods for the incompressible Navier–Stokes equations based on high-order discontinuous Galerkin discretizations. *Journal of Computational Physics*, 2017.

- [11] E. Ferrer, D. Moxey, R. Willden, and S. Sherwin. Stability of projection methods for incompressible flows using high order pressure-velocity pairs of same degree: continuous and discontinuous Galerkin formulations. *Communications in Computational Physics*, 16(3):817–840, 2014.
- [12] E. Ferrer and R. Willden. A high order discontinuous Galerkin finite element solver for the incompressible Navier–Stokes equations. *Computers & Fluids*, 46(1):224–230, 2011.
- [13] R. Friedrich and M. Arnal. Analysing turbulent backward-facing step flow with the lowpass-filtered Navier–Stokes equations. *Journal of Wind Engineering and Industrial Aerodynamics*, 35:101–128, 1990.
- [14] M. Germano, U. Piomelli, P. Moin, and W. H. Cabot. A dynamic subgrid-scale eddy viscosity model. *Physics of Fluids A: Fluid Dynamics*, 3(7):1760–1765, 1991.
- [15] V. Gravemeier, A. Comerford, L. Yoshihara, M. Ismail, and W. A. Wall. A novel formulation for neumann inflow boundary conditions in biomechanics. *International Journal for Numerical Methods in Biomedical Engineering*, 28(5):560–573, 2012.
- [16] F. F. Grinstein, L. G. Margolin, and W. J. Rider. *Implicit large eddy simulation: computing turbulent fluid dynamics*. Cambridge university press, 2007.
- [17] K. M. Hasan, P. J. Bassar, D. L. Parker, and A. L. Alexander. Analytical computation of the eigenvalues and eigenvectors in dt-mri. *Journal of Magnetic Resonance*, 152(1):41–47, 2001.
- [18] J. S. Hesthaven and T. Warburton. *Nodal discontinuous Galerkin methods: algorithms, analysis, and applications*. Springer Science & Business Media, 2007.
- [19] S. M. Joshi, P. J. Diamessis, D. T. Steinmoeller, M. Stastna, and G. N. Thomsen. A post-processing technique for stabilizing the discontinuous pressure projection operator in marginally-resolved incompressible inviscid flow. *Computers & Fluids*, 139:120–129, 2016.
- [20] S. Jovic and D. M. Driver. Backward-facing step measurements at low reynolds number, $Re_h = 5000$. 1994.
- [21] L. Kaiktsis, G. E. Karniadakis, and S. A. Orszag. Onset of three-dimensionality, equilibria, and early transition in flow over a backward-facing step. *Journal of Fluid Mechanics*, 231:501–528, 1991.
- [22] T. v. Kármán. Mechanische ähnlichkeit und Turbulenz, nach Ges. *Wiss. Gottingen. Math. Physik. Klasse*, 1930.
- [23] G. Karniadakis and S. Sherwin. *Spectral/hp element methods for computational fluid dynamics*. Oxford University Press, 2013.

- [24] G. E. Karniadakis, M. Israeli, and S. A. Orszag. High-order splitting methods for the incompressible Navier–Stokes equations. *Journal of computational physics*, 97(2):414–443, 1991.
- [25] N. Kasagi and A. Matsunaga. Three-dimensional particle-tracking velocimetry measurement of turbulence statistics and energy budget in a backward-facing step flow. *International Journal of Heat and Fluid Flow*, 16(6):477–485, 1995.
- [26] M. Klein, A. Sadiki, and J. Janicka. A digital filter based generation of inflow data for spatially developing direct numerical or large eddy simulations. *Journal of computational Physics*, 186(2):652–665, 2003.
- [27] A. N. Kolmogorov. The local structure of turbulence in incompressible viscous fluid for very large Reynolds numbers. In *Dokl. Akad. Nauk SSSR*, volume 30, pages 299–303, 1941.
- [28] B. Krank, N. Fehn, W. A. Wall, and M. Kronbichler. A high-order semi-explicit discontinuous Galerkin solver for 3D incompressible flow with application to DNS and LES of turbulent channel flow. *Journal of Computational Physics*, 348:634–659, 2017.
- [29] B. Krank and W. A. Wall. A new approach to wall modeling in LES of incompressible flow via function enrichment. *Journal of Computational Physics*, 316:94–116, 2016.
- [30] M. Kronbichler and K. Kormann. A generic interface for parallel cell-based finite element operator application. *Computers & Fluids*, 63:135–147, 2012.
- [31] H. Le, P. Moin, and J. Kim. Direct numerical simulation of turbulent flow over a backward-facing step. *Journal of fluid mechanics*, 330:349–374, 1997.
- [32] A. Leonard. Energy cascade in large-eddy simulations of turbulent fluid flows. *Advances in geophysics*, 18:237–248, 1975.
- [33] M. Lesieur. *Turbulence in fluids*, volume 40. Springer Science & Business Media, 2012.
- [34] D. Leslie and G. Quarini. The application of turbulence theory to the formulation of subgrid modelling procedures. *Journal of fluid mechanics*, 91(1):65–91, 1979.
- [35] D. K. Lilly. The representation of small-scale turbulence in numerical simulation experiments. In *Proc. IBM Sci. Compt. Symp. Environ. Sci., White Plains, IBM, 1967*, 1967.
- [36] T. S. Lund, X. Wu, and K. D. Squires. Generation of turbulent inflow data for spatially-developing boundary layer simulations. *Journal of Computational Physics*, 140(2):233–258, 1998.
- [37] M. Marek, A. Tyliszczak, and A. Bogusławski. Large eddy simulation of incompressible free round jet with discontinuous Galerkin method. *International Journal for Numerical Methods in Fluids*, 79(4):164–182, 2015.

- [38] C. Meneveau, T. S. Lund, and W. H. Cabot. A lagrangian dynamic subgrid-scale model of turbulence. *Journal of Fluid Mechanics*, 319:353–385, 1996.
- [39] P. Moin and J. Kim. Numerical investigation of turbulent channel flow. *Journal of fluid mechanics*, 118:341–377, 1982.
- [40] R. D. Moser, J. Kim, and N. N. Mansour. Direct numerical simulation of turbulent channel flow up to $\text{Re}_\tau = 590$. *Physics of fluids*, 11(4):943–945, 1999.
- [41] R. Moura, G. Mengaldo, J. Peiró, and S. Sherwin. On the eddy-resolving capability of high-order discontinuous Galerkin approaches to implicit les/under-resolved dns of euler turbulence. *Journal of Computational Physics*, 330:615–623, 2017.
- [42] F. Nicoud and F. Ducros. Subgrid-scale stress modelling based on the square of the velocity gradient tensor. *Flow, turbulence and Combustion*, 62(3):183–200, 1999.
- [43] F. Nicoud, H. B. Toda, O. Cabrit, S. Bose, and J. Lee. Using singular values to build a subgrid-scale model for large eddy simulations. *Physics of Fluids*, 23(8):085106, 2011.
- [44] S. A. Orszag, M. Israeli, and M. O. Deville. Boundary conditions for incompressible flows. *Journal of Scientific Computing*, 1(1):75–111, 1986.
- [45] J. M. Ortega. *Matrix theory: A second course*. Springer Science & Business Media, 2013.
- [46] S. B. Pope. *Turbulent flows*. IOP Publishing, 2001.
- [47] L. Prandtl. A report on testing for built-up turbulence. *Z. Angew. Math. Mech.*, 5:136–139, 1925.
- [48] U. Rasthofer and V. Gravemeier. Multifractal subgrid-scale modeling within a variational multiscale method for large-eddy simulation of turbulent flow. *Journal of Computational Physics*, 234:79–107, 2013.
- [49] O. Reynolds. On the dynamical theory of incompressible viscous fluids and the determination of the criterion. *Proceedings of the Royal Society of London*, 56(336-339):40–45, 1894.
- [50] L. F. Richardson. Weather prediction by numerical process cambridge university press. *CambridgeRichardson Weather prediction by numerical process1922*, 1922.
- [51] P. Sagaut. *Large eddy simulation for incompressible flows: an introduction*. Springer Science & Business Media, 2006.
- [52] F. G. Schmitt. About boussinesq’s turbulent viscosity hypothesis: historical remarks and a direct evaluation of its validity. *Comptes Rendus Mécanique*, 335(9-10):617–627, 2007.

- [53] K. Shahbazi. An explicit expression for the penalty parameter of the interior penalty method. *Journal of Computational Physics*, 205(2):401–407, 2005.
- [54] J. Smagorinsky. General circulation experiments with the primitive equations: I. the basic experiment. *Monthly weather review*, 91(3):99–164, 1963.
- [55] P. R. Spalart. Direct simulation of a turbulent boundary layer up to $\text{Re}_\theta = 1410$. *Journal of fluid mechanics*, 187:61–98, 1988.
- [56] D. T. Steinmoeller, M. Stastna, and K. Lamb. A short note on the discontinuous Galerkin discretization of the pressure projection operator in incompressible flow. *Journal of Computational Physics*, 251:480–486, 2013.
- [57] G. R. Tabor and M. Baba-Ahmadi. Inlet conditions for large eddy simulation: a review. *Computers & Fluids*, 39(4):553–567, 2010.
- [58] G. Taylor and A. Green. Mechanism of the production of small eddies from large ones. *Proceedings of the Royal Society of London. Series A, Mathematical and Physical Sciences*, 158(895):499–521, 1937.
- [59] L. Timmermans, P. Minev, and F. Van De Vosse. An approximate projection scheme for incompressible flow using spectral elements. *International journal for numerical methods in fluids*, 22(7):673–688, 1996.
- [60] E. R. Van Driest. On turbulent flow near a wall. *J. Aeronaut. Sci*, 23(11):1007–1011, 1956.
- [61] A. Vreman. An eddy-viscosity subgrid-scale model for turbulent shear flow: Algebraic theory and applications. *Physics of fluids*, 16(10):3670–3681, 2004.
- [62] B. Vreman, B. Geurts, and H. Kuerten. Realizability conditions for the turbulent stress tensor in large-eddy simulation. *Journal of Fluid Mechanics*, 278:351–362, 1994.
- [63] C. C. Wiart, K. Hillewaert, L. Bricteux, and G. Winckelmans. Implicit LES of free and wall-bounded turbulent flows based on the discontinuous Galerkin/symmetric interior penalty method. *International Journal for Numerical Methods in Fluids*, 78(6):335–354, 2015.